

ADSORPTION PROCESSES IN NUCLEAR FUEL RESOURCE RECOVERY

A Thesis
Presented to
The Academic Faculty

by

Alexander Ian Wiechert

In Partial Fulfillment
of the Requirements for the Degree
Doctor of Philosophy in the
School of Civil and Environmental Engineering

Georgia Institute of Technology

May 2020

COPYRIGHT © 2020 BY ALEXANDER IAN WIECHERT

ADSORPTION PROCESSES IN NUCLEAR FUEL RESOURCE RECOVERY

Approved by:

Dr. Sotira Yiacoumi
School of Civil and Environmental Eng.
Georgia Institute of Technology

Dr. Costas Tsouris
School of Civil and Environmental Eng.
Georgia Institute of Technology

Dr. James Mulholland
School of Civil and Environmental Eng.
Georgia Institute of Technology

Dr. Yingjie Liu
School of Mathematics
Georgia Institute of Technology

Dr. Spyros Pavlostathis
School of Civil and Environmental Eng.
Georgia Institute of Technology

Date Approved: December 9th, 2019

ACKNOWLEDGMENTS

Over the last few years as I have worked towards the completion of this thesis, there have been many individuals who have aided me in this endeavor. First of all, I would like to express my deepest gratitude to my advisor, Professor Sotira Yiacoumi, for her advice, encouragement, and support and for giving me the opportunity to pursue these studies. I must also thank Dr. Costas Tsouris for his invaluable guidance in carrying out this research. I would also like to thank the other members of my committee, Dr. Jim Mulholland, Dr. Spyros Pavlostathis, and Dr. Yingjie Liu, for their valuable time and their insightful comments that have helped to shape this work. I am also fortunate to have worked alongside many talented individuals in the Colloids and Interfaces Group including Dr. Austin Ladshaw, Dr. Yong-ha Kim, Dr. Lydia Park, Ziheng Shen, and Abishek Kasturi whose dedication to their own research has been an inspiration.

Much of the work described here has been built upon collaborative efforts between myself and other students, post-docs, professors, and researchers from various institutions around the country. I would also like to thank those individuals: (i) Gary Gill, Jordana Wood, Li-Jung Kuo, Jonathan Strivens, and Nicholas Schlafer from Pacific Northwest National Laboratory, (ii) Wei-Po Liao, Tomonori Saito, Candice Halbert, Eunice Hong, Jisue Moon, and Carter Abney from Oak Ridge National Laboratory, (iii) Lawrence Tavlarides, Yue Nan, Seungrag Choi, and Jiuxu Liu from Syracuse University, and (iv) Horng-Bin Pan and Chein Wai from the University of Idaho. This work was supported by the United States Department of Energy through the Office of Nuclear Energy and through the Nuclear Energy University Program.

Lastly, I thank my parents and family for everything that they have done for me not just during this endeavor but throughout my entire life.

TABLE OF CONTENTS

ACKNOWLEDGMENTS	iii
LIST OF TABLES	viii
LIST OF FIGURES	x
LIST OF COMMON SYMBOLS	xiv
SUMMARY	xvi
CHAPTER 1: Introduction	1
1.1 Background	1
1.2 Motivation	1
1.3 Scope and Objectives	5
1.4 References	8
PART I. RECOVERY OF URANIUM FROM SEAWATER	12
CHAPTER 2: Effect of Adsorbent Conformation	13
2.1 Introduction	13
2.2 Materials and Methods	14
2.2.1 Sample Preparation	14
2.2.2 Neutron Reflectometry	16
2.3 Results and Discussion	18
2.4 Conclusions	24
2.5 Acknowledgments	26
2.6 References	26
2.7 Nomenclature	27
CHAPTER 3: Impact of Metal Ion Competition	29
3.1 Introduction	29
3.2 Materials and Methods	30
3.2.1 Materials	30
3.2.2 Experimental Setup	30
3.2.3 Modeling Methodology	32
3.3 Results and Discussion	34
3.3.1 Analysis of Feed Seawater	34
3.3.2 Analysis of Desalination Brine Reject	39
3.4 Conclusions	44
3.5 Acknowledgments	46
3.6 References	46
3.7 Nomenclature	49

CHAPTER 4: Alternative Adsorbent Synthesis	51
4.1 Introduction	51
4.2 Methodology	52
4.2.1 Experimental Methodology	52
4.2.2 Modeling Methodology	55
4.3 Results and Discussion	56
4.4 Conclusions	64
4.5 Acknowledgments	66
4.6 References	66
4.7 Nomenclature	68
PART II. NUCLEAR FUEL REPROCESSING OFF-GAS TREATMENT	70
CHAPTER 5: Aging Effect in Silver Exchanged Mordenite	71
5.1 Introduction	71
5.2 Methodology	72
5.2.1 Materials	72
5.2.2 Aging Experiments	73
5.2.3 XAS Methods	75
5.2.4 Adsorption Modeling	76
5.3 Results and Discussion	78
5.3.1 Iodine Capacity Experiments	78
5.3.2 XAS Results	80
5.3.3 Aging Modeling	87
5.4 Conclusions	92
5.5 Acknowledgments	94
5.6 References	94
5.7 Nomenclature	97
CHAPTER 6: Aging Effect in Silver Aerogel	99
6.1 Introduction	99
6.2 Methodology	100
6.2.1 Materials	100
6.2.2 Experimental Methodology	101
6.2.3 Modeling Methodology	102
6.3 Results and Discussion	103
6.3.1 Aging and XAS Experiments	103
6.3.2 Aging Modeling	109
6.4 Conclusions	110
6.5 Acknowledgments	111
6.6 References	111
6.7 Nomenclature	114

CHAPTER 7: Conclusions and Recommendations	115
APPENDIX A: Uranium Recovery from Seawater	121
A.1 Aqueous Speciation Model	121
A.2 References	123
APPENDIX B: Silver Adsorbent Aging	125

LIST OF TABLES

Table 2.1 – Summary of film thickness (T) obtained from neutron reflectivity under different measurement conditions. Roughness (R) listed for single block polymers (PAO and PAO-co-PAA) is the interfacial polymer-to-air roughness; d-PAO roughness is for quartz to polymer transition; PAA roughness is polymer to D ₂ O; inter-polymer roughness is 10Å for all samples	23
Table 3.1 – Experimental and predicted adsorption results (mg/g and mmol/kg adsorbent) after 12 weeks in batch and the initial aqueous concentrations (µg/L and nM) determined from 10 mL aliquots of feed seawater. The analytical error is approximately 5%, as reported by Gill et al. (2016). ⁴	34
Table 3.2 – Experimental and predicted adsorption results (mg/g adsorbent) after 12 weeks and the initial aqueous concentration (µg/L) determined from 10 mL sample of brine reject. The analytical error is approximately 5%, as reported by Gill et al. (2016). ⁴	39
Table 4.1 – Forward (k_f) and reverse (k_r) reaction rate constants for U, V, and Zn and adsorbent max capacity (mol/kg adsorbent) for small and large braids.	56
Table 4.2 – Concentration in feed seawater and salinity normalized 28-day adsorption capacities on small braids in Cage B (LCW-B) and Cage C large braids (LCW-C) for U, V, Fe, Zn, and Cu.	57
Table 4.3 – Simulated 56-day salinity normalized raceway adsorption capacity (mg/g) and saturated adsorption capacity (mg/g) for V, U, and Zn on the Cage B small braids.	63
Table 4.4 – Simulated 56-day salinity normalized raceway adsorption capacity (mg/g) and saturated adsorption capacity (mg/g) for V, U, and Zn on Cage C large braids.	63

Table 5.1 – Equilibrium I ₂ capacity measured in weight percent gained after aging Ag ⁰ Z for a variety of times in the 1% NO in N ₂ and 2% NO ₂ in dry air aging environments at 150°C	79
Table 5.2 – Forward and reverse reaction rate constants for all reactions used in aging simulations for 1% NO in N ₂ and 2% NO ₂ in dry air at 150°C and the reaction for I ₂ adsorption on Ag ⁰ . Reaction orders determined by stoichiometry unless otherwise noted.	92
Table 6.1 – I ₂ capacity as a percentage of initial weight gained after exposure to 50 ppmv I ₂ in dry air at 150°C for Ag ⁰ functionalized aerogel aged with an unaged capacity of 36.4 w.t. % in dry air (dew point of -70°C), humid air (dew point of -15°C), and 1% NO in N ₂ gas streams.	104
Table A1 – Concentration (µg/L) determined from 10 mL aliquots of feed seawater.	122
Table A2 – Concentration (µg/L) determined from 10-mL aliquots of brine reject.	122
Table A3 – Summary of adsorption reactions with IDO ligand and their equilibrium constants considered in the adsorption model in addition to the reactions used in the works of Ladshaw and coworkers ^{A3-A5} adjusted for 23°C and zero ionic strength.	122
Table A4 – Summary of aqueous reactions considered in the adsorption model in addition to those used in the works of Ladshaw and coworkers. ^{A3-A5} Equilibrium constants are adjusted for 23°C and zero ionic strength.	123
Table A5 – Concentration ratios for each of the trace elements examined experimentally to the uranium (U) concentration in both feed seawater and desalination brine reject.	123

LIST OF FIGURES

- Figure 1.1** – Diagram of the nuclear fuel cycle depicting the various stages of the fuel’s life from its initial extraction (represented by U mining), to enrichment, processing, electricity generation in atomic and MOX fuel plants, and then either final disposal or recycle of spent fuel through reprocessing.¹² 3
- Figure 2.1** – Acrylonitrile and acrylic acid polymer samples are depicted above and include pure acrylonitrile (a), diblock copolymers with hydrophilic acrylic acid segments (b₁ and b₂), and randomly assorted acrylonitrile and acrylic acid copolymers (c). 15
- Figure 2.2** – Neutron beam path during reflectometry measurements: (a) in air and (b) under solvated conditions. A liquid cell is used during solvated measurements obstructing the top and bottom of the sample, thus the beam enters through the side of the substrate. 17
- Figure 2.3** – Neutron reflectivity data with fit in (a) air for (i) pure PAO ($\chi^2_v = 2.5$) and (ii) PAO-co-PAA ($\chi^2_v = 1.44$) and the same for (b) D₂O with χ^2_v of (i) 3.0 and (ii) 5.0, in descending order, vs momentum transfer and SLD profiles vs distance from the quartz interface in (c) air and (d) D₂O. 19
- Figure 2.4** – Neutron reflectivity data (RQ⁴) with modeling fits in (a) air for samples (i) B ($\chi^2_v = 2.67$) and (ii) A ($\chi^2_v = 1.87$), and under solvated conditions for (b) sample A and (c) sample B. Solvated measurements include (i) D₂O ($\chi^2_v = 2.13$ and $\chi^2_v = 2.18$), (ii) after conditioning ($\chi^2_v = 2.14$ and $\chi^2_v = 2.17$), and (iii) in the salt solution ($\chi^2_v = 1.80$ and $\chi^2_v = 2.53$) for samples A and B, respectively. Modeled scattering length density (SLD) profiles vs distance from the quartz interface (d) in air and under solvated conditions for samples (e) A and (f) B 21
- Figure 3.1** – Adsorption of Ca and Mg (mg/g adsorbent) and adsorbent surface speciation of ITA²⁻, HITA⁻, and H₂AO⁺ (mol/kg adsorbent) predicted for pH 6.5 – 9.0. 37

Figure 3.2 – U uptake (mg U/g adsorbent) over time (weeks) for AFI adsorbent in feed seawater and brine reject solution. Error is approximately 5%, as reported by Gill et al. (2016). ⁴	40
Figure 3.3 – Predicted effects of total IDO and pH on adsorption of U in (a) feed seawater and (b) brine reject solution.	43
Figure 3.4 – Predicted effects of total IDO and pH on adsorption of V in (a) feed seawater and (b) brine reject solution.	44
Figure 4.1 – Schematic of recirculating flume system used in adsorption experiments (the schematic is a courtesy from the MicroBio Engineering Inc). This setup was operated at environmental conditions, at an average temperature of 10.8°C with 40-micron pre-filtered seawater, to more realistically simulate field deployment conditions.	53
Figure 4.2 – Schematic of the cages containing adsorbent braids in the raceway where Cage C contains three large braids (60 g per braid) and every other cage has 10 small braids (10 g per braid).	54
Figure 4.3 – Simulated (lines) and experimental adsorption capacities (mg adsorbate/g adsorbent) for V, U, and Zn over a 28 day exposure period for (a) Cage B small braids and (b) Cage C large braids in the raceway. The analytical error is approximately 5%, as reported by Gill et al. (2016). ¹²	61
Figure 4.4 – Measured and simulated (lines) aqueous concentrations (ppb) for U and V in the raceway over a 28-day exposure period. The analytical error is approximately 5%, as reported by Gill et al. (2016). ¹²	62
Figure 5.1 – Complete schematic of continuous flow aging system; dry air lines and water vapor generator were not used in this study.	74
Figure 5.2 – Normalized Ag K-edge XANES of AgZ aged in (a) 1% NO in N ₂ and (b) 2% NO ₂ in dry air.	81
Figure 5.3 – Proportion of each Ag species present in 2% NO ₂ aged mordenite samples as a percent of total Ag before (left) and after (right) I ₂ adsorption determined from linear combination fitting of XANES data.	82

Figure 5.4 – Proportion of each Ag species present in 1% NO aged mordenite samples as a percent of total Ag before (left) and after (right) I ₂ adsorption determined from linear combination fitting of XANES data.	84
Figure 5.5 – Simulation results compared against XAS combination fitting data for aging at 150°C in 2% NO ₂ in dry air for aging times up to two months.	89
Figure 5.6 – Simulation results compared against XAS combination fitting data for aging at 150°C in 1% NO in N ₂ and aging times up to two months.	91
Figure 6.1 – Normalized Ag K-edge XANES of Ag Aerogel aged in dry air at 150°C for one month, two months, four months, and six months.	106
Figure 6.2 – The portion of each Ag species present in 150°C dry air aged Ag aerogel samples as a percent of total Ag determined from linear combination fitting of XANES data.	107
Figure 6.3 – Simulation results compared against XAS combination fitting data (one, two, four, and six months) and activated aerogel estimate from I ₂ loading experiments (three days, one week, and two weeks) on aerogel aged in dry air at 150°C.	110
Figure B1 – Linear combination fitting (LCF) for Ag ⁰ Z aged in 2% NO ₂ in dry air using reference compounds Ag ⁰ Z, Ag ₂ O, AgNO ₃ , and AgZ. Experimental data are in black and the LCF is in red. Reference standards used to achieve the LCFs are plotted beneath and scaled according to their contribution to the fit.	125
Figure B2 – Linear combination fitting (LCF) for Ag ⁰ Z aged in 2% NO ₂ in dry air and then exposed to iodine (I ₂) at a concentration of 50 ppmv in dry air using reference compounds Ag ⁰ Z, Ag ₂ O, AgNO ₃ , AgZ, and AgI. Experimental data are in black and the LCF is in red. Reference standards used to achieve the LCFs are plotted beneath and scaled according to their contribution to the fit.	126

- Figure B3** – Linear combination fitting (LCF) for Ag^0Z aged in 1% NO in N_2 using reference compounds Ag^0Z , Ag_2O , AgNO_3 , and AgZ . Experimental data are in black and the LCF is in red. Reference standards used to achieve the LCFs are plotted beneath and scaled according to their contribution to the fit. 127
- Figure B4** – Linear combination fitting (LCF) for Ag^0Z aged in 1% NO in N_2 and then exposed to iodine (I_2) at a concentration of 50 ppmv in dry air using reference compounds Ag^0Z , Ag_2O , AgNO_3 , AgZ , and AgI . Experimental data are in black and the LCF is in red. Reference standards used to achieve the LCFs are plotted beneath and scaled according to their contribution to the fit. 128
- Figure B5** – Structure of mordenite crystal where 12-member $7.0 \times 6.5\text{\AA}$ main channels, parallel 8-member $5.7 \times 2.6\text{\AA}$ side channels, and 5-member side pockets with approximate binding sites shown. 129
- Figure B6** – Linear combination fitting (LCF) for Ag^0 aerogel aged in dry air using reference compounds for unaged Ag^0 aerogel, Ag_2S , and Ag_2SO_4 . Experimental data are in black and the LCF is in red. 129

LIST OF COMMON SYMBOLS

Ag – Silver

Ag⁰ – Reduced/Metallic Silver

Ag₂O – Silver Oxide

AgNO₃ – Silver Nitrate

Ag₂S – Silver sulfide

Ag₂SO₄ – Silver Sulfate

AgI – Silver Iodide

AgZ – Silver Exchanged Mordenite

Ag⁰Z – Reduced Silver Exchanged Mordenite

C – Carbon

Ca – Calcium

Cu – Copper

Fe – Iron

H₂ – Hydrogen

H₂O – Water

I₂ – Inorganic Iodine

K – Potassium

Mg - Magnesium

Na – Sodium

N₂ – Nitrogen gas

NO – Nitric Oxide

NO₂ – Nitrogen Dioxide

O₂ – Molecular Oxygen

S – Sulfur

U – Uranium

V – Vanadium

Zn – Zinc

DG-OSPNEY – Discontinuous Galerkin Off-gas Separation and Recovery Model

MOOSE – Multiphysics Object Oriented Simulation Environment

NIST – National Institute of Standards and Technology

ORNL – Oak Ridge National Laboratory

US DOE – United States Department of Energy

SUMMARY

It is expected that, over the coming decades, demand for nuclear energy will rise alongside a general increase in global energy demand. To meet this growing demand, the availability of nuclear fuel resources will need to expand in a manner that is both economically competitive and environmentally sustainable. There are two primary ways with which the availability of nuclear fuels may be expanded. The first is to develop new sources of nuclear fuel while the second would be to extend the usable lifetime of already available resources. In the first case, uranium recovery from seawater is an attractive possibility not only because the oceanic reserve of uranium is far larger than known terrestrial reserves, but also because it has much less significant environmental consequences than traditional mining. On the other end, extending the usable lifetime of fuel resources currently available would, necessarily, require reprocessing of spent fuels. A large majority of the material in spent nuclear fuels is reusable and can be recovered for power generation. This would, in turn, lessen the need for extraction of new fuel resources. During reprocessing, however, a number of off-gases, including radioactive iodine in organic and inorganic forms, are released. Of these, iodine is the most important and must be removed from reprocessing off-gas before release to the environment. Thus, off-gas treatment is an inescapable aspect of nuclear fuel reprocessing. As such, the work described here is divided into two parts: first focusing on the recovery of uranium from seawater and then investigating adsorbents for iodine capture from nuclear fuel reprocessing off-gas.

While there are many reasons that make uranium recovery from seawater attractive, the low concentration of uranium and presence of many potential competitors make the process quite challenging. Adsorbents synthesized by grafting amidoxime polymers to an inert backbone are currently considered the most promising materials for uranium recovery. Fine tuning of the adsorbent is, nevertheless, still necessary to attain the desired performance. To this end, the conformation, or spatial arrangement, of the amidoxime polymers in a model film system was analyzed through neutron reflectometry. The conformation of an adsorbent polymer film is important to the capacity because it affects the film's diffusivity and the accessibility of adsorption sites. Adsorbent chains within the film may, for example, be very loosely associated with one another greatly reducing the density of the film. In this state, the barrier to diffusion is low thus increasing site accessibility and the overall rate of adsorption. Polymers with hydrophilic comonomers were shown to develop more favorable conformation than those without comonomers. Additionally, the configuration of comonomers in the film also affected conformation with the best performance observed in randomly configured copolymers. Adsorbent conditioning was also examined for diblock copolymers with one adsorbent and one comonomer film layer. After conditioning, the adsorbent film contracted slightly while the density of the comonomer film at the interface between the two layers increased. This effect was a result of sodium ions, released by the sodium bicarbonate conditioner, which possess kosmotropic properties in solution. Kosmotropic ions reduce the favorability of polymer-water bonds. As a result, polymer chains become more closely associated through inter and inter polymer bonding. The effect of the kosmotropic ions was more pronounced on the hydrophilic comonomer. Such a change in

the conformation could lead to a decline in the adsorption capacity or greatly slow the rate of adsorption by limiting site accessibility and increasing the barrier to diffusion.

The effect of competition was then examined by comparing uranium adsorption in seawater to adsorption in desalination brine reject. Brine reject has a much higher concentration of uranium than seawater and by incorporating the adsorbent system into existing infrastructure the cost of recovery can be significantly reduced. Despite this higher concentration, uranium adsorption was lower in brine reject than in seawater. One major reason for this was competition from iron and vanadium which both attained far higher capacities in the brine solution. Another likely reason for uranium's lower adsorption capacity and slower adsorption kinetics is the kosmotropic effect observed previously since kosmotropes are present at much higher concentrations in brine than in seawater. Chemisorption modeling was performed to assess this possibility and it was shown that uranium, of all the five trace metals tested, was the most susceptible to adsorbent ligand availability in brine. Thus even a small change in the effective density of surface ligands could reduce uranium adsorption notably.

For the final section on the recovery of uranium from seawater, a potential alternative means of adsorbent synthesis was assessed and compared against previously developed grafted adsorbents. This adsorbent was synthesized directly from commercially available acrylonitrile fibers and conditioned with a low cost alternative to the chemical generally used for the grafted adsorbent. A raceway flume feed with coarsely filter seawater was used to more accurately represent deployment conditions. The alternative adsorbent compared favorably to the grafted adsorbent for short term adsorption at lower temperatures. Kinetic modeling was then used to predict the long

term uranium capacity and to estimate performance at higher temperatures. These predictions indicate that the adsorption advantage of the alternative adsorbent would become less significant as the temperature increased. Thus by about 30°C, the grafted material's uranium adsorption capacity would be greater than the alternative adsorbent. The alternative adsorbent, however, has the additional advantage of adsorbing far less vanadium, which is a significant competitor to uranium, than the grafted adsorbent. Thus, this adsorbent could potentially be applied to uranium recovery in solutions with high vanadium concentration such as the brine reject previously discussed.

Silver adsorbents are currently considered the most promising materials for iodine capture in nuclear fuel reprocessing off-gas due to the high affinity between silver and iodine. Two types of silver adsorbents, (i) reduced silver exchanged mordenite and (ii) reduced silver functionalized silica aerogel, were examined in this work. While reduced silver adsorbents are known to have a high capacity for iodine, how these materials interact with other off-gas species is not well understood. For example, when exposed to oxygen, water vapor, nitric oxide, or nitrogen dioxide for long periods of time the iodine capacity of both adsorbents is known to drop considerably, a phenomenon we call here aging. The underlying processes that produce this capacity drop are, however, not known and have not been studied. In the case of reduced silver mordenite, aging in 1% nitric oxide in nitrogen gas and 2% nitrogen dioxide in dry air were examined. It was determined that the primary cause of aging was dissociative adsorption of nitric oxide catalyzed by sodium impurities and coadsorption of nitrogen dioxide and oxygen, with both processes forming silver nitrate. The resulting silver nitrate then migrates into the mordenite crystal channels exchanging at available protonated sites, effectively returning

the silver to its unreduced form. Silver nitrate not able to exchange forms clusters within the mordenite crystal channels stabilized through interactions with the channel walls. These clusters then prevent iodine from diffusing through the mordenite crystal channels where it would normally be able to adsorb at silver binding sites. As a result, the vast majority of iodine adsorbed in heavily aged samples was on silver nitrate.

The aging effect in silver aerogel is much less significant than in silver mordenite. This can be attributed to two factors. First the aerogel has no metal impurities and, as a result, does not adsorb either water vapor or nitric oxide at the experimental temperatures. Secondly, the thiol groups used to functionalize the aerogel adsorb to metallic silver forming a protective monolayer across the surface. Nevertheless, thiols also play a significant part in aerogel aging. In dry air aged aerogel samples, formation of silver sulfide and silver sulfate was observed. Silver sulfide is formed as a result of thiols adsorbing to irregular silver surface sites where the alkyl group of the thiol is cleaved from the surface bound sulfide. Silver sulfate is the product of sulfur oxidation brought about from interactions between surface bound thiols and subsurface oxygen species.

This research, ultimately, serves to advance the long term economic and environmental sustainability of nuclear energy by developing an alternative to traditional uranium mining and by assisting in the design of systems for more efficient utilization of nuclear fuel resources.

CHAPTER 1: INTRODUCTION

1.1 Background

Adsorption, broadly speaking, is a surface phenomenon whereby an adsorbate originating from either a gas or a liquid bulk phase adheres to the surface of a solid adsorbent. This overarching process can be sub-divided into the two principal categories of chemisorption and physisorption.^{1,2} In the case of chemisorption, the adsorbate is bound to the adsorbent surface through a site-specific, and in some cases irreversible, chemical reaction yielding a chemically distinct adsorbed phase.³ Furthermore, the site specific nature of chemisorption generally precludes the formation of more than one layer of adsorbate on the adsorbent's surface. Physisorption, on the other hand, proceeds reversibly without changing the adsorbate's chemical state as a result of van der Waals and other intermolecular forces.³ These two sub-categories of adsorption encompass a wide variety of potential applications in contaminant removal and resource recovery from both gas phase and liquid solutions. Some of these potential applications include but are not limited to (i) wastewater treatment,^{4,5} (ii) off-gas treatment to remove carbon dioxide,⁶ volatile organic compounds,⁷ and radioactive noble gases,⁸ and (iii) recovery of soluble metal ions from mine tailings.⁹ The work described here focuses on the development of adsorbents for applications in the area of nuclear fuel resources.

1.2 Motivation

The development of reliable and efficient energy resources represents one of the most significant areas of research in environmental engineering. With the global demand

for energy expected to rise by just over 48% between 2012 and 2040, it is likely that an even greater emphasis will be placed upon the development of new energy technologies.¹⁰ This is particularly true considering our present, and potentially future, reliance on fossil fuels which are one of the largest sources of anthropogenic greenhouse gases and a significant contributor to climate change. To reduce our reliance on fossil fuels, it will not only be necessary to continue the development of new renewable energy resources but also to improve the utilization of existing technologies. Nuclear energy is already one of the world's most widely used sources of energy and is expected to increase its energy generating capacity by as much as 56% over the next fifteen years.¹¹ To accommodate this expected growth in demand, access to nuclear fuel resources will need to be expanded while also developing technologies that enhance utilization of existing resources over their entire life cycle.

The life cycle of nuclear fuels, otherwise known as the nuclear fuel cycle (Figure 1.1),¹² is a complex series of interrelated processes beginning with extraction of uranium (U) ores through the various stages of enrichment, fuel processing, electricity generation, and finally disposal or reprocessing of spent fuel. The two components of the nuclear fuel cycle most important to the availability of nuclear fuel resources are the initial extraction of new raw resources and the reprocessing of spent fuels. New fuel resources have traditionally been obtained through mining of U ore, though these methods are problematic for two primary reasons. The first, and less pressing, concern is that traditional U reserves will be depleted within the next 135 years at the current rate of consumption or far sooner if demand rises significantly.¹³ The second relates to the pollution caused by U mining which can contaminate nearby surface water bodies and

groundwater systems with various radionuclides and trace metals.¹⁴⁻¹⁶ Thus developing alternative U resources that can be recovered while minimizing environmental impacts is desirable. At the other end of the cycle, spent nuclear fuels contain a large quantity of usable materials that without reprocessing are simply wasted. Incorporating reprocessing facilities into the fuel cycle would allow approximately 70% of the spent fuel to be recycled.¹⁷ Thus reprocessing would substantially cut down on waste and significantly extend the lifetime of nuclear fuel resources.

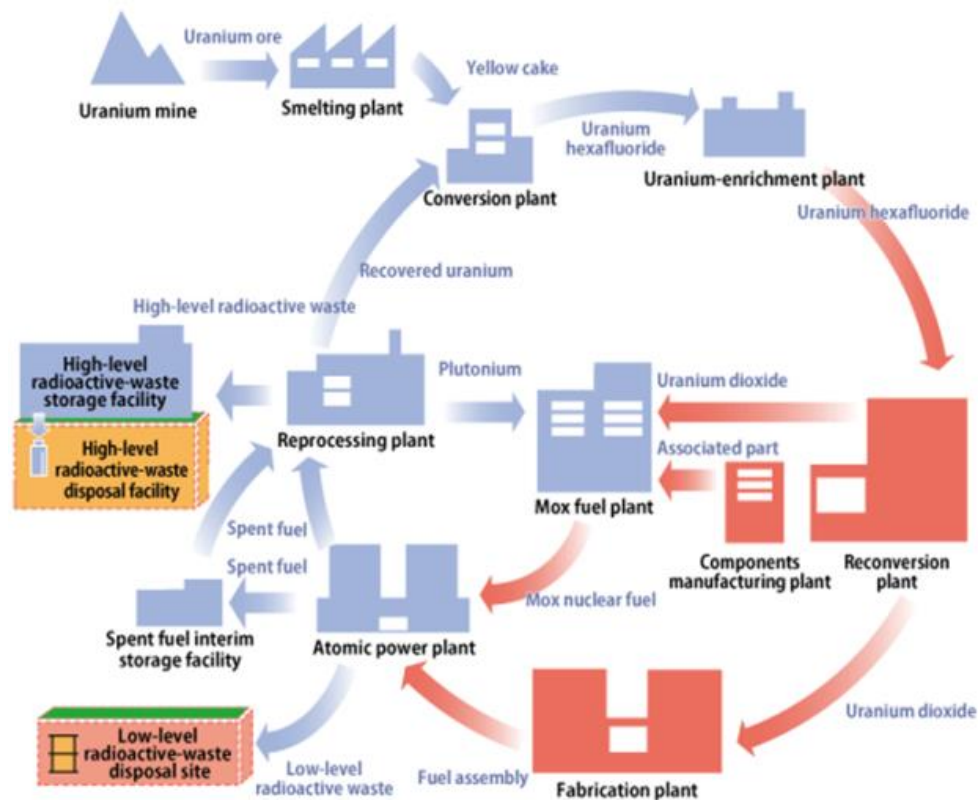


Figure 1.1. Diagram of the nuclear fuel cycle depicting the various stages of the fuel’s life from its initial extraction (represented by U mining), to enrichment, processing, electricity generation in atomic and MOX fuel plants, and then either final disposal or recycle of spent fuel through reprocessing.¹²

Considering alternatives to traditional U mining, one potential source of U is oceanic U which represents a reserve about 500 times larger than all known terrestrial U.¹⁸ The recovery of U from seawater has been an area of interest since at least the early 1950s. Numerous materials have been examined during the nearly seven decades long period since then, though amidoxime based adsorbents are currently considered the most promising.¹⁸ Development of amidoxime based adsorbents for U recovery from seawater began in Japan during the early 1980s. These early studies led to a number of marine tests during the 1990s and early 2000s.¹⁹⁻²¹ Marine testing of amidoxime materials during this period culminated in the work of Seko and coworkers, who were able to recover one kg of U, with a capacity of 2.85 mg/g adsorbent, using a passive adsorbent system deployed for 240 days.²² In the United States, the US Department of Energy has sponsored research into the recovery of U from seawater since 2010.²³ Through this program, Oak Ridge National Laboratory (ORNL) has continued to develop amidoxime based adsorbents significantly improving upon earlier Japanese designs.^{24,25} Other recent studies in this area have also examined amidoxime based materials not derived from the designs previously studied by the Japanese.²⁶⁻²⁸ Despite these capacity improvements and considerable reductions in recovery costs relative to the Japanese adsorbents, the cost of U recovery with these materials remains too high for the process to be commercially viable.²⁹ As such, the continued development and optimization of amidoxime adsorbents are needed for commercial recovery of U from seawater.

In the case of nuclear fuel reprocessing, spent nuclear fuels contain a number of radioactive fission byproducts which are volatilized during reprocessing including iodine-129 in organic and inorganic forms, tritium, carbon-14, krypton-85, and xenon-135.³⁰ Of

these species, iodine is the most important as a result of its long half-life (~15.7 million years) which allows for accumulation in the environment. Furthermore, radioactive iodine emissions are regulated by both the US Environmental Protection Agency and Nuclear Regulatory Commission under the US Code of Federal Regulations Title 40 Part 190³¹ and Title 10 Part 20,³² respectively. As such, reprocessing off-gas must be treated to capture volatilized iodine. One of the two traditional methods for iodine capture is liquid scrubbing, however, the highly corrosive materials used in these systems make them costly to construct and maintain.^{33,34} The other method traditionally used for iodine capture has been solid adsorbent columns.³⁵ The lower cost of constructing and maintaining solid adsorbent systems has made the use of these material quite attractive, however, any material used must also resist degradation in the off-gas stream. For some time, silver (Ag) based solid adsorbents including various Ag zeolites (mordenite, faujasite, etc.), Ag nitrate impregnated alumina and silica, and Ag functionalized aerogels have been considered for iodine off-gas capture.³⁵⁻³⁷ Nevertheless, the behavior of these adsorbents in the off-gas stream, such as the interactions between the Ag adsorbent and off-gas constituents besides iodine, has not been studied in depth. Thus, before these adsorbent materials can be applied to iodine capture it will first be necessary to determine what processes are at play in the off-gas stream and how they influence the adsorbent's iodine capacity.

1.3 Scope and Objectives

The principal goals of the research presented here are to investigate the phenomena that influence the behavior of adsorbents needed for the development of

systems that shall improve the accessibility of nuclear fuel resources. This knowledge is then applied towards the implementation of predictive modeling tools and as an aid to the development of these adsorbent materials. The work present is divided into five chapters across two parts in accordance with the two media in which adsorption is investigated. Part I is divided into three chapters and discusses aqueous adsorption in the context of U recovery from seawater. Part II, on the other hand, delves into gaseous adsorption through two chapters focused on research into adsorbents for iodine capture from nuclear fuel reprocessing off-gas.

In CHAPTER 2, the effects of amidoxime polymer hydrophilicity, conditioning, and metal ion adsorption on graft chain conformation were investigated. Neutron reflectometry experiments were performed on model adsorbent polymer films consisting of pure amidoxime, amidoxime with acrylic acid comonomers in a random configuration, and a block copolymer with a lower layer of pure amidoxime and an upper layer of acrylic acid. Samples were tested first in air then in a liquid environment to assess the effect of hydrophilic comonomers. The block copolymers were then further tested after conditioning and after exposure to simulated seawater.

CHAPTER 3 focuses on the effect of competing metal ions on amidoxime's U adsorption capacity. Batch experiments were performed at ORNL with filtered seawater and desalination brine reject to assess the adsorption of U, vanadium (V), zinc (Zn), iron (Fe), calcium (Ca), magnesium (Mg), and copper (Cu). Alongside these experiments, modeling was performed to assess the speciation of competing ions and how that speciation influences adsorption. The potential effects of pH and ligand surface density

were also examined as an explanation for the disparity between experimental adsorption performance in brine reject versus the filtered seawater.

For CHAPTER 4, an alternative method of adsorbent synthesis was considered for the development of amidoxime based U adsorbents. Rather than grafting adsorbent polymer chains to an inert bulk fiber, the amidoxime adsorbent was synthesized directly from commercially available acrylonitrile fibers. Samples were synthesized by LCW Supercritical Technologies, formed into large and small sized braids, and tested at Pacific Northwest National Laboratory (PNNL) in a flume feed with coarsely filter seawater. Kinetic adsorption modeling was also performed to predict the adsorbent's long term capacity and to estimate the potential capacity at higher adsorption temperatures.

CHAPTER 5 marks the beginning of Part II covering Ag adsorbents for treatment of iodine in nuclear fuel reprocessing off-gas. In CHAPTER 5 specifically, the processes governing inorganic iodine (I_2) capacity degradation over time from exposure to other off-gas constituents, known as aging, were explored in a reduced Ag mordenite adsorbent. Aging experiments were performed at Syracuse University to determine the overall effect of material aging on the adsorption capacity. X-ray absorption spectroscopy experiments were performed at Argonne National Laboratory by researchers from ORNL to determine the speciation of Ag over time. With this information, the underlying processes responsible for aging were identified, reaction schemes for each aging environment were proposed, and then those reactions were used in modeling of aging. The final chapter of Part II, CHAPTER 6, is a direct continuation of CHAPTER 5 and includes very similar experimental and modeling methodologies. The most significant difference between the two is that CHAPTER 6 examines a reduced Ag functionalized

silica aerogel material prepared at PNNL instead of the Ag mordenite prepared at Syracuse University.

1.4 References

- 1) Tóth J. (Ed.), Adsorption Theory Modeling and Analysis, Marcel Dekker, Inc. New York, NY, 2002.
- 2) Benjamin, M.M. Water Chemistry, Waveland Press, Inc., Illinois, 2010.
- 3) Yiacoumi, S.; Tien, C. Kinetics of Metal Ion Adsorption from Aqueous Solutions, Kluwer Academic Publishers, Boston, MA, 1995.
- 4) De Gigi, S.; Lofrano, G.; Grassi, M.; Notarnicola, M. Characteristics and adsorption capacities of low-cost sorbents for wastewater treatment: A review. *Sustainable Materials and Technologies* **2016**, *9*, 10-40.
- 5) Huggins, T.M.; Haeger, A.; Biffinger, J.C.; Ren, Z.J, Granular biochar compared with activated carbon for wastewater treatment and resource recovery. *Water Research* **2016**, *94*, 225-232.
- 6) Bhatt, P.M.; Belmabkhout, Y.; Cadiau, A.; Adil, K.; Shekhan, O.; Shkurenko, A.; Barbour, L.J.; Eddaoudi, M. A Fine-Tuned Fluorinated MOF Addresses the Need for Trace CO₂ Removal and Air Capture using Physisorption. *J. Am. Chem. Soc.* **2016**, *138*, 9301-9307
- 7) Zhang, X.; Gao, B.; Creamer, A.E.; Cao, C.; Li, Y. Adsorption of VOCs onto engineered carbon: A review. *J. Haz. Mat.* **2017**, *338*, 102-123.
- 8) Liu, J.; Strachan, D.M.; Thallapally, P.K.; Enhanced noble gas adsorption in Ag@MOF-74Ni. *Chem. Commun.* **2014**, *50*, 466-468
- 9) Jiang, S.J.; Huang, L.; Nguyen, T.A.H.; Ok, Y.S.; Rudolph, V.; Yang, H.; Zhang, D. Copper and zinc adsorption by softwood and hardwood biochars under elevated sulphate-induced salinity and acid pH conditions. *Chemosphere* **2016**, *142*, 64-71.
- 10) *International Energy Outlook 2016 with Projections to 2040*; Energy Information Administration, U.S. Department of Energy, 2016.
- 11) *Energy, Electricity and Nuclear Power Estimates for the Period up to 2050: 2016 Edition*, Report IAEA-RDS-1/36; International Atomic Energy Agency, 2016.

- 12) Mitsubishi Nuclear Fuel, “MNF and the Nuclear Fuel Cycle”, <http://www.mnf.co.jp/en/business>
- 13) *Uranium 2016: Resources, Production and Demand*, NEA No. 7301, Organization for Economic Co-Operation and Development/Nuclear Energy Agency, International Atomic Energy Agency, 2016.
- 14) Kosior, G.; Steinnes, E.; Samecka-Cymerman, A.; Lierhagen, S.; Kolon, K.; Dothanczuk-Srodka, A.; Ziembik, A. Trace elements in native and transplanted *Fontinalis antipyretica* and *Platyhypnidium riparioides* from rivers polluted by uranium mining. *Chemosphere* **2017**, *171*, 735-740.
- 15) Antunes, S.C.; Pereira, R.; Marques, S.M.; Castro, B.B.; Goncalves, F. Impaired microbial activity caused by metal pollution: A field study in a deactivated uranium mining area. *Science of The Total Environment* **2011**, *410-411*, 87-95.
- 16) Wang, J.; Liu, J.; Li, H.; Song, G.; Chen, Y.; Xiao, T.; Qi, J.; Zhu, L. Surface Water Contamination by Uranium Mining/Milling Activates in Northern Guangdong Province, China. *Clean – Soil, Air, Water* **2012**, *40*, 1357-1363.
- 17) World Nuclear Association, *Processing of Used Nuclear Fuel*, <https://www.world-nuclear.org/information-library/nuclear-fuel-cycle/fuel-recycling/processing-of-used-nuclear-fuel.aspx> (Accessed November 8, 2019).
- 18) Kim, J.; Tsouris, C.; Mayes, R.T.; Oyola, Y.; Saito, T.; Janke, C.J.; Dai, S.; Schneider, E.; Sachde, D. Recovery of Uranium from Seawater: A Review of Current Status and Future Research Needs. *Sep. Sci. Technol.* **2013**, *48*, 367–387.
- 19) Takeda, T.; Saito, K.; Uezu, K.; Furusaki, S.; Sugo, T.; Okamoto, J. Adsorption and Elution of Hollow-Fiber Packed Bed for Recovery of Uranium from seawater. *Ind. Eng. Chem. Res.* **1991**, *30*, 185–190.
- 20) Egawa, H.; Kabay, N.; Shuto, T.; Jyo, A. Recovery of Uranium from Seawater. 14. System Arrangements for the Recovery of Uranium from Seawater by Spherical Amidoxime Chelating Resins Utilizing Natural Seawater Motions. *Ind. Eng. Chem. Res.* **1993**, *32*, 709–715.
- 21) Shimizu, T.; Tamada, M. Practical scale system for uranium recovery from seawater using braid type adsorbent. *Proc. Civ. Eng. Ocean* **2004**, *20*, 617–622.
- 22) Seko, N.; Katakai, A.; Hasegawa, S.; Tamada, M.; Kasai, N.; Takeda, H.; Sugo, T.; Saito, K. Aquaculture of Uranium in Seawater by a Fabric-Adsorbent Submerged System. *Nucl. Technol.* **2003**, *144*, 274-278.
- 23) Alexandratos, S.; Kung, S. Preface to the Special Issue: Uranium in Seawater. *Ind. Eng. Chem. Res.* **2016**, *55*, 4101-4102.

- 24) Gill, G.; Kuo, L.-J.; Janke, C.; Park, J.; Jeters, R.; Bonheyo, G.; Pan, H.-B.; Wai, C.; Khangaonkar, T.; Bianucci, L.; Wood, J.; Warner, M.; Peterson, S.; Abrecht, D.; Mayers, R.; Tsouris, C.; Oyola, Y.; Strivens, J.; Schlafer, N.; Addleman, R.; Chouyyok, W.; Das, D.; Kim, J.; Buesseler, K.; Breier, C.; D'Alessandro, E. The Uranium from Seawater Program at the Pacific Northwest National Laboratory: Overview of Marine Testing, Adsorbent Characterization, Adsorbent Durability, Adsorbent Toxicity, and Deployment Studies. *Ind. Eng. Chem. Res.* **2016**, *55*, 4264-4277.
- 25) Kim, J.; Tsouris, C.; Oyola, Y.; Janke, C.; Mayes, R.; Dai, S.; Gill, G.; Kuo, L.-J.; Wood, J.; Choe, K.-Y.; Schneider, E.; Linder, H. Uptake of Uranium from Seawater by Amidoxime-Based Polymeric Adsorbent: Field Experiments, Modeling, and Updated Economic Assessment. *Ind. Eng. Chem. Res.* **2014**, *53*, 6076-6083.
- 26) Piechowicz, M.; Abney, C.; Thacker, N.; Gilhula, J.; Wanmg, Y.; Veroneau, S.; Hu, A.; Lin, W. Successful Coupling of a Bis-Amidoxime Uranophile with a Hydrophilic Backbone for Selective Uranium Sequestration. *ACS Appl. Mater Interfaces* **2017**, *9*, 27894-27904.
- 27) Sun, Q.; Aguila, B.; Perman, J.; Ivanov, A.; Bryanstev, V.; Earl, L.; Abney, C.; Wojtas, L.; Ma, S. Bio-inspired nano-traps for uranium extraction from seawater and recovery from nuclear waste. *Nature Communications* **2018**, *9*, 1644.
- 28) Alexandratos, S.; Zhu, X.; Florent, M.; Sellin, R. Polymer-Supported Bifunctional Amidoximes for the Sorption of Uranium from Seawater. *Ind. Eng. Chem. Res.* **2016**, *55*, 4208-4216.
- 29) Das, S.; Liao, W.P.; Byers, M.; Tsouris, C.; Janke, C.J.; Mayes, R.T.; Schneider, E.; Kuo, L.J.; Wood, J.R.; Gill, G.A.; Dai, S. Alternative Alkaline Conditioning of Amidoxime Based Adsorbent for Uranium Extraction from Seawater. *Ind. Eng. Chem. Res.* **2016**, *55*, 4303-4312.
- 30) Ladshaw, A.; Wiechert, A.; Welty, A.; Lyon, K.; Law, J.; Jubin, R.; Tsouris, C.; Yiacoymi, S. Adsorbents and adsorption models for capture of Kr and Xe gas mixtures in fixed-bed columns. *Chemical Engineering Journal* **2019**, *375*, 122073.
- 31) EPA, Protection of environment: Chapter I-Environmental Protection Agency. Part 190-environmental radiation protection standards for nuclear power operations. Agency, U. E. P., Ed. US Environmental Protection Agency: Washington, DC (United States), 2010; Vol. 40 CFR 190.10.
- 32) NRC, Standards for protection against radiation. US Nuclear Regulatory Commission: Washington, DC (United States), 2012; Vol. 10 CFR 20.

- 33) Sodaye, H.; Nisan, S.; Poletiko, C.; Prabhakar, S.; Tewari, P.K. Extraction of uranium from the concentrated brine rejected by integrated nuclear desalination plants. *Desalination* **2009**, *235*, 9-32.
- 34) Nan, Y.; Tavlarides, L.; DePaoli, D. Adsorption of Iodine on Hydrogen-Reduced Silver-Exchange Mordenite: Experiments and Modeling. *Separations: Materials, Devices and Processes* **2016**, *63*, 1024-1035
- 35) Haefner, D and Tranter, T. Methods of Gas Phase Capture of Iodine from Fuel Reprocessing Off-Gas: A Literature Survey. INL/EXT-07-12299. Idaho National Laboratory, Idaho Falls, ID 2007.
- 36) Riley, R.; Vienna, J.; Strachan, D.; McCloy, J.; Jerden, J. Material and processes for the effective capture and immobilization of radioiodine: A review. *Journal of Nuclear Materials* **2016**, *470*, 307-326.
- 37) Huve, J.; Ryzhikov, A.; Nouali, H.; Lalia, V.; Auge, G.; Daou, T.J. Porous sorbents for the capture of radioactive iodine compounds: a review. *RSC Adv.* **2018**, *8*, 29248.

**PART I. RECOVERY OF URANIUM RESOURCES
FROM SEAWATER**

CHAPTER 2: Effect of Adsorbent Conformation

2.1 Introduction

Amidoxime based uranium (U) adsorbents grafted with hydrophilic comonomers, such as vinylphosphonic acid¹ and itaconic acid,² have a higher U adsorption capacity than adsorbents synthesized with only amidoxime. Since these comonomers do not directly affect U adsorption, their influence on polymer hydrophilicity and, by extension, polymer conformation is likely to be a contributing factor to this increased capacity.^{3,4} Polymer conformation is primarily determined by grafting density (surface coverage), polymer chain size (molecular weight), and polymer-polymer and/or polymer-medium interactions (electrostatic interactions and hydrogen bonding). Increasing grafting density or chain length will multiply the total number of adsorption sites but beyond a certain point diffusion limitations may restrict the number of accessible adsorption sites. This effect is believed to be caused by polymer crosslinking, which leads to polymer chains becoming intertwined as a result of attractive molecular interactions. These properties are particularly important because they can be manipulated to reduce the diffusion barrier, increase accessibility, and promote polymer brush stability through secondary polymer interactions.

The primary objectives of this study are to examine any effect of hydrophilic acid comonomers, alkali conditioning, and metal ion loading in simulated seawater on polymer conformation. Amidoxime and amidoxime acrylic acid copolymers are characterized by neutron reflectometry. Normally these copolymers take the form of adsorbent chains grafted to the surface of an inert bulk fiber using radiation induced graft

polymerization. For this analysis, a model system of copolymer graft chains deposited onto a substrate is used to create adequate contrast. Optimization of polymer conformation has the potential to produce the maximum number of effective adsorption sites and, in turn, improve the U adsorption capacity. The results of these experimental studies, combined with an understanding of the influence of grafting density and chain size, will aid in the optimization of graft-chain conformation.

2.2 Materials and Methods

2.2.1 Sample Preparation

Samples (Figure 2.1) were prepared using a multistep process beginning with precursor synthesis using Atom Transfer Radical Polymerization (ATRP). Substrate surfaces were cleaned by sonication at room temperature in acetone and isopropyl alcohol for 20 min each, followed by an additional 24 min of oxygen cleaning. Triethoxysilane ATRP initiators were synthesized first and acted as polymer end-groups for attachment to the quartz substrate. All monoblock polymers were prepared with a 50% by volume dimethyl sulfoxide (DMSO) solution with a monomer concentration of 0.4% by weight. For the DMSO solution, triethoxysilane had a molarity of 1.0 while copper (I) bromide and 2,2'-bipyridine were added at a molarity of 0.5 and 1.5, respectively, at 65°C. Randomly configured monoblock copolymers were prepared in solutions containing acrylonitrile and tert-butyl acrylate at a desired ratio.

After polymerization of the first block, substrates were removed from solution, sonicated in fresh DMSO for 30 min at 50 °C, and rinsed with DSMO solution to remove chains not chemically bonded to the substrate's surface. Substrates were then dried in

nitrogen (N₂) and vacuum dried for one day at 40 °C. For diblock copolymers, polymerization of the second block was carried out in a 20% by volume tert-butyl acrylate dimethylformamide (DMF) solution. After purging the acrylonitrile monoblock with Argon for 30 min, copper (I) bromide was added to begin the polymerization of the second block. After polymerization of the second block, the substrate was removed from solution, rinsed using a DMF/methanol solution, and sonicated in fresh DMF for 30 min at 50 °C. The sample was then rinsed again with DMF/methanol, dried under N₂, and finally annealed in a vacuum for two days at 135 °C to ensure block segregation.

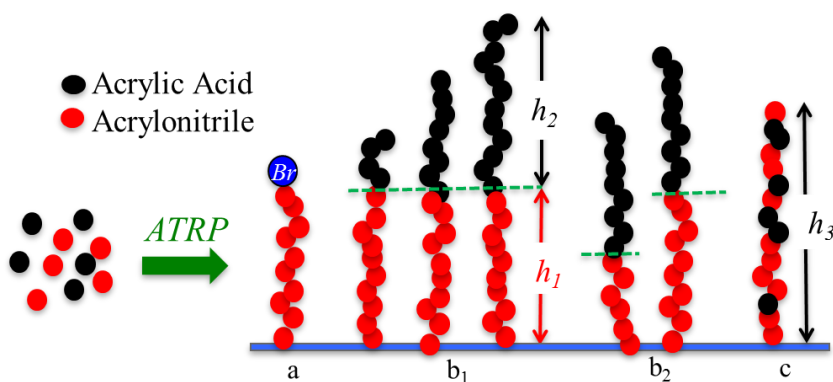


Figure 2.1. Acrylonitrile and acrylic acid polymer samples are depicted above and include pure acrylonitrile (a), diblock copolymers with hydrophilic acrylic acid segments (b₁ and b₂), and randomly assorted acrylonitrile and acrylic acid copolymers (c).

Amidoximation and hydrolysis recipes were based on previously established procedures.⁴ Hydrolysis was conducted in a DMSO/trifluoroacetic acid solution over the course of 20 hr to remove the butyl-acrylate molecule from the tert-butyl acrylate polymer, forming polyacrylic acid (PAA). Hydrolyzed polymer-bearing substrates were then soaked in DI water for one hr. Amidoximation was conducted in a DI water/methanol solution with neutralized hydroxylamine hydrochloride, which provides

the hydroxylamine molecules that react with the cyano group of the acrylonitrile polymer, forming polyamidoxime (PAO). The substrate was submerged in this solution at 77 °C for one day. Substrates were rinsed with DI water then N₂ dried.

2.2.2 Neutron Reflectometry

Reflectometry experiments were conducted at the Oak Ridge National Laboratory (ORNL) Spallation Neutron Source using the BL-4B Liquids Reflectometer and at the National Institute of Standards and Technology (NIST) Center for Neutron Research using the NG7 Cold Neutron Reflectometer. Reflectivity data were obtained as a function of the momentum transfer (Q) between 0.01 and 0.2 Å⁻¹ with $Q = 4\pi\sin\theta/\lambda$, where θ is the incident angle and λ is the neutron beam wavelength. For ORNL's BL-4B Liquids Reflectometer, data were obtained at seven incident angles while λ was varied between 2.5 Å and 17.5 Å at each angle, with an instrument resolution of $\Delta Q/Q = 0.05$. A final reflectivity profile was obtained by reducing the data for all seven angles simultaneously. NIST's NG7 Cold Neutron Reflectometer operates over a smaller range of λ from 2.35 to 5.5 Å, while varying the incident angle to obtain a single reflectivity profile. Substrates were tested under both dry and solvated conditions (Figure 2.2), with additional measurements taken for diblock samples after alkali conditioning and in simulated seawater. Dry measurements in air were taken at room temperature and atmospheric pressure. Heavy water (D₂O) was used in all liquid measurements because it provides good contrast with the sample and produces negligible incoherent neutron scattering. When using normal water, it is impossible to obtain a total reflection plateau, and this limitation significantly increases the difficulty of analyzing the data. Additionally,

because water has greater incoherent neutron scattering, its use would lead to increased background scattering at high Q values making measurements more difficult, time consuming, and limited in Q range.

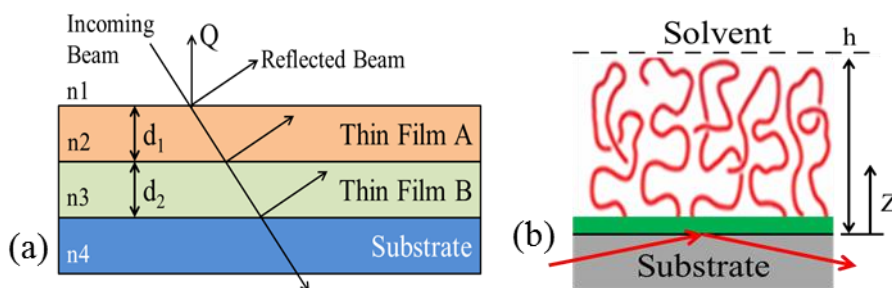


Figure 2.2. Neutron beam path during reflectometry measurements: (a) in air and (b) under solvated conditions. A liquid cell is used during solvated measurements obstructing the top and bottom of the sample, thus the beam enters through the side of the substrate.

Reduced data from these experiments were fit using Igor Pro-MotoFit from the Igor Pro reflectivity analysis package and nonlinear least-squares regression.⁵ The desired quality of fitting was defined by reduced chi squared value of $\chi^2_v < 3.0$ for air measurements and $\chi^2_v < 6.0$ for solvated measurements. The PAA layer for diblock samples was fit using a system of sublayers with variable Scattering Length Density (SLD) and a fixed thickness of 45 Å and a roughness of 9.0 Å. One exception to this approach was the final sublayer before transitioning to D₂O which has a variable roughness. The roughness of the Quartz-PAO transition was restricted to a value no greater than 15 Å while the PAO-PAA roughness was not allowed to exceed 10 Å. Conservation of mass was further confirmed to be within 5% based on the physical structure. The sample's mass after solvation was calculated by solving for the area under the volume fraction profile for each layer to find a predicted air thickness. This predicted

thickness was compared to the actual air thickness obtained from the measurements taken in air. Since SLD is additive, the polymer volume fraction can be determined by considering the contributions of D₂O and the polymer to the SLD.

2.3 Results and Discussion

The random copolymer configuration (PAO-co-PAA) and pure PAO monoblock samples were prepared with a similar molecular weight (~40,000 g/mol) and grafting density of 0.16 chains/nm². These samples were almost identical, with the principal exception that the PAO-co-PAA sample contained randomly distributed hydrophilic comonomers with a molar ratio of PAO:PAA = 0.67:0.33. The reflectivity profiles for pure PAO and PAO-co-PAA (Figure 2.3) are remarkably similar. Reflectivity profiles were shifted for ease of comparison. Furthermore, when these films are modeled, the SLD profiles, which are used to determine film thickness based on reflectivity, are essentially the same yielding a film thickness of approximately 95 Å for both samples. These data also provide evidence that the preparatory process used is properly controlled.

Additional experiments were performed in D₂O at neutral pD (pH in D₂O) with the pure PAO and PAO-co-PAA samples. Sample reflectivity differs significantly from the results in air as expected. Pure PAO is shown to extend to approximately 180 Å, which is an increase of nearly 90% over the dry film thickness. The film thickness for PAO-co-PAA samples also increased to an approximate thickness of 280 Å, which represents an extension of 195% from the initial air thickness. This additional extension is a result of the hydrophilic PAA comonomers which help to compensate for the hydrophobic properties of PAO. Considering that past experimental data^{1,2} have shown

that hydrophilic segments yield increased U adsorption capacity, these results are a clear indication of the relationship between hydrophilicity, polymer conformation, and capacity.^{3,4} The results obtained for the randomly distributed copolymers show that polymer chains extend significantly further when hydrophilic segments are incorporated. This additional extension, in turn, reduces the barrier to U diffusion and allows more adsorption sites to be utilized yielding an increased adsorption capacity.

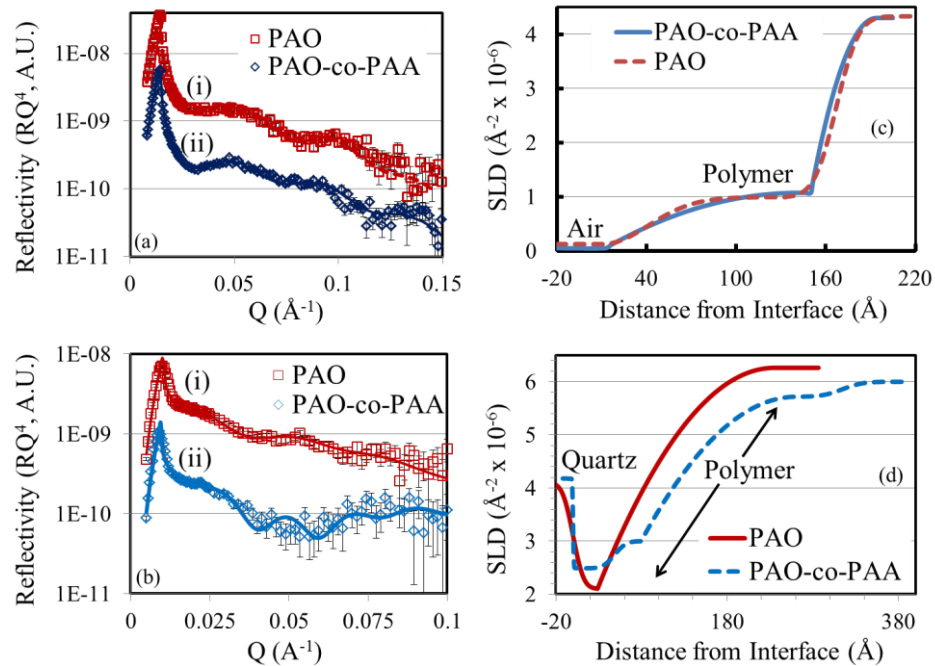


Figure 2.3. Neutron reflectivity data with fit in (a) air for (i) pure PAO ($\chi^2_v = 2.5$) and (ii) PAO-co-PAA ($\chi^2_v = 1.44$) and the same for (b) D₂O with χ^2_v of (i) 3.0 and (ii) 5.0, in descending order, vs momentum transfer and SLD profiles vs distance from the quartz interface in (c) air and (d) D₂O.

The PAO layer of the diblock samples was kept at a constant approximate thickness of 55 Å for all samples and was deuterated (d-PAO) to improve contrast with the PAA layer. PAA thickness was varied for each sample. Thus, deuterated acrylonitrile

deposition was the same for both samples (A and B), while second-block polymerization was carried out at different temperatures. Poly-tert-butyl acrylate block addition occurred over a 4-hr period with two similar DMF polymer solutions. The temperature was kept at 45°C and 85°C for samples A and B, respectively. Amidoximation and hydrolysis were conducted after deposition to convert deuterated acrylonitrile and poly-tert-butyl acrylate to d-PAO and PAA, respectively. Sample A (Figure 2.4), the shorter of the two samples, had a PAA thickness of ~145 Å and a total thickness of ~200 Å. Sample B had a PAA thickness of ~185 Å with a total thickness of ~240 Å. In D₂O at neutral pD, the d-PAO layers of samples A and B swelled by approximately 100% and 150%, respectively, while the PAA layer swelled by ~180% and ~170% for samples A and B, respectively. The samples reached a total thickness of 405 Å for sample A and 495 Å for sample B. This swelling is expected given that samples generally expand under liquid conditions, though it is not as significant as the swelling observed in D₂O for PAO-co-PAA samples. These results are further evidence of the positive relationship between polymer hydrophilicity and conformation. The configuration of the film, nevertheless, also plays an important part in film conformation with the PAO-co-PAA polymer swelling by a much greater margin with much less PAA. Multiple layers were used in the SLD model for PAA to yield more accurate fitting results and was based on similar approaches reported in literature.^{6,7}

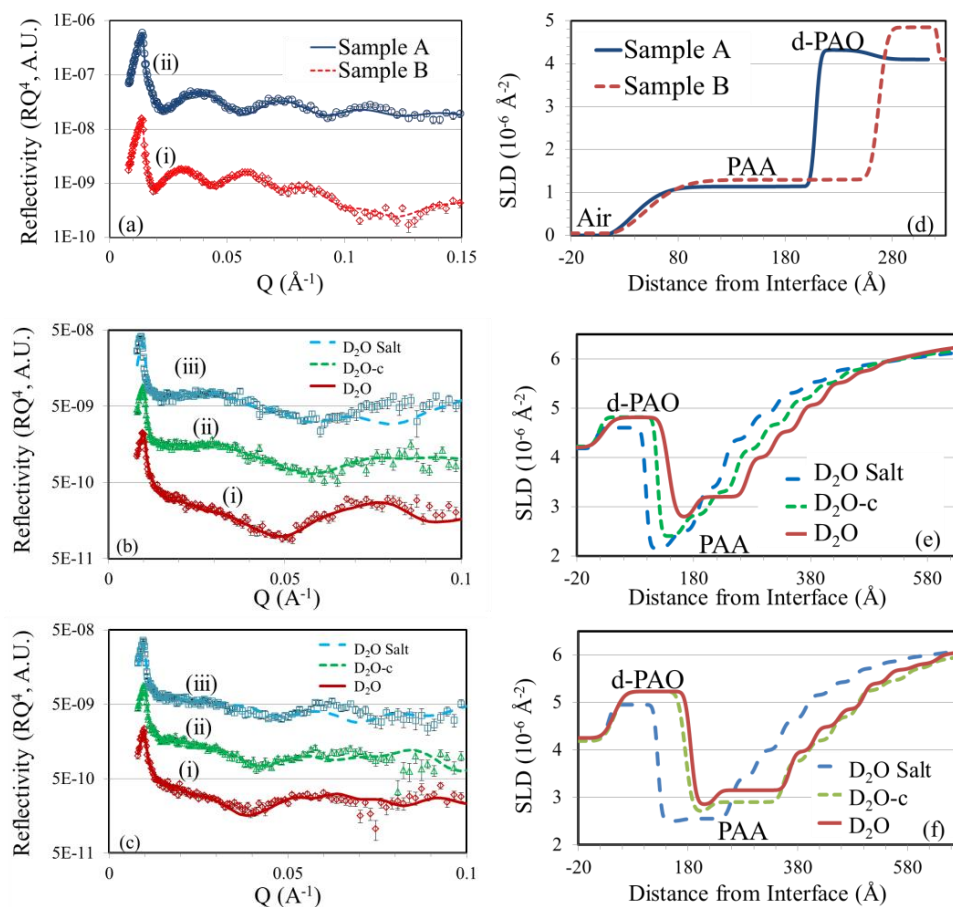


Figure 2.4. Neutron reflectivity data (RQ^4) with modeling fits in (a) air for samples (i) B ($\chi^2_v = 2.67$) and (ii) A ($\chi^2_v = 1.87$), and under solvated conditions for (b) sample A and (c) sample B. Solvated measurements include (i) D_2O ($\chi^2_v = 2.13$ and $\chi^2_v = 2.18$), (ii) after conditioning ($\chi^2_v = 2.14$ and $\chi^2_v = 2.17$), and (iii) in the salt solution ($\chi^2_v = 1.80$ and $\chi^2_v = 2.53$) for samples A and B, respectively. Modeled scattering length density (SLD) profiles vs distance from the quartz interface (d) in air and under solvated conditions for samples (e) A and (f) B.

In U adsorption applications, alkali conditioning increases the adsorption capacity dramatically. This is caused, in part, by the conversion of some amidoxime groups to carboxylate, which increases the polymer's hydrophilicity and, by extension, the adsorption capacity.^{8,9} That increase in hydrophilicity comes at the expense of losing a fraction of the adsorption sites. After alkali conditioning in a solution of 1.0 M sodium bicarbonate (NaHCO_3), the d-PAO layer for sample A dropped from an initial thickness in D_2O of ~ 110 Å to ~ 100 Å, while the thickness of sample B decreased from ~ 140 Å to ~ 130 Å (Table 2.1). Overall, there was no significant change in the PAA thickness, though the internal structure of the layer changed significantly. The innermost sublayers of the model, which accounts for the bulk of polymer mass, experienced a notable drop in SLD, while the outer layers' SLD increased. This change in SLD corresponds to an increase in the polymer volume fraction near the d-PAO-PAA interface. Thus in both samples, the mass of the PAA layer is becoming more densely concentrated at the d-PAO-PAA interface after alkali conditioning. Since NaHCO_3 is a relatively weak base, polymer damage from conditioning is unlikely to be the cause of this change in the polymer's internal structure. The kosmotropic effects of sodium (Na) ions, and to a lesser extent carbonate, offer another explanation.

Kosmotropes influence polymer conformation by increasing the favorability of hydrogen-hydrogen bonds in water. This effect, in turn, reduces the favorability of polymer-water bonds and increases the likelihood of polymer-polymer interactions which lead to excessive crosslinking and eventually to polymer collapse at sufficiently high concentrations.^{10,11} Additionally, kosmotropic effects have been observed in 1.0 M sodium chloride (NaCl) solutions¹² and for polymers containing PAA at the same molar

concentration of NaCl.¹³ Due to the inert nature of chloride, 1.0 M NaCl would be of comparable strength to the 1.0 M NaHCO₃ solution used. Thus, the increased density of PAA observed after alkali conditioning is likely caused by heavy inter- and intra-polymer crosslinking promoted by the kosmotropic effects of the NaHCO₃ that is used in conditioning. The difference between samples A and B is probably the result of additional crosslinking in sample A. This is likely due to the additional relative extension in D₂O that sample A's PAA layer experienced, thus allowing for diffusion to occur more rapidly.

Table 2.1. Summary of film thickness (T) obtained from neutron reflectivity under different measurement conditions. Roughness (R) listed for single block polymers (PAO and PAO-co-PAA) is the interfacial polymer-to-air roughness; d-PAO roughness is for quartz to polymer transition; PAA roughness is polymer to D₂O; inter-polymer roughness is 10Å for all samples.

Sample	Air		D ₂ O		D ₂ O after Conditioning		After Metal Ion Adsorption	
	T (Å)	R (Å)	T (Å)	R (Å)	T (Å)	R (Å)	T (Å)	R (Å)
N/A	95	30	180	50	N/A	N/A	N/A	N/A
PAO	95	30	280	25	N/A	N/A	N/A	N/A
PAO-co-PAA	95	30	280	25	N/A	N/A	N/A	N/A
Sample A (d-PAO)	55	15	110	10	100	5	85	10
Sample A (PAA)	145	28	405	80	405	125	405	120
Sample B (d-PAO)	55	10	140	15	130	15	90	10
Sample B (PAA)	185	10	495	90	495	110	495	90

The conditioned samples were then measured in a D₂O solution with a comparable pD and salt concentration to seawater that served as a simulated seawater

environment to examine the effect of metal ion loading on polymer conformation. This solution includes U, but also competing ions such as vanadium (V) and iron (Fe) that would also be adsorbed when deployed in the ocean. Kosmotropic effects are less important in this solution due to the lower concentration of kosmotropes, particularly Na ions, in the sea-salt solution though they are still present. The d-PAO thickness of sample A declined again to 85 Å (a 23% drop relative to the D₂O thickness), while sample B dropped to 90 Å (a 35% relative drop compared to D₂O). The final film thickness was 490 Å and 585 Å for samples A and B, respectively. An increase in polymer density is again observed for both samples, though, in this case, the effect is significantly more pronounced in the d-PAO layer. While the metal ions adsorbed will slightly reduce the SLD on their own, this decline in film thickness and the accompanying increase in polymer density are predominantly the results of crosslinking. This crosslinking is the result of multisite adsorption where a metal ion, such as U or V, will form complexes with two or three amidoxime ligands.¹⁴ The similar d-PAO thickness observed for both samples after metal ion adsorption may indicate that the adsorbent films will tend to adopt a similar conformation when ions are adsorbed.

2.4 Conclusions

The primary objectives of this study were to examine the influence of hydrophilicity, alkali conditioning, and metal ion loading on polymer conformation. Previous experimental work has shown that by increasing polymer hydrophilicity, the U adsorption capacity also increases. Furthermore, the increase in capacity observed may be the result of conformational changes induced by the hydrophilic acid segments added to

the polymer. Pure PAO and PAO-co-PAA samples with similar molecular weights and grafting densities were prepared. The initial film thickness in air, observed for both samples, was ~ 95 Å. In D_2O , the PAO film thickness was nearly double its thickness in air while PAO-co-PAA's thickness increased to almost three times its initial air thickness. These results have shown that the effect of hydrophilicity on polymer conformation is to increase the degree of film swelling in solution. This swelling reduces the barrier to U diffusion and causes an increase in U capacity, thus explaining the observations made in past experiments.

Diblock samples, A and B, had a d-PAO thickness of approximately 55 Å and a total film thickness of 200 Å and 240 Å, respectively. The d-PAO thickness of both samples increased in D_2O by $\sim 100\%$ and $\sim 150\%$, respectively, relative to their thicknesses in air, while the PAA swelled by $\sim 180\%$ and $\sim 170\%$, for A and B, respectively. After conditioning, the d-PAO thickness of both samples declined by ~ 10 Å, with a negligible change in their PAA thickness. The internal structure of the PAA layer for both samples, however, changed after conditioning. The inner portions of the polymer film lost water, reducing the volume fraction of D_2O and increasing the density of polymer at the d-PAO-PAA interface. This increase in PAA density was likely caused by kosmotropic effects from the $NaHCO_3$ used in conditioning, which promoted polymer crosslinking and suppressed polymer-water hydrogen bonding. Sample A was affected significantly more than sample B during $NaHCO_3$ conditioning, indicating heavier crosslinking in sample A. This result is likely due to the greater relative extension of sample A in D_2O allowing for easier diffusion of kosmotropic ions. After metal ion adsorption in the salt solution, the d-PAO thickness declined to 85 Å, $\sim 77\%$ of the

thickness in D₂O, for sample A, and to 90 Å, ~65% of the D₂O thickness, for sample B. This result indicates that, as polymers undergo multisite adsorption of metal ions, crosslinking occurs between polymer chains and they begin to collapse.

2.5 Acknowledgments

The development of this chapter was a collaborative effort among my co-authors and myself and was the main subject of the following manuscript: A. Wiechert, W.P. Liao, E. Hong, C. Halbert, S. Yiacoumi, T. Saito, C. Tzouris. Influence of Hydrophilic Groups and Metal-Ion Loading on Polymer-Chain Conformation of Amidoxime-Based Uranium Adsorbents. Published in the Journal of Colloid and Interface Science on August 15th 2018.

2.6 References

- 1) Das, S.; Oyola, Y.; Mayes, R.T.; Janke, C.J.; Kuo, L.J.; Gill, G.; Wood, J.R.; Dai, S. Extracting Uranium from Seawater: Promising AI Series Adsorbents. *Ind. Eng. Chem. Res.* **2016**, *55*, 4103-4109.
- 2) Das, S.; Oyola, Y.; Mayes, R.T.; Janke, C.J.; Kuo, L.J.; Gill, G.; Wood, J.R.; Dai, D. Extracting Uranium from Seawater: Promising AF Series Adsorbents. *Ind. Eng. Chem. Res.* **2016**, *55*, 4110-4117.
- 3) Ladshaw, A.; Wiechert, A.; Das, S.; Yiacoumi, s.; Tzouris, C. Amidoxime Polymers for Uranium Adsorption: Influence of Comonomers and Temperature. *Materials* **2017**, *10*, 1268.
- 4) Saito, T.; Brown, S.; Chatterjee, S.; Kim, J.; Tzouris, C.; Mayes, R.; Kuo, L.J.; Gill, G.; Oyola, Y.; Janke, C.; Dai, S. Uranium recovery from seawater: Development of fiber adsorbents prepared via atom-transfer radical polymerization. *J. Mat. Chem.* **2014**, *2*, 14674-14681.
- 5) Nelson, A.; Muir, B.; Oldham, J.; Fong, C.; McLean, K.; Hartley, P.; Oiseth, S.; James, M. X-ray and neutron reflectometry study of glow-discharge plasma polymer films. *Langmuir* **2006**, *22*, 453-458.

- 6) Hollmann, O.; Gutberlet, T.; Czeslik, C. Structure and Protein Binding Capacity of a Planar PAA Brush. *Langmuir* **2007**, *23*, 1347-1353.
- 7) Evers, F.; Reichart, C.; Steitz, R.; Tolan, M.; Czeslik, C. Probing adsorption and aggregation of insulin at a poly(acrylic acid) brush. *Phys. Chem. Chem. Phys.* **2010**, *12*, 4375-4382.
- 8) Das, S.; Tsouris, C.; Zhang, C.; Kim, J.; Brown, S.; Oyola, Y.; Janke, C.J.; Mayes, R.T.; Kuo, L.-J.; Wood, J.R.; Gill, G.A.; Dai, S. Enhancing Uranium Uptake by Amidoxime Adsorbent in Seawater: An Investigation for Optimum Alkaline Conditioning Parameters. *Ind. Eng. Chem. Res.* **2015**, *55*, 4294-4302.
- 9) Pan, H.-B.; Kuo, L.-J.; Wood, J.R.; Strivens, J.; Gill, G.A.; Janke, C.J.; Wai, C. Towards understanding KOH conditioning of amidoxime-based polymer adsorbents for sequestering uranium from seawater, *Royal Society of Chemistry* **2015**, *5*, 100715-100721.
- 10) Murdoch, T.; Humphreys, B.; Willott, J.; Prescott, S.; Nelson, A.; Webber, G.; Wanless, E. Enhanced specific ion effects in ethylene glycol-based thermoresponsive polymer brushes. *J. Col. Int. Sci.* **2016**, *490*, 869-878.
- 11) Chang, C.-J.; Reddy, M.; Hsieh, S.-R.; Huang, H.-C. Influence of imidazolium based green solvents on volume phase transition temperature of crosslinked poly(N-isopropylacrylamide-co-acrylic acid) hydrogel. *Soft Matter* **2015**, *11*, 785-792.
- 12) Chen, Q.; Xu, Y.; Cao, X.; Qin, L.; An, A. Core cross-linked star (CCS) polymers with temperature and salt dual responsiveness: synthesis, formation of high internal phase emulsions (HIPEs) and triggered demulsification. *Poly. Chem.* **2014**, *5*, 175-185.
- 13) Perry, S.; Li, Y.; Priftis, D.; Leon, L.; Tirrell, M. The Effect of Salt on the Complex Coacervation of Vinyl Polyelectrolytes. *Polymers* **2014**, *6*, 1756-1772.
- 14) Ladshaw, A.P.; Ivanov, A.S.; Das, S.; Bryantsev, V.; Tsouris, C.; Yiacoymi, S. First-Principles Integrated Adsorption Modeling for Selective Capture of Uranium from Seawater by Polyamidoxime Sorbent Materials. *Appl. Mater. Interfaces* **2018**, *10*, 12580-12593.

2.7 Nomenclature

PAO – Polyamidoxime

PAA – Poly-acrylic acid

d-PAO – Deuterated Polyamidoxime

PAO-co-PAA – Random copolymer of amidoxime and acrylic acid

ATRP – Atom Transfer Radical Polymerization

DMSO – Dimethyl sulfoxide

DMF – Dimethylformamide

Q – Momentum transfer

θ – Neutron beam incident angle

λ – Neutron beam wavelength

χ^2_v – Reduced Chi Squared

D₂O – Heavy Water

NaHCO₃ – Sodium Bicarbonate

NaCl – Sodium Chloride

SLD – Scattering Length Density

pD – Deuterium equivalent to pH

CHAPTER 3: Impact of Metal Ion Competition

3.1 Introduction

One of the primary challenges to the recovery of uranium (U) from seawater is the low concentration of U in seawater. A ready supply of saline solution with a higher concentration of U could be used as a seawater alternative allowing for greater U recovery with the adsorbents that are currently available. Brine reject from desalination plants, essentially a concentrate of seawater, could be used if the concentration of U scales with salinity. Furthermore, by incorporating amidoxime recovery systems into existing infrastructure the mooring cost, which are among the most significant costs of these systems, may be substantially reduced.¹ Biofouling, a significant risk in unfiltered seawater which can reduce adsorbent uptake by up to 30%, would also be mitigated or avoided entirely by utilizing the desalination plant's existing filtration systems.² The sale of U and other minerals recovered from the brine solution may also partially offset the cost of desalination. Therefore, the objective of this study is to evaluate the capacity of amidoxime adsorbents for the recovery of U from desalination brine-reject. Batch adsorption experiments in both feed seawater and brine reject solution are performed with adsorbents developed at Oak Ridge National Laboratory (ORNL) from their AF1 series adsorbent. The AF1 series is prepared by grafting amidoxime itaconic acid (ITA) copolymer chains to the surface of a polyethylene backbone. Modeling based on these experiments was performed to evaluate the efficacy of our thermodynamic model to simulate the adsorption of competing ions.

3.2 Materials and Methods

3.2.1 Materials

The samples used in the adsorption experiments came from the Tampa Bay Desalination plant in Florida with seawater coming from the plant's feedstock and brine rejected from the reverse osmosis membranes. ORNL's AF1 series adsorbent was used for the experiments in this study.³ The adsorbent materials were prepared by grafting acrylonitrile, with ITA comonomers, onto high-surface-area hollow-gear polyethylene fibers using radiation induced graft polymerization. Polymer grafting was performed by placing irradiated polyethylene trunk fibers into flasks containing a dimethyl sulfoxide solution of acrylonitrile and ITA for a period of 18 hr at 64°C. Conversion of the nitrile groups to amidoxime was achieved through hydroxylamine mediated amidoximation. Fibers were treated with a water/methanol (50/50 by wt.) solution containing 10% by weight hydroxylamine hydrochloride for 72 hr at 80°C. Two amidoxime ligands, the open chain acetamidoxime (AO) and cyclic glutarimide-dioxime (IDO), are formed during amidoximation. After amidoximation, the adsorbent samples were conditioned with 0.44 M potassium hydroxide at 80°C for one hr. Additional details regarding the synthesis and preparation of the AF1 series adsorbent are given in the work of Das and coworkers.³

3.2.2 Experimental Setup

Adsorption experiments were performed over a 12-week period in five gallon plastic tanks containing either filtered seawater or brine-reject solution. Each tank was thoroughly washed with a water/ethanol solution and then rinsed with either brine or seawater before being filled with their respective solutions. This treatment was performed

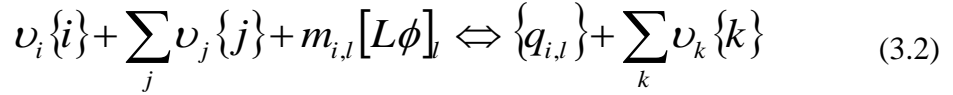
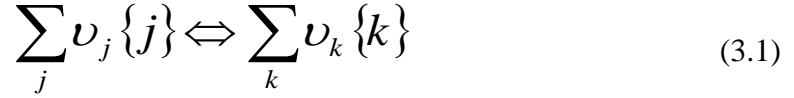
to suppress potential microbial growth.⁴ Visual inspections of the samples were conducted over the 12-week period to monitor for microbial development. The pH of both solutions was measured at the start of the experimental period for each solution yielding a pH of 7.7 for both the feed seawater and brine reject and did not change significantly during adsorption. Approximately 8.2 mg of adsorbent was added to each tank with the fibers suspended freely in solution. 10 mL aliquots were withdrawn from the tank periodically via pipette, over a 12-week period, along with an initial sample taken before addition of the adsorbent (see Appendix Tables A1 and A2). The tanks were kept at room temperature, about 23°C, and were shaken at a constant rate of 100 rpm over the 12-week duration of the experiment. Similar batch experiments in five gallon tanks with seawater were reported by Kim et al. (2013).⁵ Analysis of the 10 mL samples was conducted using inductively coupled plasma mass spectroscopy (Thermo Scientific's X-Series II), after acidification with high-purity (Optima grade) nitric acid from Fisher Scientific. A five-element internal standard (High Purity Standards ICP-MS-IS-2) of 100 ppb Bismuth (Bi), Indium (In), Scandium (Sc), Terbium (Tb), and Yttrium (Y) was used to correct for matrix effects. The liquid samples were aspirated using a Teflon SP nebulizer and Elemental Scientific PC3 spray chamber at a rate of 100 µL/min. These samples were quantified by comparing the average of six replicable measurements against a 6-point calibration curve to determine the concentration of U, zinc (Zn), copper (Cu), iron (Fe), and vanadium (V).^{4,6,7} After 12 weeks, the adsorbent fibers were digested in a concentrated solution of aqua regia, composed of concentrated hydrochloric and nitric acid at a ratio of 3:1. Acidic elution, as described by Gill and coworkers,⁴ would normally be used for adsorbate recovery to allow for the adsorbent material to be

recycled allowing for multiple deployments. Aqua regia is used in this study to ensure that all of the U is properly accounted for. The digested solution was then analyzed, in a similar manner to the 10 mL samples, yielding the adsorbed mass of the five elements listed previously, in addition to the adsorbed calcium (Ca) and magnesium (Mg). Experimental error in the results is due to error in analytical measurements, which was reported at ~5% by Gill et al. (2016).⁴

3.2.3 Modeling Methodology

Due to the intrinsic complexity of seawater, any model designed to adequately describe adsorption in seawater must not only consider reactions in the aqueous phase and on the adsorbent surface, but also the effects of various other mechanisms and parameters. This includes, but is not limited to, the effects of ionic strength, charging of the adsorbent surface, temperature, and pH. An object-oriented adsorption modeling software framework, where each object is used to represent various aspects of the problem's chemistry and physics which are combined into a single residual function and solved iteratively, was developed.⁸⁻¹⁰ Aqueous equilibrium and site-specific chemisorption reactions represent a significant proportion of the model and are represented by Equations 3.1 and 3.2 respectively. Where the stoichiometry (ν) and activity, denoted by curly brackets, are defined for the specific adsorbate (i) and each of the aqueous phase species (j and k). The ligand is denoted by the l subscript which is associated with the number of sites used by the adsorbate/ligand pair ($m_{i,l}$), molar concentration of active sites $[L\phi]_l$, and the chemisorption activity of the adsorbed species $\{q_{i,l}\}$. A list of complexation and aqueous phase reactions introduced to the model for this

study is given in Appendix A (Tables A3 and A4) and is built upon the aqueous and surface speciation that was previously considered in the works of Ladshaw and coworkers.⁸⁻¹⁰



Surface activity and surface charging are also key model components as both parameters affect the chemisorption equilibrium (Equation 3.3) through the surface activity parameter ($\gamma_{i,l}^s$) and Boltzmann factor ($\eta_{i,l}$), respectively. Adsorbent surface charging occurs as a result of both the binding of ligands with aqueous species^{11,12} and the protonation/deprotonation¹⁰ of the ligand and its comonomers. The Boltzmann factor (Equation 3.4) is further defined as a function of the temperature (T), Boltzmann constant (k_B), elementary electrical charge constant (e), net charge exchange (N), and the electrical surface potential (ψ). Non-idealities brought about by non-bonding interactions between chemical species on the adsorbent surface are included in the model through surface activity. Of the various methods for estimating surface activity, the universal quasi-chemical (UNIQUAC) model developed by Abrams and Prausnitz¹³ was used in this work.

$$K_{i,l} \cdot \eta_{i,l} = \frac{(\gamma_{i,l}^s q_{i,l}) \cdot \prod \{k\}^{\nu_k}}{[L\phi]_l^{m_{i,l}} \cdot \{i\}^{\nu_i} \cdot \prod \{j\}^{\nu_j}} \quad (3.3)$$

$$\eta_{i,l} = \exp\left(-\frac{N_{i,l} e \psi}{k_B T}\right) \quad (3.4)$$

3.3 Results and Discussion

3.3.1 Analysis of Feed Seawater

After a period of 12 weeks in batch, the adsorbent was collected, digested, and the digested solution examined by the analytical method described above. These results, along with the model results and the initial aqueous concentrations of V, Fe, Cu, Zn, U, Mg, and Ca, for feed seawater are summarized in Table 3.1. The two most plentiful adsorbed species are Ca and Mg. This is not unexpected given that the concentration of both Ca and Mg is several orders of magnitude larger than any of the other elements. Of the remaining adsorbed elements, U is the most significant, by mass, with a capacity of 6.22 mg/g adsorbent after 12 weeks (84 days) of adsorption. In terms of molar adsorption, however, U is much less significant with comparable adsorption to Fe, V, and Zn whilst being significantly lower than Cu.

Table 3.1. Experimental and predicted adsorption results (mg/g and mmol/kg adsorbent) after 12 weeks in batch and the initial aqueous concentrations ($\mu\text{g/L}$ and nM) determined from 10 mL aliquots of feed seawater. The analytical error is approximately 5%, as reported by Gill et al. (2016).⁴

Element	Aqueous Concentration		Adsorbed Mass			
	$\mu\text{g/L}$	nM	Experimental		Predicted	
	$\mu\text{g/L}$	nM	mg/g	mmol/kg	mg/g	mmol/kg
V	0.522	10.2	1.05	20.6	1.09	21.4
Fe	1.98	35.4	1.06	18.9	1.07	19.2
Cu	5.28	82.5	5.29	82.7	5.40	84.3
Zn	4.80	73.8	1.97	30.3	N/A	N/A
U	2.90	12.2	6.22	26.1	6.12	25.7
Ca	0.422 g/L	10.6 mM	16.6	415	16.3	407
Mg	1.32 g/L	54.8 mM	11.3	471	11.1	464

Adsorbed U species at the end of the exposure period account for about 93% of all U present in the batch solution. Earlier adsorption experiments with the AF1 series yielded adsorption capacities of about 3.5 mg/g adsorbent² while more recent experiments with the ORNL AF1FR2 adsorbent, which is similar to the AF1FR3 adsorbent used in this study, obtained 5.0 mg/g adsorbent⁴ over a 56 day exposure period. The difference between the AF1FR2 results and those obtained from this study are a consequence of the additional exposure time. For the remaining trace metals, the adsorbed mass is 5.29 mg Cu, 1.97 mg Zn, 1.06 mg Fe, and 1.05 mg V per g adsorbent. These represent values of 43%, 18%, 23%, and 87% of the total mass in the batch for Cu, Zn, Fe, and V, respectively.

Fe adsorption is surprisingly low given that previous experimental works had indicated that the adsorption of Fe was more favorable than that of U. Specifically, the results of Sun and coworkers¹⁴ and Parker and coworkers¹⁵ had shown that Fe-IDO complexes were stronger than their U-IDO counterparts and that the kinetics of Fe adsorption was comparable to the kinetics of U adsorption on IDO. There are a few factors that may explain this lower-than-expected adsorption. Fe in seawater can broadly be divided into four categories: Fe (II), inorganic labile Fe (III), labile organically complexed Fe (III), and inert Fe (III).¹⁶ Fe (II) is unstable in seawater and will oxidize rapidly in oxygenated water.^{17,18} Thus, Fe (II) is assumed to comprise a negligible component of the Fe in solution in this study. The proportion of Fe in the form of inorganic labile Fe (III), which can easily form complexes with amidoxime, and organically complexed Fe (III), where the adsorbents must compete with organic ligands to form Fe complexes, will determine the quantity of available Fe for adsorption.

Therefore, depending on the significance of the inert Fe fraction, the actual concentration of Fe that can readily form complexes with IDO may be significantly lower than the 1.98 $\mu\text{g/L}$ that was measured. Additionally, if the inorganic labile fraction only represents a small component of available Fe, then the IDO ligands might have to compete with the organic ligands to form Fe complexes. If both the inert fraction was high and the labile fraction was low, then adsorption of Fe could be substantially reduced which may explain the lower-than-expected adsorption observed.

For Ca and Mg adsorption, the discrepancy between experimental and modeling results is less than 5% for both elements. This agreement was obtained by reducing the log of the stability constant for the MgH_2IDO^+ complexation reaction by 0.35 and increasing for the CaH_2IDO^+ reaction by 0.1 relative to the values reported by Leggett and Rao.¹⁹ These two species each represent nearly 100% of adsorbed Ca and Mg, respectively. The adsorption of these two species is, furthermore, predominantly driven by the buildup of excess negative charge on the adsorbent surface. The ITA comonomer is the primary cause of this negative charging with a majority existing as either ITA^{2-} or HITA^- species, which represent 56.5% and 43% of total ITA respectively. As a comparison, both adsorbent ligands are largely neutral species, 66.2% of IDO as H_3IDO and 56% of AO as HAO, or protonated species, ~44% of AO as H_2AO^+ , with the remainder as complexes at seawater pH.

At lower pHs (Figure 3.1), the adsorption of Ca and Mg is significantly reduced with both elements dropping to a predicted adsorption capacity of less than 1.0 mg/g adsorbent by a pH of about 6.8. As the pH drops, the proportion of ITA as HITA^- and AO as H_2AO^+ increases leading to a substantial reduction in negative charging on the

adsorbent surface. The converse is also true for higher pH where the adsorption of Ca and Mg increases noticeably due to a reduced presence of H_2AO^+ and a greater proportion of ITA in the deprotonated form ITA^{2-} . The aqueous speciation of both Ca and Mg remains relatively constant over the pH range depicted in Figure 3.1, thus there is a clear correlation between the predicted adsorption and surface charging. There is, however, a degree of uncertainty with respect to the behavior ITA in seawater given the high probability of non-binding charge neutralizing interactions between aqueous ions and charged surface species. For instance, in an earlier modeling study on U/V selectivity, V adsorption on these same materials (ORNL AF1 fibers) could only be adequately described by introducing a counter-ion binding mechanism involving sodium ions.¹⁰ A similar interaction between an aqueous cation and either ITA^{2-} or HITA^- would reduce the favorability of Ca and Mg adsorption by neutralizing some of the excess negative charge on the adsorbent surface.

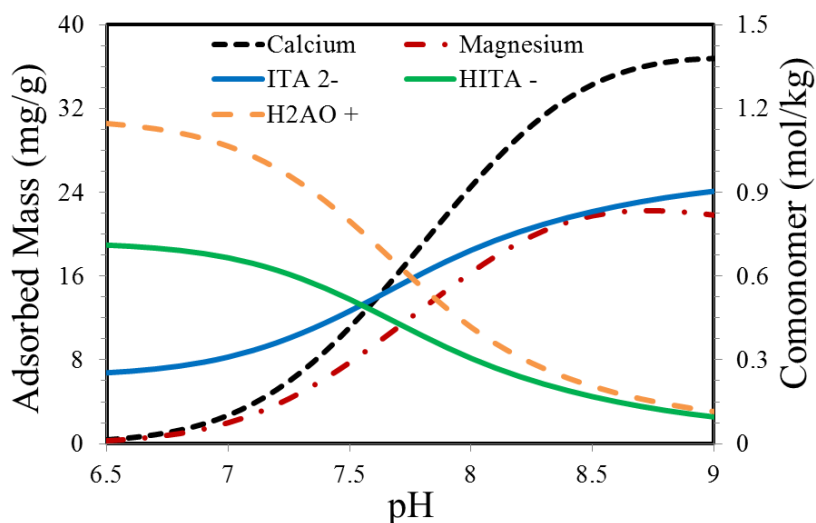


Figure 3.1. Adsorption of Ca and Mg (mg/g adsorbent) and adsorbent surface speciation of ITA^{2-} , HITA^- , and H_2AO^+ (mol/kg adsorbent) predicted for pH 6.5 – 9.0.

In the case of Cu adsorption, the aqueous phase concentration of Cu^{2+} ions was adjusted to obtain the agreement observed between the experimental and modeling results. This was done in an effort to account for the presence of competing organic ligands in seawater, whose characteristics are unknown. Organic ligands dominate the aqueous speciation of Cu in seawater with upwards of 99.99% in the form of organically complexed species, reducing the free Cu ion concentration to be on the order of 10^{-4} nM.²⁰⁻²² Based on this information, it is not unreasonable to assume that steady state aqueous concentration of free ions is $\sim 1.7 \times 10^{-4}$ nM. At this concentration, the discrepancy between experimental and modeling results is 2%.

For Fe modeling, it was assumed that adsorption would be limited by the factors previously discussed. The difference between the experimental data and modeling results was 1.2%. This was obtained by reducing the concentration of Fe (III) available for adsorption to 8.3 nM of which essentially 100% is adsorbed. This was done to account for the unknown inert fraction of Fe which is unavailable for adsorption and unknown organically complexed fraction that will compete with IDO for available Fe. There is good agreement between experimental and modeling results for U and V with a discrepancy of 1.6% and 3.9% for each element, respectively. This is to be expected given that the adsorption of both U and V is well understood and has been examined extensively in previous works.^{4,8-10} Adsorption of Zn was not considered because no complexation information is available for Zn adsorption onto either the IDO or the AO ligands. Additionally, complexation information was also unavailable for adsorption of Ca, Mg, Fe, and Cu onto AO ligands and, as such, these complexes were not considered.

3.3.2 Analysis of Desalination Brine Reject

The most significant differences observed between adsorption experiments in feed seawater and brine reject (Table 3.2) was in the adsorption of U, V, and Fe. Despite having more than twice as much U in solution, the U adsorption in the brine reject was approximately 36% lower than in seawater dropping from 6.22 mg/g in seawater to 3.95 mg/g in the reject solution. In terms of molar adsorption, U has the lowest surface concentration of all five trace metals with only 16.6 moles of U adsorbed per kg adsorbent. Additionally, the kinetics of adsorption in the brine solution is far slower with less U adsorbed at each sampling time (Figure 3.2). This is caused by significantly higher competition for adsorption sites from V and Fe which are known, based on previous investigations, to form more favorable complexes with IDO than IDO does with U.^{10,14,23}

Table 3.2. Experimental and predicted adsorption results (mg/g adsorbent) after 12 weeks and the initial aqueous concentration ($\mu\text{g/L}$) determined from 10 mL sample of brine reject. The analytical error is approximately 5%, as reported by Gill et al. (2016).⁴

Element	Aqueous Concentration		Adsorbed Mass			
	$\mu\text{g/L}$	nM	mg/g	mmol/kg	mg/g	mmol/kg
V	1.37	26.9	2.67	52.4	2.79	54.7
Fe	54.4	971	3.00	53.6	3.02	53.9
Cu	4.74	74.1	5.87	91.7	5.87	91.7
Zn	7.51	116	1.43	22.0	N/A	N/A
U	6.66	28.0	3.95	16.6	6.05	25.4
Ca	0.77 g/L	19.3 mM	15.4	383	21.1	527
Mg	2.43 g/L	101.0 mM	13.3	554	14.4	599

A mass of 1.2 tonnes of U can fuel a 5-MW nuclear reactor.¹ Assuming that the adsorbent can be deployed 10 times with a 5% loss of capacity after each deployment, this mass of U could be recovered annually with an adsorbent mass of 33 tonnes in

seawater and 60 tonnes in brine. This estimate is based on the 36 day U uptake capacity (Figure 3.2) of 4.22 mg U/g adsorbent and 2.59 mg U/g adsorbent in feed seawater and brine reject, respectively. On a global scale, this could yield ~22,100 tonnes of U annually, which would fuel roughly 92 1-GW reactors, from the slightly more than 18,400 desalination plants operated around the globe. Additionally, this estimate of U mass recovered is probably fairly low given that many desalination plants would likely be able to scale up their U recovery. For the Tampa Bay plant, a recovery rate of 1.2 tonnes U per year would only represent 0.68% of all U passing through the plant. Thus, a far higher recovery rate is theoretically possible though this would be dependent upon the mass of adsorbent that was used in the recovery system.

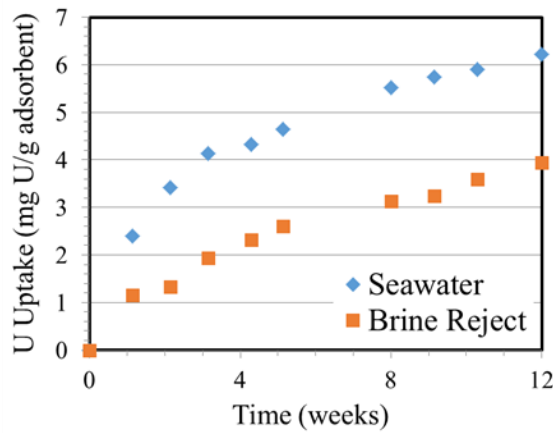


Figure 3.2. U uptake (mg U/g adsorbent) over time (weeks) for AF1 adsorbent in feed seawater and brine reject solution. Error is approximately 5%, as reported by Gill et al. (2016).⁴

The concentration of Fe is significantly higher in the brine reject solution, 27 times higher than in seawater, because ferric hydroxide [Fe(OH)₃] is used as a coagulant in the desalination plant's pretreatment process. As a result, the quantity of Fe available for

adsorption increases substantially leading to a threefold increase in the adsorbed mass of Fe from 1.06 mg/g adsorbent to 3.00 mg/g adsorbent. The initial V concentration is about 2.5 times higher in the reject solution and is mirrored in the quantity of V adsorbed, 2.67 mg/g adsorbent, which is also about 2.5 times higher than the adsorption in seawater. For the remaining minerals, the difference between adsorption in the reject solution and in seawater is not as significant.

Aside from $\text{Fe}(\text{OH})_3$, other coagulation agents such as ferric chloride (FeCl_3) and ferrous sulfate (FeSO_4) can be used though it is unlikely that they will significantly affect the material's adsorption behavior. Given the high concentrations of sulfate (2.8 g/L) and chloride (19.8 g/L) already present in seawater, the change in concentration at the expected coagulation dosage is likely to be relatively small. As such, the pH and ionic strength, and by extension the activity coefficients of the aqueous ions, of the brine solution formed when using these alternative coagulants will be comparable to their current values. Furthermore, the speciation of many of the competing metals is largely independent of both chloride and sulfate concentrations. For this study, the aqueous speciation of $\text{U}^{8,24}$ and V^8 are dependent upon carbonate speciation, Ca and Mg exist predominantly as free ions, and Cu^{20-22} and Fe^{16} are dominated by organic complexes. Thus, it is not expected that the addition of chloride or sulfate from coagulants can significantly impact U uptake.

In the brine reject solution, there was good agreement between modeling and experimental results for V, Fe, Cu, and Mg. The free Cu ion concentration was reduced slightly to a value of 1.5×10^{-4} nM for the brine reject simulation from the 1.7×10^{-4} nM value used in seawater. For modeling of Fe adsorption, the available Fe concentration

was increased from 8.3 nM to 23.4 nM yielding good agreement with the experimental results. As discussed previously, only the Fe in the labile and organically complexed phases would be readily available for adsorption. Aside from the Fe adsorbed by aqueous organic ligands that have not been fully saturated with Fe,²⁵ a large proportion of the added Fe will likely form inert complexes in the brine solution, significantly reducing the total Fe which is actually available for adsorption.

There were no additional considerations made for the adsorption of Ca, Mg, V, or U in modeling adsorption from brine reject. This method achieved good agreement for V and Mg, though U and Ca are overestimated. For Ca adsorption, the discrepancy observed is likely tied to the charge neutralization interactions discussed previously. Despite having more than twice as much aqueous U, the modeled adsorbed mass of U in the brine solution is roughly the same as in seawater. This is the result of increased competition with the other adsorbing elements, particularly Fe and V. The discrepancy between experimental and modeling results for U adsorption is likely explained, at least in part, by the adsorption of other competing elements, such as Zn, which could not be considered in the model. Additionally, the modeling framework used in this study solves the system at equilibrium, which may not have been reached in the brine as a result of the slowed U uptake kinetics (Figure 3.2). Thus, if the experimental exposure time was extended then the adsorbed mass of U in brine may eventually reach a value comparable to adsorption in seawater. This additional exposure time would still be a significant disadvantage given that higher capacity with low exposure times is desired.

It is also possible that the number of available adsorption sites is lower than anticipated. Aqueous kosmotropic ions, such as Ca^{2+} , Mg^{2+} , Na^+ , and sulfate, in addition

to the formation of multi-ligand amidoxime complexes are known to affect the graft chain conformation of our amidoxime materials.²⁶ The conformation is influenced by the formation of inter-polymer and intra-polymer bonds known as crosslinking. These crosslinks cause the amidoxime chains grafted to the surface of the polyethylene fiber to become intertwined making diffusion more difficult and reducing accessibility to adsorption sites. A reduction in the number of available adsorption sites would most likely lead to a reduction in U adsorption due to unfavorable competition with V and Fe. Model predictions show that the adsorption of U (Figure 3.3) is more susceptible to changes in the availability of IDO ligands in brine reject solution than seawater. At the experimental pH, a 9% reduction in the total IDO results in a roughly 2% decline in U adsorption in seawater, whilst in brine, this reduction yields a 13.7% drop in U adsorption. Furthermore, a 45% reduction in total IDO reduces adsorption of U by 19.2% and 67.3% in seawater and brine, respectively.

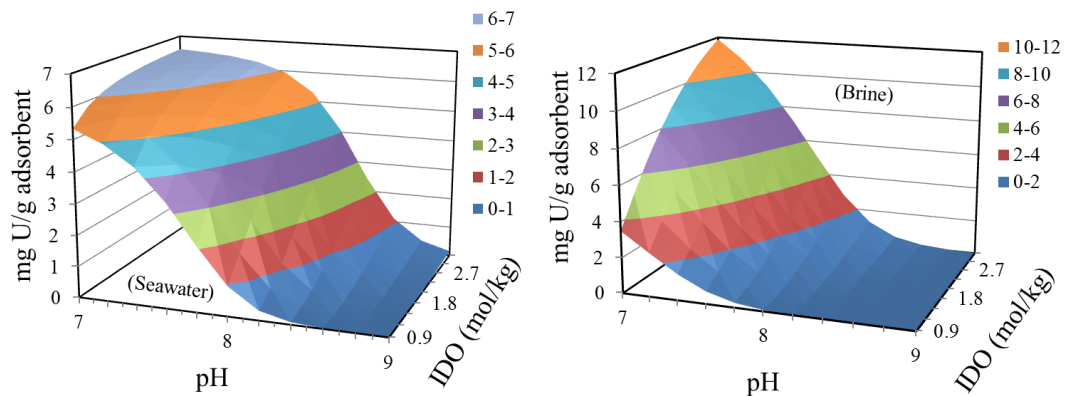


Figure 3.3. Predicted effects of total IDO and pH on adsorption of U in (a) feed seawater and (b) brine reject solution.

For the remaining elements, the discrepancy between their behavior in seawater and brine is much less significant. V adsorption (Figure 3.4), by comparison, drops by 2.2% and 3% for seawater and brine, respectively, when IDO is reduced by 9% at the experimental pH. Additionally, a 45% reduction in total IDO leads to a 21.8% and 31.1% decline in V adsorption in seawater and brine, respectively. The susceptibility of Ca and Mg adsorption to total IDO is similar to V. Thus, a relatively small reduction in available IDO could explain the lower U adsorption in brine without significantly affecting the other competing elements. A reduction of this nature would also be more significant in brine due to the higher aqueous concentration of kosmotropes in that solution.

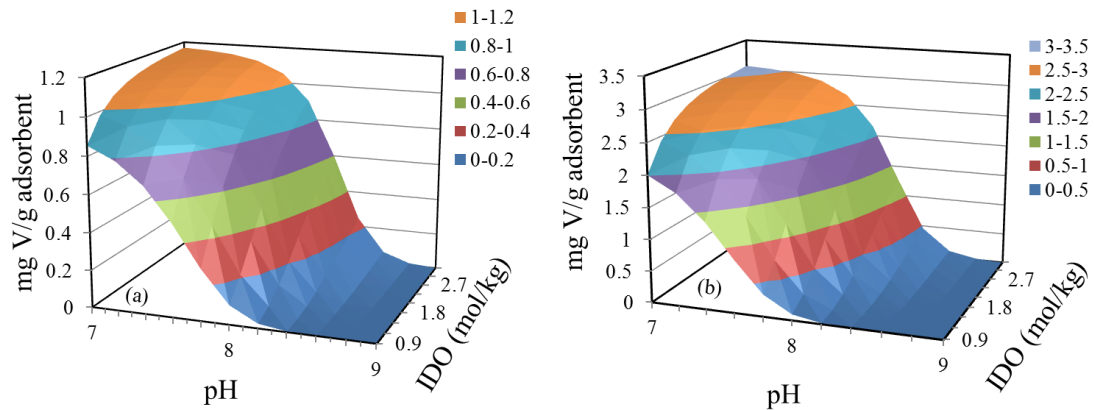


Figure 3.4. Predicted effects of total IDO and pH on adsorption of V in (a) feed seawater and (b) brine reject solution.

3.4 Conclusions

The study of U extraction from seawater has been an area of interest for more than six decades covering a wide range of materials of which amidoxime is considered to be the most promising. One of the most significant obstacles to a recovery of U has been its low concentration in seawater. Brine reject solution from desalination plants is a

concentrate of seawater and could allow for greater adsorption capacities to be achieved with existing adsorbents. In addition, brine reject can also be used to reduce the adsorbent deployment costs by incorporating the adsorbent system into existing infrastructure, eliminate the possibility of biofouling by taking advantage of the desalination plant's filtration systems, and potentially allow for the recovery of other valuable minerals such as lithium, Mg, and V. Two batch adsorption experiments were performed using ORNL's AF1 series adsorbent in five gallon tanks of feed seawater and brine reject from the Tampa Bay Desalination Plant in Florida. The most significant differences observed between these experiments were in the adsorption of U, V, Fe. As a result of the ferric hydroxide used in the pretreatment process, the quantity of dissolved Fe in the reject solution was 27 times higher than in the feed seawater. This led to an increase in the quantity of adsorbed Fe from 1.06 mg/g adsorbent in seawater to 3.00 mg/g adsorbent in the reject solution. An increase of about 150% to the dissolved V concentration in the reject solution caused a comparable increase in the adsorbed V. The changes in adsorption of Cu and Zn between feed and reject seawater were comparatively small, while they were insignificant for Ca and Mg. Thus, the 36% decline in adsorbed U from 6.22 mg/g adsorbent to 3.95 mg/g adsorbent can be attributed primarily to an increase in competition from Fe and V.

With respect to the modeling, there were a number of unknowns relating to charge neutralizing interactions and organic ligands, which affected the adsorption of Ca, Mg, Cu, and Fe. Several of these unknowns were accounted for by adjusting parameters in the model, such as free ion concentrations and binding constants, in order to yield good agreement in seawater for all elements and in brine for Fe, V, Cu, and Mg. However,

even with these adjustments, there are still several unknowns in the model which lead to uncertainty in the results and will need to be considered more thoroughly in future studies. Regardless of that uncertainty, the model was still able to demonstrate its capability to provide accurate results for U and V adsorption in real seawater and was instrumental as an analysis tool in exploring justifications for observed metal ion uptake in the seawater and in the brine-reject solutions. The results of this study demonstrate the need of more selective U adsorbents to take advantage of the higher U concentration offered by desalination brine reject solutions with respect to U recovery.

3.5 Acknowledgments

The development of this chapter was a collaborative effort among my co-authors and myself and was the main subject of the following manuscript: A. Wiechert, A. Ladshaw, G. Gill, J. Wood, S. Yiacoymi, C. Tsouris. Uranium Resource Recovery from Desalination Plant Feed and Reject Water using Amidoxime Functionalized Adsorbent. Published in the Industrial and Engineering Chemistry Research on November 27th 2018.

3.6 References

- 1) Flicker-Byers, M.E.; Haji, M.N.; Slocum, A.H.; Schneider, E. Cost Optimization of a Symbiotic System to Harvest Uranium from Seawater via an Offshore Wind Turbine. *Ocean Engineering*, **2018**, *169*, 227-241.
- 2) Park, J.; Gill, G.A.; Strivens, J.; Kuo, L.-J.; Jeters, R.; Avila, A.; Wood, J.; Schlafer, N.; Janke, C.; Miller, E.; Thomas, M.; Addleman, R.; Bonheyo, G. Effect of Biofouling on the Performance of Amidoxime-Based Polymeric Uranium Adsorbents. *Ind. Eng. Chem. Res.* **2016**, *55*, 4328-4338.
- 3) Das, S.; Oyola, Y.; Mayes, R.; Janke, C.; Kuo, L.-K.; Gill, G.; Wood, J.; Dai, S. Extracting Uranium from Seawater: Promising AF Series Adsorbents. *Ind. Eng. Chem. Res.* **2016**, *55*, 4110-4117.

- 4) Gill, G.; Kuo, L.-J.; Janke, C.; Park, J.; Jeters, R.; Bonheyo, G.; Pan, H.-B.; Wai, C.; Khangaonkar, T.; Bianucci, L.; Wood, J.; Warner, M.; Peterson, S.; Abrecht, D.; Mayers, R.; Tsouris, C.; Oyola, Y.; Strivens, J.; Schlafer, N.; Addleman, R.; Chouyyok, W.; Das, D.; Kim, J.; Buessler, K.; Breier, C.; D'Alessandro, E. The Uranium from Seawater Program at the Pacific Northwest National Laboratory: Overview of Marine Testing, Adsorbent Characterization, Adsorbent Durability, Adsorbent Toxicity, and Deployment Studies. *Ind. Eng. Chem. Res.* **2016**, *55*, 4264-4277.
- 5) Kim, J.; Oyola, Y.; Tsouris, C.; Cole, C.R.; Mayes, R.T.; Janke, J.C.; Dai, S. Characterization of Uranium Uptake Kinetics from Seawater in Batch and Flow-Through Experiments. *Ind. Eng. Chem. Res.* **2013**, *52*, 9433-9440.
- 6) Kim, J.; Tsouris, C.; Oyola, Y.; Janke, C.; Mayes, R.; Dai, S.; Gill, G.; Kuo, L.-J.; Wood, J.; Choe, K.-Y.; Schneider, E.; Linder, H. Uptake of Uranium from Seawater by Amidoxime-Based Polymeric Adsorbent: Field Experiments, Modeling, and Updated Economic Assessment. *Ind. Eng. Chem. Res.* **2014**, *53*, 6076-6083.
- 7) Wood, J.R.; Gill, G.A.; Kuo, L.-J. Strivens, J.E.; Choe, K.-Y. Comparison of Analytical Methods for the Determination of Uranium in Seawater Using Inductively Coupled Plasma Mass Spectrometry. *Ind. Eng. Chem. Res.* **2016**, *55*, 4344-4350.
- 8) Ladshaw, A.P.; Das, S.; Liao, W.-P.; Yiacoumi, S.; Janke, C.; Mayes, R.; Dai, S.; Tsouris, C. Experiments and Modeling of Uranium Uptake by Amidoxime-Based Adsorbent in the Presence of Other Ions in Simulated Seawater. *Ind. Eng. Chem. Res.* **2016**, *55*, 4241-4248.
- 9) Ladshaw, A.P.; Wiechert, A.I.; Das, S.; Yiacoumi, S.; Tsouris, C. Amidoxime Polymers for Uranium Adsorption: Influence of Comonomers and Temperature. *Materials*. **2017**, *10*, 1268.
- 10) Ladshaw, A.P.; Ivanov, A.S.; Das, S.; Bryantsev, V.; Tsouris, C.; Yiacoumi, S. First-Principles Integrated Adsorption Modeling for Selective Capture of Uranium from Seawater by Polyamidoxime Sorbent Materials. *Appl. Mater. Interfaces*. **2018**, *10*, 12580-12593.
- 11) Yiacoumi, S.; Tien, C. *Kinetics of Metal Ion Adsorption from Aqueous Solutions*; Kluwer Academic Publishers: Boston, MA, 1995.
- 12) Kalinin, V.V.; Radke, C. J. An ion-binding model for ionic surfactant adsorption at aqueous-fluid interfaces. *Colloids Surf.* **1996**, *114*, 337-350.

- 13) Abrams, D. S.; Prausnitz, J. M. Statistical thermodynamics of liquid mixtures: A new expression for the excess Gibbs energy of partly or completely miscible systems. *AIChE J.* **1975**, *21*, 116–128.
- 14) Sun, X.; Xu, C.; Tian, G.; Rao, L. Complexation of glutarimidedioxime with Fe(III), Cu(II), Pb(II), and Ni(II), the competing ions for the sequestration of U(VI) from seawater. *Dalton Trans.* **2013**, *42*, 14621-14627.
- 15) Parker, B.F.; Hohloch, S.; Pankhurst, J.R.; Zhang, Z.; Love, J.B.; Arnold, J.; Rao, L. Interactions of vanadium(IV) with amidoxime ligands: redox reactivity. *Dalton Trans.* **2018**, *47*, 5695-5702.
- 16) Gledhill, M.; Buck, K.N.; The organic complexation of iron in the marine environment: a review. *Frontiers in Microbiology.* **2012**.
- 17) Rose, A.L.; Waite, T.D. Kinetic Model for Fe(II) Oxidation in Seawater in the Absence and Presence of Natural Organic Matter. *Environ. Sci. Technol.* **2002**, *36*, 433-444.
- 18) Achterberg, E.P.; Holland, T.W.; Bowie, A.R.; Mantoura, R.F.C.; Worsfold, P.J. Determination of iron in seawater. *Analyt. Chim. Acta.* **2001**, *442*, 1-14.
- 19) Leggett, C.J.; Rao, L. Complexation of calcium and magnesium with glutarimidedioxime: Implications for the extraction of uranium from seawater. *Polyhedron.* **2015**, *95*, 54-59.
- 20) Buck, K.N.; Bruland, K.W. Copper speciation in San Francisco Bay: A novel approach using multiple analytical windows. *Marine Chem.* **2005**, *96*, 185-198.
- 21) Bruland, K. W.; Rue, E.L.; Donat, J.R.; Skrabal, S.A.; Moffett, J.W. Intercomparison of voltammetric techniques to determine the chemical speciation of dissolved copper in a coastal seawater sample. *Analyt. Chim. Acta.* **2000**, *405*, 99-113.
- 22) Tang, D.; Warnken, K.W.; Santschi, P.H. Organic complexation of copper in surface waters of Galveston Bay. *Limnol. Oceanogr.* **2001**, *46*, 321-330.
- 23) Wang, C.-Z.; Wu, Q.-Y.; Lan, J.-H.; Chai, Z.-F.; Wu, G.-Z.; Shi, W.-Q. Complexation of vanadium with amidoxime and carboxyl groups: uncovering the competitive role of vanadium in uranium extraction from seawater. *Radiochim. Acta* **2017**, *105*, 541-553.
- 24) Endrizzi, F.; Leggett, S.; Rao, L. Scientific Basis for Efficient Extraction of Uranium from Seawater. 1: Understanding the Chemical Speciation of Uranium under Seawater Conditions. *Ind. Eng. Chem. Res.* **2016**, *55*, 4249-4256.

- 25) Thuroczy, C.E.; Gerringa, L.J.A.; Klunder, M.B.; Middag, R.; Lann, P.; Timmermans, K.R.; de Baar, H.J.W. Speciation of Fe in the Eastern North Atlantic Ocean. *Deep-Sea Res.* **2010**, *57*, 1444-1453.
- 26) Wiechert, A.I.; Liao, W.-P.; Hong, E.; Halbert, C.E.; Yiacoumi, S.; Saito, T.; Tsouris, C. Influence of hydrophilic groups and metal-ion adsorption on polymer-chain conformation of amidoxime-based uranium adsorbents. *Journal of Colloid and Interface Science.* **2018**, *524*, 399-408.

3.7 Nomenclature

ITA – Itaconic Acid

AO – Acetamidoxime

IDO – Glutarimide-dioxime

UNIQUAC – Universal quasi-chemical model

Fe(OH)₃ – Ferric hydroxide

FeCl₃ – Ferric Chloride

FeSO₄ – Ferrous Sulfate

Bi – Bismuth

In – Indium

Sc – Scandium

Tb – Terbium

Y – Yttrium

ν – Stoichiometric constant

γ^s – Surface activity parameter

η – Boltzmann factor

ψ - Electrical surface potential

e – Elementary electrical charge constant

N – Net Charge exchange

T – Temperature

k_B – Boltzmann constant

$\{i\}$ – Aqueous activity of a species

$\{q\}$ - Chemisorption activity of an adsorbed species

m – Number of sites used in an adsorption reaction

$[L\phi]$ – Molar concentration of active sites

i, j, k – Indices for aqueous species

l – Index for ligands

CHAPTER 4: Alternative Adsorbent Synthesis

4.1 Introduction

The two most significant contributors to the cost of uranium (U) recovery from seawater are adsorbent synthesis and the chemicals used in alkaline treatment for conditioning and regeneration of the adsorbent.¹ The Oak Ridge National Laboratory (ORNL) adsorbents previously discussed are synthesized using radiation induced graft polymerization to attach amidoxime polymers to a polyethylene backbone and undergo alkaline treatment with potassium hydroxide.^{2,3} This technique is highly controllable allowing for precise tuning of adsorbent synthesis, however, its complexity is a major contributor to synthesis costs. Lower cost chemicals for alkaline treatment, such as sodium hydroxide (NaOH), have been considered and can reduce U recovery costs by up to 30% when used in place of potassium hydroxide.¹ The acrylic fiber based amidoxime adsorbent, termed the LCW adsorbent, considered in this study is intended to substantially reduce both the cost of alkaline treatment and that of adsorbent synthesis, while also increasing the durability of the adsorbent. This is achieved through simplified adsorbent synthesis based on the amidoximation of commercially available acrylic fibers and the use of NaOH for alkaline treatment. The performance of these LCW adsorbents has not yet been examined extensively, thus the goal of this study is to assess the viability of these adsorbents for U recovery from seawater. Adsorption experiments were performed with ambient seawater at a temperature of $10.8 \pm 0.7^\circ\text{C}$ using braided LCW materials in a meso-scale raceway system (total volume of 0.9 m^3) to more realistically reflect deployment conditions. Kinetic adsorption modeling is also performed to predict

the adsorption loadings for relatively long-term seawater deployment (56 days) at temperatures up to 31°C. These performance simulations are then compared to ORNL's AF1² and AI8³ adsorbents synthesized using radiation induced graft polymerization with itaconic and vinylphosphonic acid comonomers, respectively.

4.2 Methodology

4.2.1 Experimental Methodology

Adsorption experiments were conducted over a 28-day period using ambient seawater with an average temperature of ~10.8°C in the meso-scale raceway system (MicroBio Engineering Inc, San Luis Obispo, CA, USA) shown in Figure 4.1. The system has a total volume of 0.9 m³ and a recirculation rate in the raceway of 8.0 cm/s. The influent flow rate of fresh seawater entering the raceway was controlled to 3.6 m³/hr. Ambient seawater was drawn by pump from Sequim Bay, WA, at a depth of ~10 m through a plastic pipe. Raw seawater was roughly filtered by an Arkal Spin KlinTM filter system (nominal pore size 40 µm) to remove large particles. The seawater pH in the flume was monitored daily using a VWR Scientific portable pH probe equipped with a temperature compensating glass electrode that was calibrated using National Institute of Standards and Technology (NIST) traceable buffers. Salinity in the flume was also measured on a daily basis using an YSI model Pro30 instrument. Both salinity and pH remained relatively constant during the experimental period, with values of 30.5±0.3 psu and 8.07±0.03, respectively.

The braided LCW adsorbent was synthesized from textile grade acrylic fibers consisting of 92% acrylonitrile and 8% methyl acrylate by weight. Amidoximation of the

acrylonitrile monomers was carried out using a 3.0 w.t. % hydroxylamine solution made in a 1:1 by volume methanol-water mixture at 70°C for 45 min. After amidoximation, the fiber was conditioned using a 1.0 M NaOH solution at room temperature for 24 hr followed by a deionized water rinse. Additional details regarding adsorbent synthesis can be found in the work of Pan and coworkers.⁴

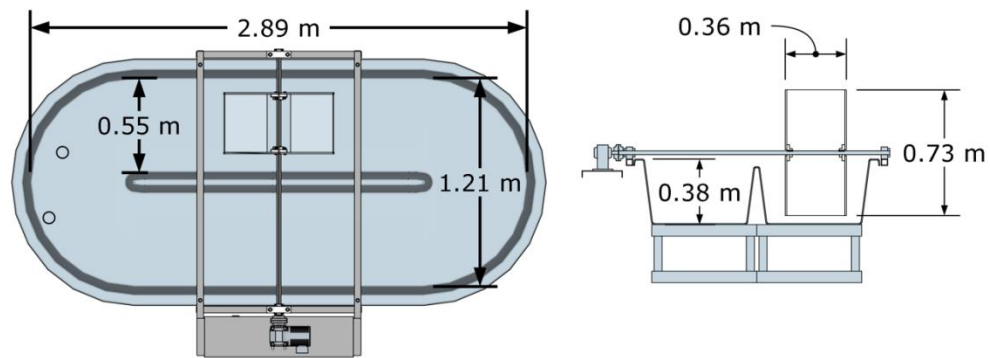


Figure 4.1. Schematic of recirculating flume system used in adsorption experiments (the schematic is a courtesy from the MicroBio Engineering Inc). This setup was operated at environmental conditions, at an average temperature of 10.8°C with 40-micron pre-filtered seawater, to more realistically simulate field deployment conditions.

Adsorbents were grouped by braid size with large braids (60 g per braid) in Cage C and small braids (10 g per braid) in all other cages (Figure 4.2). The total adsorbent mass was about 980 g with 800 g of small braids divided evenly between the eight cages containing small braids and 180 g of large braids in Cage C. Adsorbent snips were collected weekly from the tips of the adsorbent braids in Cages B and C using titanium-coated scissors and analyzed to determine the adsorbed mass of U and other metals. Snipped samples were first washed with DI water and then dried at 80°C using a heating block overnight.

Dried adsorbent snips were then digested in 15 mL of Fisher Scientific Optima grade 50% aqua regia acid solution consisting of a 3:1 hydrochloric-nitric acid mixture for three hr at 85°C. Analysis of the digestate was carried out using a PerkinElmer 7300 inductively coupled plasma optical emission spectrometer (ICP-OES) and quantified based on standard calibration curves. The aqueous concentrations of U and vanadium (V) were determined using inductively coupled plasma mass spectroscopy with the on-line pre-concentration method.⁵ This method was carried out using an Elemental Scientific seaFAST S2™ equipped with a seaFAST PFA chelation column packed with ethylenediaminetriacetic/iminodiacetic acid ion exchange resin. Analytes were eluted off the column using 10% nitric acid and then nebulized for analysis by a Thermo Scientific ICap Q inductively coupled plasma mass spectrometer (ICP-MS).

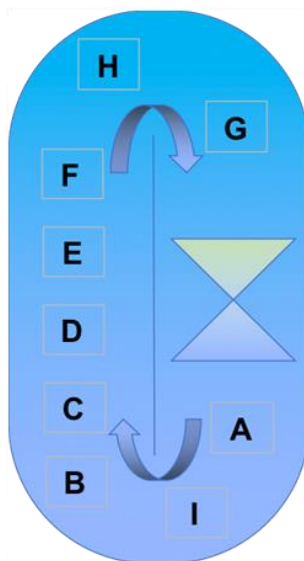


Figure 4.2. Schematic of the cages containing adsorbent braids in the raceway where Cage C contains three large braids (60 g per braid) and every other cage has 10 small braids (10 g per braid).

4.2.2 Modeling Methodology

The adsorption of U and other metals on amidoxime based fibers is primarily governed through adsorbent-adsorbate reaction kinetics and the mechanisms of mass transfer including inter-particle, inter-phase, and intra-particle mass transfer.⁶ At the experimental linear velocity of about 8.0 cm/s, however, the mass-transfer limitations in the flume are removed and as such do not need to be considered.⁷ To account for adsorption, all adsorbent-adsorbate reactions are assumed to proceed as reversible Langmuir type reactions (Equation 4.1) where C is the adsorbate concentration in the bulk phase, q is the adsorption capacity represented as mass adsorbed per mass of adsorbent, and L is the capacity still available for adsorption.

This available capacity L is in turn a function (Equation 4.2) of the theoretical maximum capacity (q_{\max}) and q . Equations 4.1 and 4.2 can be combined to derive a kinetic expression for adsorption (Equation 4.3) with forward and reverse reaction rate constants of k_f and k_r , respectively. For the bulk phase, the system is treated as a series of perfectly mixed reactors defined by Equation 4.4. In this equation V is the reactor volume, M_a is adsorbent mass, C_j is the concentration of the j^{th} element in the reactor, Q_i is the i^{th} incoming flowrate, C_{ij} is the i^{th} influent concentration of the j^{th} element, Q_o the o^{th} outgoing flow, and q_j is the adsorbent mass of the j^{th} element. A series of 10 perfectly mixed reactors, corresponding to the nine adsorbent cages shown in Figure 4.2 and the section of the raceway where concentration is monitored, is considered when modeling is performed. The forward and reverse reaction rates and maximum adsorption capacity are summarized in Table 4.1.



$$L = q_{\max} - q \quad (4.2)$$

$$\frac{\partial q}{\partial t} = k_f C q_{\max} - (k_f C + k_r) q \quad (4.3)$$

$$V \frac{\partial C_j}{\partial t} = \sum \mathcal{Q}_i C_{ij} - \sum \mathcal{Q}_o C_j - M_a \frac{\partial q_j}{\partial t} \quad (4.4)$$

Table 4.1. Forward (k_f) and reverse (k_r) reaction rate constants for U, V, and Zn and adsorbent max capacity (mol/kg adsorbent) for small and large braids.

		Small Braids	Large Braids
q_{\max} (mol/kg)		1.47	1.47
k_f (m ³ /mol/hr)	U	0.75	0.544
	V	2.75	2.0
	Zn	1.25	0.906
k_r (1/hr)	U	0.00107	0.00107
	V	0.00275	0.00275
	Zn	0.00625	0.00625

4.3 Results and Discussion

After an exposure period of 28 days, the salinity normalized U recovery rate for the small LCW braids in Cage B was 1.43 mg/g adsorbent while the large braids in Cage C had an U capacity of 1.17 mg/g adsorbent (Table 4.2). The disparity in U recovery between the small and large LCW braids can likely be attributed to complications arising from material scale-up. At first glance, these recovery rates may appear lower than the rates previously observed with similar adsorbent materials, such as LCW-MSL-10 which attained an U recovery rate of approximately 4.4 mg/g adsorbent over 28 days filtered seawater exposure.⁸ These experiments, however, were performed at an average temperature of 20°C, compared to the 10.8°C maintained on average for this study, and with finely filtered seawater (0.45-µm nominal pore size). The effect of temperature on U

uptake for LCW adsorbents has not been studied; however, temperature dependent adsorption in other amidoxime based materials developed at ORNL have been analyzed.^{9,10} In the case of ORNL’s AF1 series adsorbent using 0.45 μm filtered Sequim Bay seawater, the salinity normalized 21-day recovery rate for small braids dropped from 2.5 mg U/g adsorbent at 20°C to 0.93 mg U/g adsorbent at 8°C.¹⁰ This is a result of U adsorption on amidoxime-based adsorbents being highly endothermic (apparent enthalpy ~ 58 kJ/mol).^{9,10} Therefore, the reduced U adsorption capacity in the present study can be attributed to this temperature effect.

Table 4.2. Concentration in feed seawater and salinity normalized 28-day adsorption capacities on small braids in Cage B (LCW-B) and Cage C large braids (LCW-C) for U, V, Fe, Zn, and Cu.

	Concentration	LCW-B		LCW-C	
	nM	mg/g	$\mu\text{mol/g}$	mg/g	$\mu\text{mol/g}$
U	12.8	1.43	6.01	1.17	4.92
V	36.2	1.90	37.25	1.26	24.71
Fe	545.3	1.86	33.21	1.71	30.54
Zn	22.1	0.44	6.77	0.31	4.77
Cu	7.5	0.03	0.47	0.02	0.31

The filtration level may also affect adsorption through adsorbent biofouling. Coarse filters, such as the 40- μm pore size filter used in this study, allow microorganisms to infiltrate the system and colonize the adsorbent braids. This leads to a reduction in the materials adsorption capacity, though it also offers a more realistic idea of the adsorbent’s capacity when deployed in the open ocean. Capacity loss from biofouling can be as high as 30% under worst case conditions (i.e., fully exposed to light) at 20°C.¹¹ For the

experiments in the present study, it is highly unlikely that the adsorbents would experience worst case capacity losses since the raceway was covered leaving the braids in complete darkness for most of the experiment. This inhibits the growth of photosynthetic microbes which play an important role in microbial colonization of the adsorbent braids. Park and coworkers previously showed that in a dark flume feed with coarsely filtered seawater (150 μm pore size), adsorbents accumulated 75% less microbial mass than adsorbents exposed to light after 42 days at 20°C.¹¹ At this significantly reduced biomass, the disparity between the capacity of the adsorbent in the coarsely filtered dark flume and the finely filtered control flume was negligible. Additionally, the lower temperature of the present experiment is likely to inhibit microbial growth even further. Thus, while some biomass accumulation is observed on the adsorbent, it is unlikely to have a significant impact on the adsorption capacity.

Trace elements including iron (Fe), copper (Cu), zinc (Zn), and V are also adsorbed and are competitors to U for amidoxime adsorption sites.^{12,13} V, in particular, binds very favorably to amidoxime and is present at a slightly higher concentration in Sequim Bay than the 30 nM global average concentration.¹⁴ For this study, the mass of V adsorbed over the 28 day exposure period was 1.9 mg/g adsorbent for small LCW braids in Cage B and 1.26 mg/g adsorbent for large LCW braids in Cage C. A greater mass of V is adsorbed on LCW-MSL-10 reaching about 4.0 mg/g adsorbent after 28 days at 20°C.⁸ This disparity could be explained by a few different factors though further analysis of the LCW adsorbent will be needed to determine the precise mechanism. Past analysis of ORNL's AF1 and AI8 amidoxime adsorbents has shown that adsorption of V is not significantly impacted by temperature.¹⁰ If this behavior can be extended to the LCW

adsorbents, then this would suggest significant refinement of the present LCW materials over earlier formulations.

Compared to the materials developed at ORNL, V adsorption on the LCW adsorbent is quite low for the same V aqueous concentration. At 8°C, the adsorbed mass of V after 28 days exposure to Sequim Bay seawater for ORNL's AF1 and AI8 adsorbents formulated in small braids was approximately 8.5 mg/g adsorbent and 8.0 mg/g adsorbent, respectively.¹⁰ This makes the V/U ratio (w/w) of ORNL adsorbents ~8 at 8°C; while the V/U ratios of LCW adsorbents tested in the present study are only ~1.2 for braids of a similar size. Indeed, one unique feature of LCW adsorbents is their much lower V adsorption.⁴ Although some recent studies^{15,16} have indicated that U and V do not directly compete for all of the same adsorption sites, limiting V uptake can still be advantageous. This is due to V's high binding affinity with certain amidoxime sites that are also important in U adsorption. V removal from these sites requires harsh acidic treatment that damages the adsorbent to effectively strip V.¹⁷ Thus by substantially reducing the adsorption of V, it is possible to significantly increase the reusability of the adsorbent, which is critical to the economic viability of U recovery from seawater.¹⁸

Of the remaining trace elements, Fe is the most important with an amidoxime binding strength and adsorption rate similar to those of U.^{19,20} The 28-day adsorption capacity was 1.90 mg Fe/g adsorbent for the Cage B small braids and 1.71 mg Fe/g adsorbent for the Cage C large braids. This adsorption rate is roughly on par with the adsorption of V and several times greater than that of U, in terms of molar adsorption, while having a total aqueous concentration, in feed seawater, about 15 times higher than the concentration of V. Fe complexation in seawater is, however, very complex with a

large proportion of aqueous Fe in both organic and inorganic forms that are unavailable for adsorption on amidoxime adsorption sites.¹³ Thus, based solely on the total aqueous concentration, it is difficult to accurately assess the performance of the LCW materials with respect to their selectivity for Fe over U. Adsorption of Cu on both samples is effectively negligible with only about 30 µg adsorbed per g adsorbent on the small braids in Cage B. Lastly, while the molar adsorption of Zn is comparable to U, the binding affinity of the amidoxime ligands for Zn is not precisely known, though it appears to be weak.^{13,21}

The adsorption capacity for U, V, and Zn on both the Cage B small braids (Figure 4.3a) and Cage C large braids (Figure 4.3b), and the aqueous concentration of U and V (Figure 4.4) over the experimental period were simulated using the modeling methodology previously described. Estimates of the adsorption capacity were made by adjusting the forward and reverse rate constants for both samples. Initially, this approach underpredicted the aqueous concentration in the flume, thus a correction was applied reducing the total simulated adsorbent mass by 15%. Most of this correction can be attributed to the methyl acrylate comonomer which makes up 8% of the braids' total mass and does not participate in adsorption. Additionally, when the braids are attached to the cage frame the base of the braid is tightly bound significantly constricting the flow of seawater through that region of the braid. Thus the adsorbent mass located in the constricted area is, aside from material on the surface of the braid, unavailable for adsorption.

Biofouling was assumed to have no impact on the capacity of the adsorbent. With this rate information, it is possible to simulate the adsorbent's 56-day and saturated

adsorption capacities. These are summarized for the Cage B small braids in Table 4.3 and for Cage C large braids in Table 4.4. The predicted salinity normalized adsorption capacities on the Cage B small braids for U, V, and Zn are 2.45 mg, 2.63 mg, and 0.48 mg per g adsorbent at 10.8°C, respectively. For the large braids in Cage C, the predicted salinity normalized capacities were 1.78 mg U, 1.92 mg V, and 0.35 mg Zn per g adsorbent at 10.8°C.

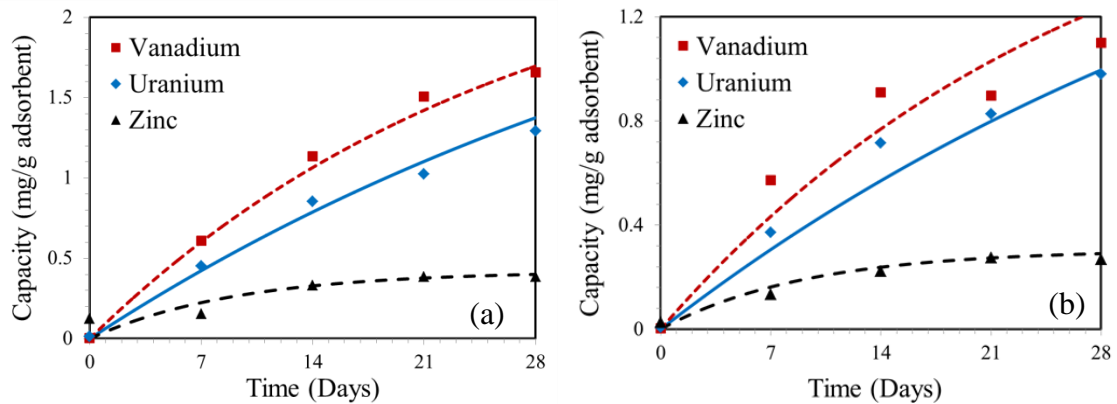


Figure 4.3. Simulated (lines) and experimental adsorption capacities (mg adsorbate/g adsorbent) for V, U, and Zn over a 28 day exposure period for (a) Cage B small braids and (b) Cage C large braids in the raceway. The analytical error is approximately 5%, as reported by Gill et al. (2016).¹²

Based on the work of Kuo and coworkers,¹⁰ the U adsorption capacity of ORNL's AF1 and AI8 adsorbents can be simulated at our experimental temperature in Sequim Bay seawater. This results in a salinity normalized U adsorption capacity of 1.68 mg/g adsorbent for AF1 and 1.36 mg/g adsorbent for AI8 at 10.8°C after 56 days. With respect to V, at the lowest temperature examined by Kuo and coworkers (8°C), the salinity normalized V adsorption capacities after 56 days for AF1 and AI8 in Sequim Bay seawater were 13 mg/g adsorbent and 14 mg/g adsorbent, respectively. Thus at reduced

temperatures, the small LCW braids are expected to significantly outperform both the AF1 and the AI8 adsorbent small braids with respect to U capture, while also adsorbing substantially less V.

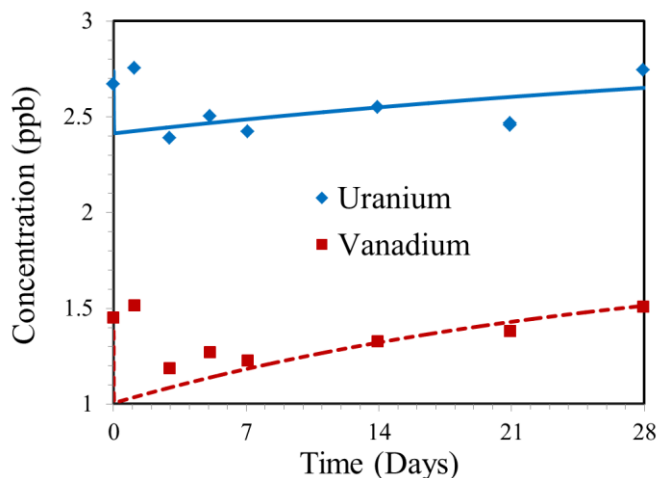


Figure 4.4. Measured and simulated (lines) aqueous concentrations (ppb) for U and V in the raceway over a 28-day exposure period. The analytical error is approximately 5%, as reported by Gill et al. (2016).¹²

To estimate the performance of the LCW braids at higher temperatures, at least one additional reference point is needed. Thus, it was assumed that at 20°C adsorption on the LCW braids under ideal conditions is comparable to the similar LCW-MSL-10 previously studied.⁸ From these data, the forward and reverse rate constants for adsorption of V, U, and Zn can be estimated and used in the adsorption model. For the purpose of this simulation, V adsorption was assumed to increase with increasing temperature. This is not necessarily the case but, as noted previously, it is a strong possibility and cannot be ruled out based on our current knowledge of the material. With this kinetic information, the salinity normalized adsorption capacities in the raceway can

be estimated at 20°C. The simulated 56-day capacities for U and V at 20°C on the Cage B small braids are 4.68 mg and 4.44 mg/g adsorbent, respectively (Table 4.3). Once again, the LCW adsorbent outperforms both the AF1 and AI8 adsorbents for samples of similar braid size though to a lesser degree than at 10.8°C, adsorbing only 20% more U than the AF1 adsorbent at 20°C compared to 45% more at 10.8°C. Additionally, the adsorption of V is still substantially lower than the 13 mg/g adsorbent on AF1 small braids and 16 mg/g adsorbent on observed AI8 small braids.¹⁰

Table 4.3. Simulated 56-day salinity normalized raceway adsorption capacity (mg/g) and saturated adsorption capacity (mg/g) for V, U, and Zn on the Cage B small braids.

Element	56-day Capacity (mg/g adsorbent)			Saturation Capacity (mg/g adsorbent)		
	10.8°C	20°C	31°C	10.8°C	20°C	31°C
V	2.63	4.44	6.91	3.00	5.97	12.32
U	2.45	4.68	7.77	3.49	5.53	9.07
Zn	0.48	0.75	1.23	0.48	0.75	1.23

Table 4.4. Simulated 56-day salinity normalized raceway adsorption capacity (mg/g) and saturated adsorption capacity (mg/g) for V, U, and Zn on Cage C large braids.

Element	56-day Capacity (mg/g adsorbent)			Saturation Capacity (mg/g adsorbent)		
	10.8°C	20°C	31°C	10.8°C	20°C	31°C
V	1.92	3.24	5.05	2.20	4.08	9.30
U	1.78	3.39	5.65	2.57	4.03	5.43
Zn	0.35	0.54	0.90	0.35	0.55	0.89

On the larger braids (Table 4.4), 56-day salinity normalized adsorption is simulated to be about 29% lower than on the small braids for both U and V. This estimate

was obtained by assuming that the impact of adsorbent scale up remains constant at all temperatures. With experimentally determined rate information for 10.8°C and an estimate of the rate constants at 20°C, a rough estimate of the forward and reverse rate constants can be obtained at other temperatures using the Arrhenius equation and applied to the adsorption model. Thus, the simulated 56-day 31°C U and V capacities are 7.77 mg/g adsorbent and 6.91 mg/g adsorbent, respectively, for the Cage B small braids (Table 4.3). At 31°C and for adsorbent braids of similar size, AF1 matches the LCW adsorbent with a 56-day U adsorption capacity of 7.8 mg/g adsorbent, though the adsorption on AI8 is lower at 6.5 mg/g adsorbent. Nevertheless, V adsorption on the AF1 adsorbent is ~3.4 times higher than is simulated to adsorb on LCW small braids at 31°C. Thus the LCW materials are expected to outperform or match adsorption of ORNL's AF1 and AI8 adsorbents of similar size at all relevant temperatures, while also having a substantially reduced affinity for V. Considering LCW's potential for lower cost production and conditioning, they may offer an avenue to notably reduce the cost of U recovery from seawater.

4.4 Conclusions

The recovery of U from seawater has been an area of significant interest for the past seven decades with many recent studies focusing on amidoxime based materials. Nevertheless, the cost of U recovery remains high with a large portion of this arising from the synthesis and alkaline treatment of the amidoxime based materials. This study examines the efficacy of an amidoxime adsorbent derived from acrylic-fibers and treated with sodium hydroxide rather than the more expensive radiation induced graft

polymerization synthesis technique and potassium hydroxide treatment generally used for amidoxime materials.

Adsorption experiments were performed with adsorbent braids of two different sizes in a recirculating raceway flume system for 28 days. The small-size LCW braids in raceway Cage B were found to consistently outperform the large-size braids in raceway Cage C with respect to U adsorption, though the adsorption of V and other competing ions was also higher. The results thus suggest the potential inhomogeneous adsorbent quality when adsorbent size was scaled up. These results were then used for modeling of adsorption kinetics and the simulation of 56-day capacity results.

At the experimental temperature of $\sim 10.8^{\circ}\text{C}$, the 56-day U capacity was simulated for Cage B small braids to be 2.45 mg/g adsorbent compared to a simulated 1.68 mg and 1.36 mg/g adsorbent for ORNL's AF1 and AI8 adsorbents of similar size. The small braids were simulated to continue outperforming both ORNL adsorbents at 20°C , though by 31°C the small braids' simulated U capacity was slightly less than the AF1 adsorbent capacity. Across all temperatures, the small braids' uptake of V was significantly lower than for both the AF1 and AI8 adsorbents. Thus at lower temperatures, LCW adsorbents are expected to outperform both AF1 and AI8 adsorbents with respect to U adsorption, while matching their adsorption at higher temperatures. This behavior, combined with their lower production and alkaline treatment costs, makes the LCW material an attractive potential adsorbent for U resource recovery from seawater. The LCW adsorbents are also shown to adsorb significantly less V, thus reducing the need for harsh elution of the adsorbent and increasing its reusability.

4.5 Acknowledgments

The development of this chapter was a collaborative effort among my co-authors and myself and is the main subject of the following manuscript that is to be submitted for publication: A. Wiechert, A. Ladshaw, L.-J. Kuo, H.-B. Pan, J. Strivens, N. Schlafer, J.R. Wood, C. Wai, G. Gill, S. Yiacoumi, C. Tsouris. Uranium Resource Recovery from Seawater using Amidoxime-Based Braided Polymers Synthesized from Acrylic Fibers. Under internal review, October 31st, 2019.

4.6 References

- 1) Das, S.; Liao, W.P.; Byers, M.; Tsouris, C.; Janke, C.J.; Mayes, R.T.; Schneider, E.; Kuo, L.J.; Wood, J.R.; Gill, G.A.; Dai, S. Alternative Alkaline Conditioning of Amidoxime Based Adsorbent for Uranium Extraction from Seawater. *Ind. Eng. Chem. Res.* **2016**, *55*, 4303-4312.
- 2) Das, S.; Oyola, Y.; Mayes, R.; Janke, C.; Kuo, L-K.; Gill, G.; Wood, J.; Dai, S. Extracting Uranium from Seawater: Promising AF Series Adsorbents. *Ind. Eng. Chem. Res.* **2016**, *55*, 4110-4117.
- 3) Das, S.; Oyola, Y.; Mayes, R.T.; Janke, C.J.; Kuo, L.K.; Gill, G.; Wood, J.R.; Dai, S. Extracting Uranium from Seawater: Promising AI Series Adsorbents. *Ind. Eng. Chem. Res.* **2016**, *55*, 4103-4109.
- 4) Pan, H-B.; Wai, C.M.; Kuo, L-J.; Gill, G.A.; Wang, J.S.; Joshi, R.; Janke, C.J. A Highly Efficient Uranium Adsorbent Derived from Acrylic Fiber for Extracting Uranium from Seawater. Under review **2019**.
- 5) Wood, J.R.; Gill, G.A.; Kuo, L.J.; Strivens, J.; Choe, K.Y. Comparison of Analytical Methods for the Determination of Uranium in Seawater Using Inductively Coupled Plasma Mass Spectrometry. *Ind. Eng. Chem. Res.* **2016**, *55*, 4344-4350.
- 6) Kim, J.; Oyola, Y.; Tsouris, C.; Cole, C. R.; Mayes, R. T.; Janke, C. J.; Dai, S. Characterization of Uranium Uptake Kinetics from Seawater in Batch and Flow-Through Experiments. *Ind. Eng. Chem. Res.* **2013**, *52*, 9433-9440.

- 7) Ladshaw, A.; Kuo, L.J.; Strivens, J.; Wood, J.; Yiacoumi, S.; Tsouris, C.; Gill, G. Influence of Current Velocity on Uranium Adsorption from Seawater Using an Amidoxime-Based Polymer Fiber Adsorbent. *Ind. Eng. Chem. Res.* **2017**, *56*, 2205-2211.
- 8) Gill, G.; Kuo, L.-J.; Strivens, J.; Wood, J.; Schlafer, N.; Janke, C.; Das, S.; Mayes, R.; Saito, T.; Brown, S.; Tsouris, C.; Wai, C.; Pan, H.-B. *Summary of Adsorption Capacity and Adsorption Kinetics of Uranium and Other Elements on Amidoxime-based Adsorbents from Time Series Marine Testing at the Pacific Northwest National Laboratory*. PNNL-2589, Pacific Northwest National Laboratory, 2016.
- 9) Ladshaw, A.P.; Wiechert, A.I.; Das, S.; Yiacoumi, S.; Tsouris, C. Amidoxime Polymers for Uranium Adsorption: Influence of Comonomers and Temperature. *Materials*. **2017**, *10*, 1268.
- 10) Kuo, L.-J.; Gill, G.; Tsouris, C.; Rao, L.; Pan, H.-B.; Wai, C.; Janke, C.; Strivens, J.; Wood, J.; Schlafer, N.; D'Alessandro, E. Temperature Dependence of Uranium and Vanadium Adsorption on Amidoxime-Based Adsorbents in Natural Seawater. *Chemistry Select*. **2018**, *3*, 843-848.
- 11) Park, J.; Gill, G.; Strivens, J.; Kuo, L.J.; Jeters, R.; Avila, A.; Wood, J.; Schlafer, N.; Janke, C.; Miller, E.; Thomas, M.; Addleman, R.; Bonheyo, G. Effect of Biofouling on the Performance of Amidoxime-Based Polymeric Uranium Adsorbents. *Ind. Eng. Chem. Res.* **2016**, *55*, 4328-4338.
- 12) Gill, G.; Kuo, L.-J.; Janke, C.; Park, J.; Jeters, R.; Bonheyo, G.; Pan, H.-B.; Wai, C.; Khangaonkar, T.; Bianucci, L.; Wood, J.; Warner, M.; Peterson, S.; Abrecht, D.; Mayers, R.; Tsouris, C.; Oyola, Y.; Strivens, J.; Schlafer, N.; Addleman, R.; Chouyyok, W.; Das, D.; Kim, J.; Buesseler, K.; Breier, C.; D'Alessandro, E. The Uranium from Seawater Program at the Pacific Northwest National Laboratory: Overview of Marine Testing, Adsorbent Characterization, Adsorbent Durability, Adsorbent Toxicity, and Deployment Studies. *Ind. Eng. Chem. Res.* **2016**, *55*, 4264-4277.
- 13) Wiechert, A.; Ladshaw, A.; Gill, G.; Wood, J.; Yiacoumi, S.; Tsouris, C. Uranium Resource Recovery from Desalination Plant Feed and Reject Water Using Amidoxime Functionalized Adsorbent. *Ind. Eng. Chem. Res.* **2018**, *57*, 17237-17244.
- 14) Rehder, D. *Bioinorganic Vanadium Chemistry*. John Wiley & Sons, Ltd. West Sussex, England, 2008.

- 15) Ladshaw, A.; Ivanov, A.; Das, S.; Bryantsev, V.; Tsouris, C.; Yiacoumi, S. First-Principles Integrated Adsorption Modeling for Selective Capture of Uranium from Seawater by Polyamidoxime Sorbent Materials. *ACS Appl. Mater. Interfaces*. **2018**, *10*, 12580-12593.
- 16) Ladshaw, A.; Das, S.; Liao, W.-P.; Yiacoumi, S.; Janke, C.; Mayers, R.; Dai, S.; Tsouris, C. Experiments and Modeling of Uranium Uptake by Amidoxime-Based Adsorbent in the Presence of Other Ions in Simulated Seawater. *Ind. Eng. Chem. Res.* **2016**, *55*, 4241-4248.
- 17) Pan, H.-B.; Kuo, L.-J.; Wai, C.; Miyamoto, N.; Joshi, R.; Wood, J.; Strivens, J.; Janke, C.; Oyola, Y.; Das, S.; Mayes, R.; Gill, G. Elution of Uranium and Transition Metals from Amidoxime-Based Polymer Adsorbents for Sequestering Uranium from Seawater. *Ind. Eng. Chem. Res.* **2016**, *55*, 4313-4320.
- 18) Lindner, H.; Schneider, E. Review of cost estimates for uranium recover from seawater. *Energy Economics* **2015**, *49*, 9-22.
- 19) Sun, X.; Xu, C.; Tian, G.; Rao, L. Complexation of glutarimidedioxime with Fe(III), Cu(II), Pb(II), and Ni(II), the competing ions for the sequestration of U(VI) from seawater. *Dalton Trans.* **2013**, *42*, 14621-14627.
- 20) Parker, B.F.; Hohloch, S.; Pankhurst, J.R.; Zhang, Z.; Love, J.B.; Arnold, J.; Rao, L. Interactions of vanadium(IV) with amidoxime ligands: redox reactivity. *Dalton Trans.* **2018**, *47*, 5695-5702.
- 21) Kim, J.; Tsouris, C.; Oyola, Y.; Janke, C.; Mayes, R.; Dai, S.; Gill, G.; Kuo, L.-J.; Wood, J.; Choe, K.-Y.; Schneider, E.; Linder, H. Uptake of Uranium from Seawater by Amidoxime-Based Polymeric Adsorbent: Field Experiments, Modeling, and Updated Economic Assessment. *Ind. Eng. Chem. Res.* **2014**, *53*, 6076-6083.

4.7 Nomenclature

C – Adsorbate concentration in the bulk phase

q – Adsorption capacity

q_{\max} – Theoretical maximum adsorption capacity

L – Capacity still available for adsorption

k_f – Reaction rate constant for forward reaction

k_r – Reaction rate constant for reverse reaction

V – Reactor volume

M_a – Adsorbent mass in reactor

Q – Flowrate

i – Influent index

j – Element index

o – Effluent index

**PART II. NUCLEAR FUEL REPROCESSING OFF-
GAS TREATMENT**

CHAPTER 5: Aging Effect in Silver Exchanged Mordenite

5.1 Introduction

Of the materials considered for iodine capture, silver mordenite (AgZ) adsorbents, and particularly reduced silver mordenite (Ag⁰Z), have been examined extensively and are considered promising for their high iodine adsorption capacity, thermodynamic stability, and regenerative capabilities.¹ Recently, a renewed emphasis has been placed on the development of Ag⁰Z for iodine capture with several studies attempting to provide a greater fundamental understanding of adsorbent activation,² the mechanisms of organic and inorganic iodine adsorption,³⁻⁸ and adsorbent regeneration.⁹ Another significant area of interest is the impact that exposure to off-gas constituents, including oxygen (O₂), water vapor (H₂O), nitric oxide (NO), and nitrogen dioxide (NO₂), have on Ag⁰Z's inorganic iodine (I₂) adsorption capacity.¹⁰⁻¹⁴ All four off-gas constituents will significantly degrade Ag⁰Z performance over long periods of time (e.g., aging); however, the impact of the NO_x gases is the most severe. For instance, the aging effect from exposure to 1% NO in a balance of nitrogen (N₂) yields an 85% reduction in the adsorbent's I₂ capacity after one month.¹² This is significantly more than the 40% reduction observed after six months in dry air.¹⁰ Nevertheless, while exposure to NO and NO₂ is known to dramatically reduce adsorbent performance, the physical and chemical processes that produce these dramatic changes have not yet been investigated.

Thus, the purpose of this study is to examine Ag⁰Z aging with the intent of elucidating the underlying physicochemical processes at play in the mordenite that result in the observed capacity losses. Ag⁰Z samples were aged in gas streams of 1% NO in N₂

and 2% NO₂ in dry air at 150°C for up to six months. Aged samples were characterized using X-ray Absorption Spectroscopy (XAS) before and after I₂ loading to determine silver (Ag) speciation and the contribution of each species to I₂ adsorption over time. With this information, potential mechanisms for adsorbent aging are explored and discussed. Finally, based on the proposed processes, a predictive model for Ag⁰Z aging has been developed based on the Discontinuous Galerkin Off-Gas Separation and Recovery (DG-OSPNEY) modeling framework.¹⁵

5.2 Methodology

5.2.1 Materials

Ag⁰Z samples were prepared from commercially available AgZ (IONEX-Type Ag-900) with a Ag content of 11.9 w.t. % and a silicon-aluminum ratio of 5:1 purchased from Molecular Products Inc. In addition to Ag, the material also contains potassium (K), sodium (Na), calcium (Ca), and iron (Fe) impurities which represent 0.74, 0.4, 0.33, and 0.98 w.t. % of the material, respectively. AgZ samples were delivered as cylindrical pellets with an average diameter of 1.6 mm manufactured from mordenite microcrystals supported by a clay-based binding material. The variance in pellet diameter was ±0.4 mm based on the distribution of pellets between 10 and 16 mesh stainless steel screens. This variation was narrowed using a 12-mesh screen to remove smaller pellets yielding a final average diameter of 1.8 mm. A complete description of the properties of this AgZ was provided in previous work.¹⁶ The reduction of 10 g of AgZ at a time to Ag⁰Z was performed in a 4% hydrogen (H₂) in Argon gas stream (500 mL/min) at 400°C for 24 hr. Before and after reduction, samples were treated in a pure N₂ gas stream at the same

temperature and flowrate used in reduction for 4 hr. This was done to desorb excess moisture before reduction and to remove any physisorbed H₂ after reduction is complete. These reduction conditions ensure that all Ag in the mordenite microcrystals is reduced to metallic silver (Ag⁰), which then migrates to the mordenite's surface forming Ag⁰ nanoparticles.^{9,16} All gases provided from cylinders were purchased from Airgas Inc. and were Certified Standard Grade, with the exception of compressed dry air which was Ultra Zero Grade. This included the 4% H₂ in Argon mixture and pure N₂ used in AgZ reduction, 1% NO in N₂ and 2% NO₂ in dry air mixtures used for aging experiments, and the compressed dry air (1.58 ppm by weight H₂O) used during I₂ loading.

5.2.2 Aging Experiments

Ag⁰Z samples were aged by exposing them to gas stream mixtures of 1% NO in N₂ and 2% NO₂ in dry air for various periods of time (i.e., one day, one week, one month) at a constant temperature of 150°C. Before this exposure, samples were dried in a N₂ flow for 4 hr at the exposure temperature. Glass columns with an internal diameter of 2.5 cm and a total height of 7.0 cm, divided equally into four chambers, were used to hold the Ag⁰Z samples. For both gas mixtures, two of these columns were placed in series and each chamber was loaded with one g of Ag⁰Z allowing for up to eight samples to be tested in each gas mixture. Compressed gas cylinders were used to provide a steady gas stream to the system with a flow rate of 500 ml/min regulated using a Cole-Parmer gas mass flow controller (Item # EW-32907). Two ovens (Thermo Scientific Heratherm) were used to ensure that both the sample columns and the incoming gas maintained a constant temperature. Thermal monitors were placed at the entrance of each glass column

to verify that the influent gas stream was at the desired temperature. All parts of the system were connected to one another using stainless steel tubing. A complete diagram of the system used for the aging experiments is given in Figure 5.1.

Once the Ag^0Z sample had been exposed to either the NO or the NO_2 mixture for a long enough period of time, it was either stored under an Argon atmosphere for characterization or transferred to the I_2 adsorption system to determine its capacity. The adsorption system and experimental equipment used were identical to a system previously described.¹⁶ In this system, about 0.2 g of aged Ag^0Z was loaded onto a steel screen suspended from a microbalance with a sensitivity of $0.1 \mu\text{g}$. This suspended sample of aged Ag^0Z was then exposed to a stream of dry air with an I_2 concentration of 50 ppmv at 150°C . Mass gain taken from microbalance measurements was used to quantify the I_2 adsorption capacity. When the sample mass stabilized, the I_2 supply was shut off and a clean stream of dry air was allowed to flow through the aged sample to desorb any physisorbed I_2 .

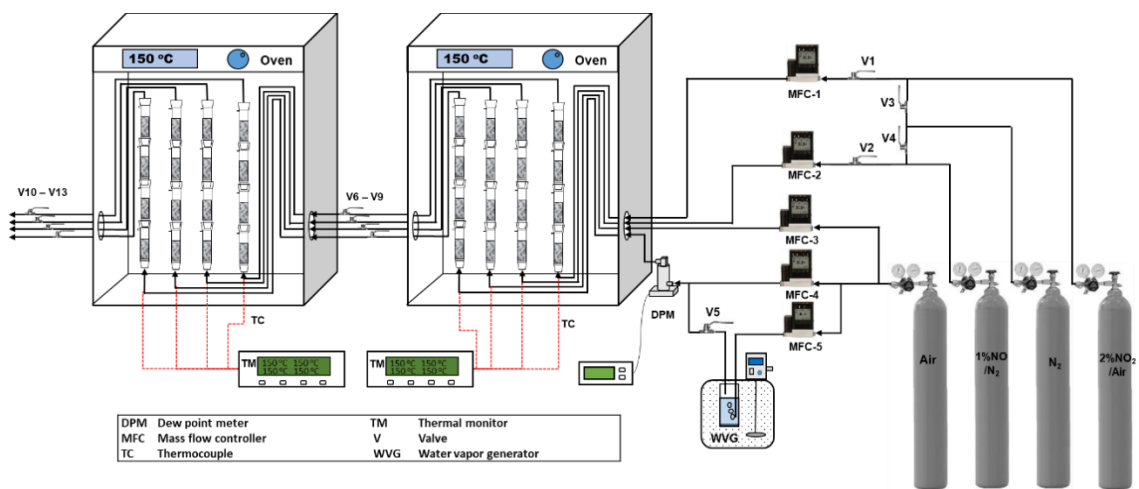


Figure 5.1. Complete schematic of continuous flow aging system; dry air lines and water vapor generator were not used in this study.

5.2.3 XAS Methods

XAS was used to determine how Ag^0Z 's chemical composition changes during aging and how aged samples adsorb I_2 . This analysis was performed at Argonne National Laboratory's Advanced Photon Source using beamline 10-ID-B.¹⁷ Aged Ag^0Z samples were ground with a mortar and pestle to achieve a uniform particle size. From each ground sample, a mass of approximately 10 mg was loaded into a self-supported pallet and tested at the Ag K-edge (25514 eV) in transmission mode. Data were also collected from Ag foil simultaneously to serve as a reference for energy calibration and data alignment. All samples were held under a pure Argon atmosphere at all times from the completion of the initial aging or I_2 loading of the material until completion of the XAS investigations. Analysis of the XAS data, which included spectra normalization, analysis of the X-ray Absorption Near Edge Structure (XANES) region, and linear combination fitting, was performed with Athena, a component of the Demeter software package.¹⁸ Linear combination fitting was performed on normalized $\mu(\text{E})$ spectra from 30 eV below to 100 eV above the edge for all samples. Reference standards for unaged Ag^0Z and AgZ , silver nitrate (AgNO_3), and silver oxide (Ag_2O) were used in combination fitting. From a proportional combination of these selected standards, an approximate XANES spectrum can be simulated and compared against the results obtained experimentally. The approximate spectrum was optimized based on the R-factor and reduced χ^2 fit parameters with the combination of references resulting in the smallest fit parameters used as the most probable representation of the sample. Best fit results for each spectrum are in Appendix B.

5.2.4 Adsorption Modeling

Aging simulations are performed with the DG-OSPNEY model which is developed at the Georgia Institute of Technology.¹⁵ DG-OSPNEY is, in turn, built within the Multiphysics Object Oriented Simulation Environment (MOOSE) modeling framework developed at the Idaho National Laboratory.¹⁹ The MOOSE framework, itself, is responsible for discretization of spatial domains and iteratively solving non-linear systems of equations. Domain discretization may be performed using either continuous or discontinuous finite element methods. Discontinuous methods are less oscillatory for problems derived from conservation laws and, as such, are used in DG-OSPNEY.¹⁵ The non-linear system of equations produced from domain discretization is solved iteratively using the Preconditioned Jacobi Free-Newton Krylov (PJFNK) method. This method incorporates both a non-linear solver based on Newton type methods and a linear Krylov subspace method nested within the non-linear solver. Linear iterations are preconditioned using incomplete lower and upper triangular fractionalization. Line search methods, Back-Tracking for example, are used to control the convergence of the non-linear iterations. DG-OSPNEY establishes the mass and energy conservation equations, formulated in the weak form and defined as piecewise discontinuous, needed to perform column adsorption modeling.

Conservation of mass (Equation 5.1) is defined with respect to each gas species (C_i) and its accumulation (dC_i/dt) in the void space of the column as defined by the bulk bed porosity (ϵ). Accumulation of each species is, in turn, further dependent upon advection, based on an advective velocity of v through the column, dispersion (D_i), and the net adsorption rate (dq_i/dt) multiplied by the adsorbent material's packing density

(ρ_b). The adsorption rate itself (Equation 5.2) is defined using a chemical reaction model where the forward and reverse rate constants are defined by k_f and k_r , respectively. The reaction order with respect to each reactant (ν_j^*) and product (ν_k^*) species is considered to be independent of the species' stoichiometry (ν) in the chemical reaction. For solid species, mass conservation is significantly simplified since advection and diffusion do not need to be considered. Rather, adsorption represented through the net rate of adsorption is the only component of Equation 5.1 that needs to be considered for non-gas phase species.

$$\varepsilon \frac{\partial C_i}{\partial t} + \nabla \cdot (\varepsilon \nu C_i) = \nabla \cdot (\varepsilon D_i \nabla C_i) + \rho_b \frac{\partial q_i}{\partial t} \quad (5.1)$$

$$\frac{\partial q_i}{\partial t} = \nu_i (k_f \prod_j C_j^{\nu_j^*} - k_r \prod_k C_k^{\nu_k^*}) \quad (5.2)$$

Conservation of energy (Equation 5.3) is dependent upon the accumulation of heat (dT/dt) that includes a contribution from both the specific heat of the gas phase (h_g) and adsorbents (h_s) involving their respective densities (ρ and ρ_b). Energy transport as a result of gas advection and material thermal conductivity (K), in addition to heating from adsorption due to the isosteric heat of adsorption for each gas species ($Q_{st,i}$), is also considered. For fixed bed columns, mass and energy fluxes at the inlet are governed by advective and dispersive transport while at the exit a zero gradient condition is defined.¹⁵ For the simulations performed in this study, the aging environment was treated as a thin-bed with otherwise the same characteristics as the experimental system.

$$(h_g \rho \varepsilon + h_s \rho_b) \frac{\partial T}{\partial t} + \nabla \cdot (h_g \rho \varepsilon \nu T) = \nabla \cdot (\varepsilon K \nabla T) + \rho_b \sum_i \frac{\partial (Q_{st,i} q_i)}{\partial t} \quad (5.3)$$

5.3 Results and Discussion

5.3.1: Iodine Capacity Experiments

Results of the I₂ loading experiments on aged Ag⁰Z for 1% NO in N₂ and 2% NO₂ in dry air at 150°C are shown in Table 5.1. The I₂ capacity was measured as a percent mass gained at equilibrium from exposure to 50 ppmv I₂ in dry air. Thus, Ag⁰Z's initial, unaged I₂ capacity of 12.3 w.t. % is equivalent to 0.123 g iodine adsorbed per g adsorbent or a Ag utilization rate of ~87%. Aging in the 2% NO₂ environment is significantly faster than in 1% NO, with the adsorbent losing almost 59% of its initial I₂ capacity after only 12 min. After five hr in 2% NO₂, the adsorbent has an I₂ capacity of only 1.4 w.t. % which amounts to a loss of over 88% of its initial capacity. The I₂ capacity in 2% NO₂ aged samples continues to decline after one month, two months, and four months of aging with a final six-month capacity of 0.35 w.t. % which is about 2.8 % of the Ag⁰Z initial capacity. In the 1% NO environment, the I₂ capacity drops to 7.48 w.t. % after one day and then to 4.95 w.t. % after one week from the initial 12.3 w.t. % on the unaged adsorbent. After one month in 1% NO, the I₂ capacity declines to 1.4 w.t. % which is the same as the NO₂ aged sample's five hr capacity. The NO aged sample's capacity further drops to 1.27 w.t. % after four months and finally to 0.45 w.t. % after six months. As such, while aging in 2% NO₂ is significantly faster than in 1% NO, the degree of aging over the long term period is roughly comparable.

These results clearly show that exposure to either NO or NO₂ significantly impacts the I₂ capacity of Ag⁰Z and, in the case of NO, are consistent with previous analysis.¹² Previous studies of capacity losses in 2 % NO₂ were performed using a static atmosphere and, as such, are not comparable to the results obtained here in a continuous

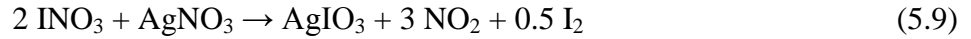
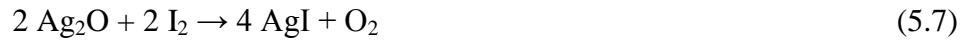
flow system.¹⁴ The I₂ adsorption capacity alone does not, however, give sufficient insight into the processes that govern adsorbent aging. For example, NO₂ aging likely involves three primary processes that allow for oxidation and dissolution of the Ag nanoparticles in Ag⁰Z which are responsible for the adsorbent's high unaged adsorption capacity.

Table 5.1: Equilibrium I₂ capacity measured in weight percent gained after aging Ag⁰Z for a variety of times in the 1% NO in N₂ and 2% NO₂ in dry air aging environments at 150°C.

1% NO in N ₂		2% NO ₂ in Dry Air	
Aging Time	I ₂ Capacity (w.t. %)	Aging Time	I ₂ Capacity (w.t. %)
Unaged	12.3	Unaged	12.3
1 day	7.48	12 min	5.10
1 week	4.95	5 hr	1.40
1 month	1.40	1 month	0.98
2 month	1.62	2 month	0.66
4 month	1.27	4 month	0.30
6 month	0.47	6 month	0.35

The first of these processes is the dissociative adsorption of O₂ on Ag⁰ forming a Ag₂O film on the surface of the Ag nanoparticle. This process is known to occur at the experimental temperature of 150°C with the net reaction shown in Equation 5.4.²⁰⁻²² This is followed by adsorption of NO₂ onto the Ag₂O yielding AgNO₃ with an overall reaction described by Equation 5.5.²³ AgNO₃ will then migrate into the mordenite's channels and exchange at protonated binding sites (HZ) returning the Ag to its original state prior to H₂ reduction (Equation 5.6). Thus, at any given time, there are four significant species of Ag that may exist in the NO₂ aged sample. This process could be simplified substantially if we only needed to consider I₂ adsorption on Ag⁰, however, all four species are known to adsorb I₂. Silver iodide (AgI) is formed from adsorption of I₂ on Ag₂O by the reaction

described in Equation 5.7, while adsorption on AgNO₃ proceeds by the reactions given in Equations 5.8 through 5.10.²⁴ The reaction pathway for I₂ adsorption on unreduced AgZ is unknown; however, there is clear evidence that a notable quantity is adsorbed on unreduced AgZ in the form of α-phase AgI.^{3,9,11} These other sources of AgI cannot be resolved based solely on the total I₂ capacity and, as such, will require additional examination to analyze properly.



5.3.2 XAS Results

To determine which Ag species are present in the aged mordenite and their contribution to I₂ adsorption, several aged samples were characterized before and after I₂ adsorption using XAS analysis. In this case the XANES, which includes the region of the XAS spectrum starting before the absorption edge and continuing to 50-100 eV beyond, was analyzed. The XANES is sensitive to metal oxidation states and the geometry of coordination due to selection rules dictating the probability of X-ray absorption. XANES of unreduced AgZ, Ag⁰Z, and mordenite aged in 1% NO and 2% NO₂ are shown in Figure 5.2. The spectrum of the as-received AgZ shows an absorption edge with the

inflection point occurring at 25520 eV and white line at 25525 eV, but it is otherwise devoid of any significant features. In contrast, the reduced Ag^0Z shows a spectrum similar to Ag foil due to the formation of Ag^0 clusters in Ag^0Z after reduction by H_2 .^{3,9,15,25} The spectra for samples aged in NO and NO_2 are very similar to the spectrum for AgZ, in that they show a dominant white line without any significant subsequent oscillations. These conspicuous differences apparent in the spectra allow for straightforward analysis by linear combination fitting, affording a means by which the ratio of Ag species present in the aged mordenite can also be quantified.

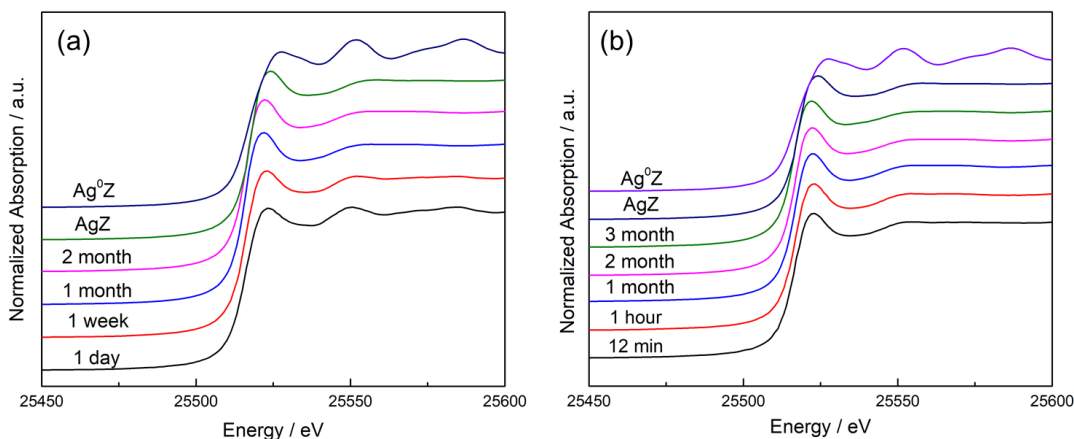


Figure 5.2. Normalized Ag K-edge XANES of AgZ aged in (a) 1% NO in N_2 and (b) 2% NO_2 in dry air.

Four different Ag standards were used throughout the linear combination fitting analysis, representing the anticipated chemical environments (AgZ , Ag^0Z , Ag_2O , and AgNO_3) formed under the aging conditions previously discussed. Linear combination fits are shown in Appendix B for samples aged in 2% NO_2 before (Figure B1) and after I_2 adsorption (Figure B2), and for samples aged in 1% NO before (Figure B3) and after I_2 adsorption (Figure B4). From these fits, the breakdown of Ag species as a percentage of

total Ag is determined for samples aged in both the 2% NO₂ (Figure 5.3) and 1% NO (Figure 5.4) environments. For samples aged in the 2% NO₂ stream, Ag⁰ is rapidly oxidized to either AgNO₃ or AgZ with only about 1% of Ag remaining in the reduced state after 12 min. After one hr, all Ag⁰Z in the NO₂ aged system has been oxidized leaving about 67.5% of Ag in the form of AgZ and the remaining 32.5% as AgNO₃. There is an increase in the percentage of Ag in the form of AgNO₃ after one month of aging in 2% NO₂, which can be attributed primarily to material non-uniformity. The remaining 2% NO₂ aging times of two months and three months have the same proportion of Ag in the form of AgZ (71%) and AgNO₃ (29%).

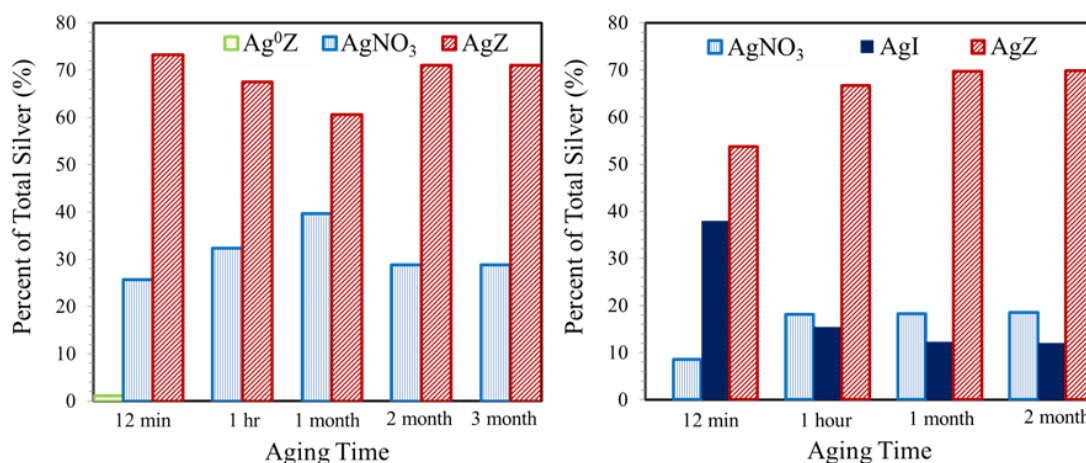


Figure 5.3. Proportion of each Ag species present in 2% NO₂ aged mordenite samples as a percent of total Ag before (left) and after (right) I₂ adsorption determined from linear combination fitting of XANES data.

No Ag₂O is observed for any of the 2% NO₂ aging times. This is not particularly surprising since the vast majority of Ag⁰Z has been oxidized within the first 12 min in 2% NO₂. As previously discussed, Ag₂O is formed by the reaction described in Equation 5.4 and serves as an intermediary between Ag⁰Z and AgNO₃. Thus, we would only expect to

see a noticeable concentration of Ag_2O form when a reasonably large amount of Ag^0Z is present in the system and disappear when Ag^0Z has been exhausted. While the reactions are different for 1% NO aging, a similar effect is observed where a small concentration of Ag_2O is maintained early on, when a significant concentration of Ag^0Z persists. Another interesting feature observed here is the persistent concentration of AgNO_3 that remains even in samples aged in NO_2 for more than two months. Ideally, all AgNO_3 should migrate into the mordenite and exchange at protonated sites as described in Equation 5.6. Thus, it would be reasonable to expect AgNO_3 to make up a large proportion of the total Ag early on and then decline over time as a result of migration. Instead, the percentage of Ag in the form of AgNO_3 does not significantly change between 12 min (25.7%) and three months (29%) in the NO_2 environment.

The most likely explanation for the behavior of AgNO_3 lies in the structure of the mordenite crystal. Binding sites are located in the main channels, side channels, and side pockets of the mordenite with a roughly 50/50 split between the main and side areas.^{26,27} In this study, the mordenite crystal contains 12-member main ($7.0 \times 6.5\text{\AA}$) channels, one set of 8-member side channels ($5.7 \times 2.6\text{\AA}$) that run parallel to the main channels and another set of 8-member side channels ($3.4 \times 4.8\text{\AA}$) that connect the previous two types of channels.⁴ Small 5-member side pockets are also present and can be found between the main and side channels (Figure B5). The size of the side channels and side pockets may, therefore, simply be too small to allow migration of AgNO_3 . This is known to occur with larger molecules that are only able to diffuse through the crystals main channels and will not enter the side areas.⁴ Another, more likely, possibility is that the structure of the side spaces alters the site exchange reaction pathway to make the process less favorable and

thus prevents the reaction from occurring. A similar phenomenon is observed in the adsorption of I_2 on AgZ where main-channel sites interact strongly enough with I_2 to cleave the I-I bond, while on side-channel sites I_2 is outcompeted by H_2O .⁶ In either case, the persistent concentration of $AgNO_3$ can be attributed to $AgNO_3$ being unable to exchange at protonated sites in the mordenite's side channels and pockets.

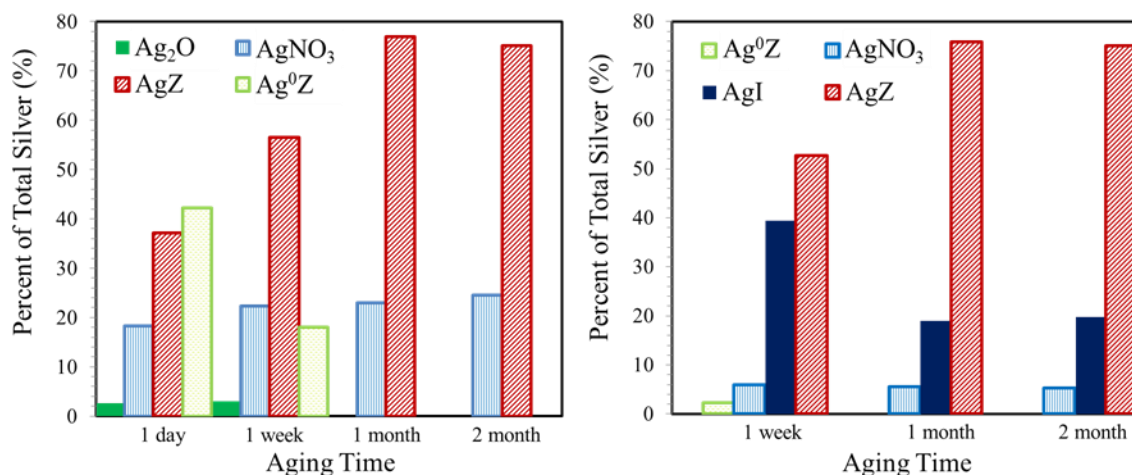


Figure 5.4. Proportion of each Ag species present in 1% NO aged mordenite samples as a percent of total Ag before (left) and after (right) I_2 adsorption determined from linear combination fitting of XANES data.

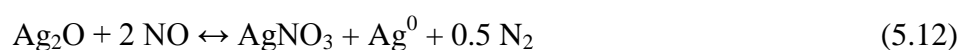
After I_2 adsorption, the percentage of total Ag in the form of AgI is 37.9%, 15.4%, 12.3%, and 12.0% for samples aged in 2% NO_2 for 12 min, one hr, one month, and two months, respectively. By analyzing the change in the concentration of Ag^0Z , AgZ , and $AgNO_3$ after I_2 adsorption, the contribution of each species to the formation of AgI can be estimated. For 12 min aging in NO_2 (Figure 5.3), the concentrations of AgZ and $AgNO_3$ drop by 19.6% (73.2% to 53.6%) and 17.3% (25.7% to 8.4%) of total Ag after I_2 adsorption. Thus, of the 37.9% of all Ag in the form of AgI, the adsorption of I_2 on AgZ

and AgNO₃ accounts for 51.7% (19.6% out of 37.9%) and 45.6% (17.3% out of 37.9%) of AgI formed, respectively, with only 2.6% arising from adsorption on Ag⁰Z after 12 min. By one hr of aging, AgZ's contribution to I₂ adsorption has declined significantly with only 5.8% of AgI forming in the α -phase, while the remainder comes from adsorption on AgNO₃. This is also the case after two months in the NO₂ environment with a comparable amount of I₂ adsorbed on AgZ. This declining contribution to I₂ adsorption from AgZ is likely related to the increasing portion of AgNO₃ that is seemingly unavailable for I₂ adsorption.

At equilibrium, all AgNO₃ should be replaced by AgI in accordance with the reactions given in Equations 5.8 through 5.10. A significant portion of AgNO₃, however, does not adsorb I₂ and the amount of unavailable AgNO₃ grows over time from only ~33% of AgNO₃ at 12 min to almost 64% of AgNO₃ after two months. AgNO₃ that is unavailable for I₂ adsorption could be attributed to the formation of immobile AgNO₃ clusters stabilized within the mordenite crystal's main channels. Interactions that stabilize molecular clusters within the mordenite channels have already been observed. AgI in the α -phase, for example, is usually only stable above 147°C in clusters >10 nm in size, but inside the mordenite main channels sub-nanometer clusters are stable to temperatures as low as 95°C through mordenite-cluster interactions.³ Additionally, the congregation of these immobile clusters within the main channels would obstruct access to the binding sites needed for the formation of α -phase AgI, explaining the declining contribution to I₂ adsorption from AgZ.

Aging of the adsorbent in the 1% NO environment is also shown to significantly reduce I₂ adsorption capacity, though this effect is much slower than the aging effect in

2% NO₂. After a single day of NO aging, Ag⁰Z has declined drastically representing only 42.3% of all Ag in the system. By the end of the first week, the proportion of Ag in the reduced form has declined even further to 18% of total Ag, and after one month of aging in 1% NO, it has vanished entirely. A small quantity (~3% of total Ag) of Ag₂O is present at both the one day and the one week aging times but disappears from the system after one month alongside Ag⁰Z. Ag₂O is formed in this environment from the dissociative adsorption of NO catalyzed by Na adsorbed to the surface of the Ag nanoparticle (Equation 5.11).^{28,29} Na is present in the mordenite as a metal impurity with a Ag-Na molar ratio of 6.4:1. In the absence of Na, NO will not dissociatively adsorb on metallic Ag above ~20°C when the surface becomes unreactive.³⁰ Without dissociative adsorption of NO, it is not possible for either Ag₂O or AgNO₃ to form as observed. AgNO₃ makes up 18.3% of total Ag after one day with a slight increase in its proportion of total Ag to 22.4% after one week and 23% after one month. The net reaction that describes NO adsorption on Ag₂O to form AgNO₃ is given in Equation 5.12.^{31,32} AgZ makes up 37.2%, 56.5%, and 77% of total Ag after one day, one week, and one month aging in the 1% NO environment. Interestingly, migration of AgNO₃ to the mordenite's channel binding sites in 1% NO seems to be much slower than in 2% NO₂ where the system reached equilibrium after one hr. This may be attributed to a delay in the dissolution of the Ag nanoparticles with AgNO₃ residing on the particle's surface for some period of time in NO since it is significantly less reactive than NO₂.

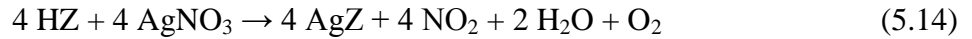


Following I₂ exposure, AgI makes up 39.4% of total Ag on the sample aged for one week and 19% on the sample aged for one month. For the one week aged sample, the two largest contributors to I₂ adsorption are Ag⁰Z (~40%) and AgNO₃ (~42%) with small contributions from Ag₂O (~8%) and α-phase adsorption on AgZ (~10%). After one month, Ag₂O and Ag⁰Z disappear from the system, and adsorption on AgNO₃ represents nearly all, about 93.5%, of the I₂ adsorption observed. As with NO₂ aging, a permanent AgNO₃ concentration that is unavailable for I₂ adsorption develops, though it is significantly smaller in this environment. The percentage of total Ag occupied by the unavailable AgNO₃ phase is 5.2% in the 1% NO stream after 2 months compared to 18.4% in 2% NO₂. Nevertheless, there is no significant increase in the contribution to I₂ adsorption from the α-phase suggesting that the interior AgZ binding sites are still inaccessible. This can be explained through the behavior of Fe impurities, 6.3:1 Ag-Fe molar ratio, present in the material. After H₂ reduction, all Fe present in the mordenite crystal will be reduced to Fe (II) and will be bound to the mordenite as an uncomplexed ion.³³ In this state, and without any means of oxidizing to Fe (III) in the 1% NO environment, Fe is somewhat mobile and can migrate into the mordenite main-channels where there is sufficient space to form immobile dinitrosyl and trinitrosyl complexes.^{34,35} These nitrosyl complexes, therefore, likely compete for space with the immobile AgNO₃ clusters significantly reducing the concentration of that Ag phase.

5.3.3 Aging Modeling

Utilizing the chemical processes previously discussed and with experimental results as a point of comparison, Ag⁰Z aging simulations were performed for both the 1%

NO in N₂ and 2% NO₂ in dry air environments. The aging system was simulated as a thin bed with a diameter of 2.5 cm, thickness of 0.1 cm, and porosity of 0.333 which yield an adsorbent mass of one g. Simulated Ag⁰Z aging results for 2% NO₂ in dry air at 150°C are compared against the XAS data for aging times up to two months in Figure 5.5. Since no Ag₂O is observed for this environment, Equations 5.4 and 5.5 may be combined to form Equation 5.13. This reaction is treated as irreversible here because it includes the additional step of migration off of the Ag particle but not migration into the mordenite channels. Migration to the channels is governed by Equation 5.6 which, when combined with the decomposition of nitric acid,³⁶ yields the net reaction given by Equation 5.14. Finally, Equation 5.15 describes the formation of AgNO₃ clusters unavailable for I₂ adsorption, where θ is a representation of the available sites for cluster formation and is defined as one fourth of the main channel binding sites.



As noted previously, binding sites are split between the main and side channels on an approximately 50/50 basis. For the mordenite examined in this study, unoccupied binding sites accounted for, on average, about 10% of all binding sites. Thus, the percentage of occupied sites in the main channel can generally range from 40 to 50% of all sites, though in some cases additional variance may be possible based on the main-side site ratio. In the case of 2% NO₂, it was assumed that the number of occupied sites in the main channel represented 41% of all sites based on the AgZ concentration in well-aged (\geq two months) samples. Reaction rate constants, which were adjusted until a

reasonable fit of the data was attained, are shown in Table 5.2. Generally, good agreement was obtained between experimental data and simulated aging using this methodology. Some variations were observed, such as at 12 min where the simulation underpredicts AgZ as a percentage of total (73.2% vs. 71.6%) and at one hr where it overpredicts the data (67.5% vs. 71.7%). This is to be expected given that the Ag⁰Z adsorbent is not entirely uniform. Significant deviation between experimental and simulated results is observed only for the one month aging time for AgZ and AgNO₃. This can also be attributed to material non-uniformity which, as noted previously, is unusually high but not improbable for the one month aged sample.

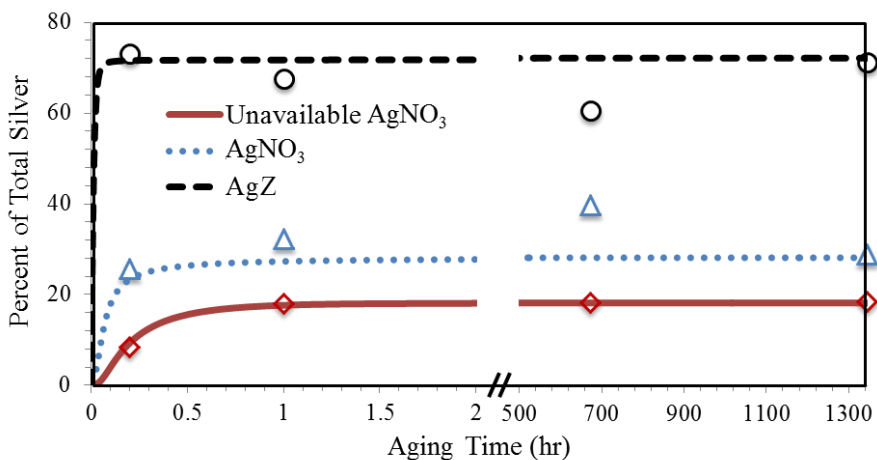
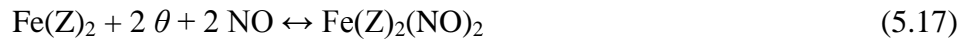
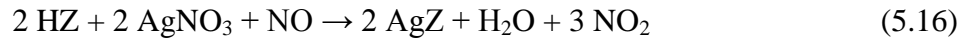


Figure 5.5. Simulation results compared against XAS combination fitting data for aging at 150°C in 2% NO₂ in dry air for aging times up to two months.

For aging in 1% NO in N₂, the dissociative adsorption of NO and adsorption of NO on Ag₂O are simulated using the reactions represented by Equations 5.11 and 5.12. Since Ag₂O is observed in this system, these reactions may not be combined into a single reaction as was the case in 2% NO₂. Occupied sites in the main channel were assumed to

represent 45% of all binding sites in the mordenite for the NO environment. The concentration of adsorbed Na, which acts as a catalyst for dissociative NO adsorption, was assumed to be constant. Migration of AgNO₃ off of the Ag particle surface and into the mordenite channels is represented using Equation 5.16 which is a combination of Equation 5.6 and the decomposition of nitric acid in the presence of NO.³⁷ Formation of dinitrosyl complexes, which likely compete with immobile AgNO₃ in the main channels, on Fe ions in the mordenite is represented by Equation 5.17.



The gas concentration of NO was held constant for the aging simulations shown in Figure 5.6. Initially, simulations were performed with variable NO concentration but there was not a significant decrease in the concentration over the simulation's run time. Thus, the simulation run time can be notably reduced by holding the concentration constant without affecting the simulation results. In two instances, adjusting the rate constant was not sufficient to achieve a reasonable fit of the data. To account for this, the reaction order was adjusted accordingly for one species per irreversible reaction. The reaction orders for all species in every reversible reaction were determined by stoichiometry. Slight variations are, once again, observed between simulated and experimental results due to slight variations in Ag⁰Z's properties between each sample. These are not notably more or less significant than the variations already observed in NO₂.

With respect to I₂ adsorption on Ag₂O and AgNO₃, the contributions to the material's adsorption capacity are easy to determine. All Ag₂O and all AgNO₃ not

clustered in the main channel will be replaced by AgI upon exposure to I_2 . Adsorption on Ag^0Z can be estimated using the last reaction given in Table 5.2 by fitting to the experimental data previously collected by Nan and coworkers.¹⁵ Thus, as an example, after one week aging in 1% NO, the simulated AgI from Ag_2O , $AgNO_3$, and Ag^0Z is 1.0%, 16.3%, and 14.1% of total Ag, respectively. These results are in line with the experimental results where AgI from Ag_2O , $AgNO_3$, and Ag^0Z account for 3%, 16.5%, and 15.8% of total Ag, respectively. Predicting α -phase adsorption on AgZ is, however, not possible with the information currently available.

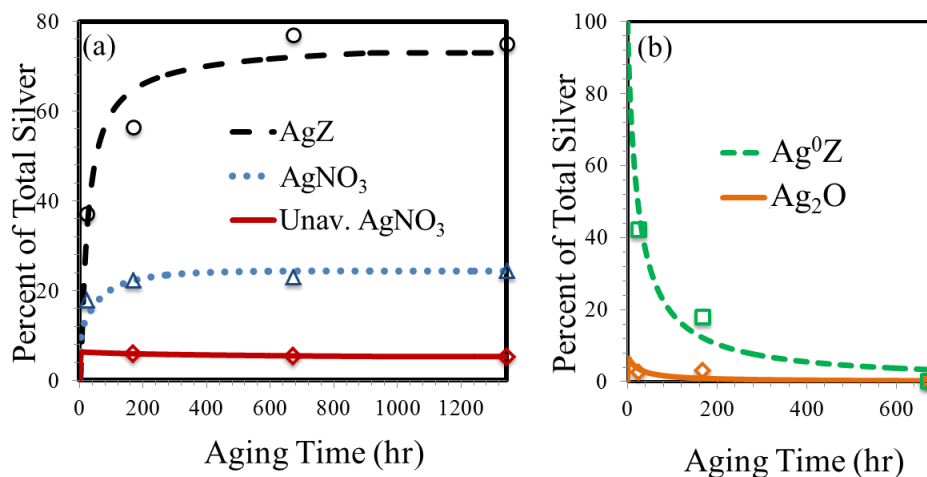


Figure 5.6. Simulation results compared against XAS combination fitting data for aging at 150°C in 1% NO in N₂ and aging times up to two months.

Based on a previous analysis, unreduced AgZ has an I_2 capacity of 2.6 w.t. % at 150°C for an unaged adsorbent with a Ag content of 9.5 w.t. %.¹¹ As such, α -phase iodine adsorption will yield a Ag utilization rate on main channel binding sites of about 27% if the channels are unobstructed. Thus, when we consider that ~25% of Ag in our material is not in the main channels, the overall utilization rate for α -phase adsorption should drop

to about 20% of the total Ag in the system. At 12 min aging in 2% NO₂, α -phase adsorption accounts for 19.6% of total Ag suggesting that the channels are not yet obstructed. By one hr, however, α -phase AgI only accounts for ~1% of total Ag where it remains for the remaining aging times. This does not give sufficient information to determine a relationship between AgNO₃ accumulating in the main channels, which is already well underway after 12 min in NO₂, and site access.

Table 5.2. Forward and reverse reaction rate constants for all reactions used in aging simulations for 1% NO in N₂ and 2% NO₂ in dry air at 150°C and the reaction for I₂ adsorption on Ag⁰. Reaction orders determined by stoichiometry unless otherwise noted.

Reaction	Rate Constants		Notes
	Forward	Reverse	N/A
$2\text{Ag}^0 + \text{O}_2 + 2\text{NO}_2 \rightarrow 2\text{AgNO}_3$	2.3e10	0.0	N/A
$\text{Na}_{(\text{ads})} + 2\text{Ag}^0 + \text{NO} \rightarrow \text{Ag}_2\text{O} + \text{Na}_{(\text{ads})}$	0.2	0.0	4 th w.r.t Ag ⁰
$\text{Ag}_2\text{O} + 2\text{NO} \rightarrow \text{Ag}^0 + \text{AgNO}_3 + 0.5\text{N}_2$	15.0	0.0	N/A
$4\text{HZ} + 4\text{AgNO}_3 \rightarrow 4\text{AgZ} + 4\text{NO}_2 + 2\text{H}_2\text{O} + \text{O}_2$	1.0e10	0.0	N/A
$2\text{HZ} + 2\text{AgNO}_3 + \text{NO} \rightarrow 2\text{AgZ} + \text{H}_2\text{O} + 2\text{NO}_2$	10.0	0.0	4 th w.r.t HZ
$\text{AgNO}_3 + \theta \leftrightarrow \text{AgNO}_3^{\text{cluster}}$	26.5	0.3	N/A
$\text{Fe}(\text{Z})_2 + 2\theta + 2\text{NO} \leftrightarrow \text{Fe}(\text{Z})_2(\text{NO})_2$	1.25e-4	12.75	N/A
$2\text{Ag}^0 + \text{I}_2 \leftrightarrow 2\text{AgI}$	16870	5.75e-4	N/A

5.4 Conclusions

Ag⁰Zs are promising materials for iodine capture from nuclear fuel reprocessing off-gas. These materials are effective iodine adsorbents with ~87% of Ag⁰ in the mordenite used for adsorption. Despite their high iodine capacity, the behavior of Ag mordenites under real off-gas conditions is not well understood. One area of interest is material aging where the adsorbent loses iodine capacity over time from exposure to O₂, H₂O, NO, and NO₂. While the overall effect of aging is known, the underlying processes that explain this loss of capacity have not been explored. To examine these processes,

adsorbed samples were aged in gas streams of 2% NO₂ in dry air and 1% NO in N₂ at 150°C for periods of up to six months. Aging leads to a significant decline in I₂ capacity (up to 97%) in both environments, though the rate of capacity loss is significantly faster in 2% NO₂. This loss of capacity is brought about by a number of different physical and chemical processes. First, the Ag⁰ is oxidized to Ag₂O through dissociative adsorption of NO in 1% NO or O₂ in 2% NO₂. Then, adsorption of NO or NO₂ leads to the formation of AgNO₃ which will migrate off of the Ag⁰ particle, first onto the mordenite surface and then into the interior channels. Once inside the channels of the mordenite, AgNO₃ will exchange at protonated binding sites in the main channels forming nitric acid. Only about 75% of Ag is originally located in the main channels before reduction, leaving a permeate presence of AgNO₃ in the mordenite.

Even in the absence of Ag⁰, I₂ will adsorb on Ag₂O, AgNO₃, and unreduced Ag. All Ag₂O is available for adsorption; however, some AgNO₃ in the system will congregate in the main channels forming a phase unavailable for I₂ adsorption. This unavailable AgNO₃ phase will also block the mordenite channels preventing I₂ from accessing main channel Ag binding sites. These sites, if unobstructed, would adsorb I₂ in the α-phase. As a result, samples aged for long periods in both 2% NO₂ and 1% NO almost exclusively adsorb I₂ on AgNO₃. In 1% NO, Fe impurities form dinitrosyl and trinitrosyl complexes in the main channels that compete with the unavailable AgNO₃ phase for space and also block channel access. Based on these processes, aging was simulated and compared against experimental data attaining reasonable approximations. I₂ adsorption was also considered, though adsorption in the α-phase could not be modeled with the available data.

5.5 Acknowledgments

The development of this chapter was a collaborative effort among my co-authors and myself and was the main subject of the following manuscript: A. Wiechert, A. Ladshaw, J. Moon, C.W. Abney, Y. Nan, S. Choi, J. Liu, L.T. Tavlarides, C. Tsouris, S. Yiacoumi. Capture of Iodine from Nuclear-Fuel-Reprocessing Off-Gas: Influence of Aging on Reduced Silver Mordenite Adsorbent after Exposure to NO/NO₂. Submitted to ACS Applied Materials and Interfaces December 2019.

5.6 References

- 1) Haefner, D and Tranter, T. Methods of Gas Phase Capture of Iodine from Fuel Reprocessing Off-Gas: A Literature Survey. INL/EXT-07-12299. Idaho National Laboratory, Idaho Falls, ID 2007.
- 2) Zhao, H. Y.; Nenoff, T. M.; Jennings, G.; Chupas, P. J.; Chapman, K. W., Determining Quantitative Kinetics and the Structural Mechanism for Particle Growth in Porous Templates. *J Phys Chem Lett* 2011, 2 (21), 2742-2746.
- 3) Chapman, K. W.; Chupas, P. J.; Nenoff, T. M., Radioactive iodine capture in silver-containing mordenites through nanoscale silver iodide formation. *J Am Chem Soc* 2010, 132 (26), 8897-9.
- 4) Nenoff, T. M.; Rodriguez, M. A.; Soelberg, N. R.; Chapman, K. W., Silver-mordenite for radiologic gas capture from complex streams: Dual catalytic CH₃I decomposition and I confinement. *Microporous and Mesoporous Materials* 2014, 200, 297-303.
- 5) Azambre, B.; Chebbi, M. Evaluation of Silver Zeolites Sorbents Towards their Ability to Promote Stable CH₃I Storage as AgI Precipitates. *ACS Applied Materials & Interfaces* 2017, 9, 25194-25203.
- 6) Chibani, S.; Chebbi, M.; Lebegue, S.; Cantrel, L.; Badawi, M. Impact of the Si/Al ratio on the selective capture of iodine compounds in silver-mordenite: a periodic DFT study. *Phys. Chem. Chem. Phys.* 2016, 18, 25574-25581.

- 7) Bucko, T.; Chibani, S.; Paul, J.-F.; Cantrel, L.; Badawi, M. Dissociative iodomethane adsorption on Ag-MOR and the formation of AgI clusters: an ab initio molecular dynamics study. *Phys. Chem. Chem. Phys.* 2017, 19, 27530-27543.
- 8) Jabraoui, H.; Hessou, E.P.; Chibani, S.; Cantrel, L.; Lebegue, S. Badawi, M. Adsorption of volatile organic and iodine compounds over silver-exchanged mordenites: A comparative periodic DFT study for several silver loadings. *App. Surf. Sci.* 2019, 485, 56-63.
- 9) Abney, C. W.; Nan, Y.; Tavlarides, L. L., X-ray Absorption Spectroscopy Investigation of Iodine Capture by Silver-Exchanged Mordenite. *Industrial & Engineering Chemistry Research* 2017, 56 (16), 4837-4846.
- 10) Jubin, R. T.; Ramey, D. W.; Spencer, B. B.; Anderson, K. K.; Robinson, S. M. In Impact of Pretreatment and Aging on the Iodine Capture Performance of Silver-Exchanged Mordenite WM2012 Conference, Phoenix, AZ (United States), Phoenix, AZ (United States), 2012.
- 11) Patton, K. K.; Bruffey, S. H.; Jubin, R. T.; Walker, J. F. Effects of Extended In-Process Aging of Silver-Exchanged Mordenite on Iodine Capture Performance, 33rd Nuclear Air Cleaning Conference, St Louis, MO (United States), St Louis, MO (United States), 2014.
- 12) Patton, K. K.; Bruffey, S. H.; Jubin, J. T.; Walker, J. F. Iodine Loading of NO Aged Silver Exchanged Mordenite; Oak Ridge National Laboratory (ORNL): Oak Ridge, TN (United States), 2014.
- 13) Bruffey, S.; Jubin, R. Initial Evaluation of Effects of NO_x on Iodine and Methyl Iodide Loading of AgZ and Aerogels; ORNL/SPR-2015/125; Oak Ridge National Laboratory (ORNL): Oak Ridge, TN (United States), 2015; p 125.
- 14) Bruffey, S.; Patton, K.; Walker Jr, J.; Jubin, R. Complete NO and NO₂ Aging Study for AgZ; ORNL/SPR-2015/128; Oak Ridge National Laboratory (ORNL): Oak Ridge, TN (United States), 2015; p 128.
- 15) Ladshaw, A.; Wiechert, A.; Welty, A.; Lyon, K.; Law, J.; Jubin, R.; Tsouris, C.; Yiacoymi, S. Adsorbents and adsorption models for capture of Kr and Xe gas mixtures in fixed-bed columns. *Chemical Engineering Journal* 2019, 375, 122073.
- 16) Nan, Y.; Tavlarides, L. L.; DePaoli, D. W., Adsorption of iodine on hydrogen-reduced silver-exchanged mordenite: Experiments and modeling. *AIChE Journal* 2017, 63 (3), 1024–1035.

- 17) Kropf, A. J.; Katsoudas, J.; Chattopadhyay, S.; Shibata, T.; Lang, E. A.; Zyryanov, V. N.; Ravel, B.; McIvor, K.; Kemner, K. M.; Scheckel, K. G.; Bare, S. R.; Terry, J.; Kelly, S. D.; Bunker, B. A.; Segre, C. U., The New MRCAT (Sector 10) Bending Magnet Beamline at the Advanced Photon Source. AIP Conference Proceedings 2010, 1234 (1), 299-302.
- 18) Ravel, B.; Newville, M., ATHENA, ARTEMIS, HEPHAESTUS: data analysis for X-ray absorption spectroscopy using IFEFFIT. Journal of Synchrotron Radiation 2005, 12 (4), 537-541.
- 19) Gaston, D.; Newman, C.; Hansen, G.; Lebrun-Grandié, D. MOOSE: A parallel computational framework for coupled systems of nonlinear equations, Nuc. Eng. Design, 239, 1768-1778, 2009.
- 20) Campble, C.T. ATOMIC AND MOLECULAR OXYGEN ADSORPTION ON Ag(111). Surface Science, 1985, 157, 43-60.
- 21) Bukhtiyarov, V.I.; Kaichev, V.V.; Prosvirin, I.P. Oxygen adsorption on Ag(111): X-ray photoelectron spectroscopy (XPS), angular dependent x-ray photoelectron spectroscopy (ADXPS) and temperature-programmed desorption (TPD) studies. Journal of Chemical Physics 1999, 111, 2169.
- 22) Backx, C.; De Groot, C.P.M.; Biloen, P. Adsorption of Oxygen on Ag(110) studied by High Resolution ELS and TPD. Surface Science 1981, 104, 300-317.
- 23) Zemlyanov, D.Y.; Hornung, A.; Weinberg, G.; Wild, U.; Schlogl, R. Interaction of Silver with a NO/O₂ Mixture: A Combined X-ray Photoelectron Spectroscopy and Scanning Electron Microscopy Study. Langmuir, 1998, 14, 3242-3248.
- 24) Huve, J.; Ryzhikov, A.; Nouali, H.; Lalia, V.; Auge, G.; Daou, T.J. Porous sorbents for the capture of radioactive iodine compounds: a review. RSC Adv. 2018, 8, 29248.
- 25) Chapman, K. W.; Chupas, P. J.; Kepert, C. J., Selective Recovery of Dynamic Guest Structure in a Nanoporous Prussian Blue through in Situ X-ray Diffraction: A Differential Pair Distribution Function Analysis. Journal of the American Chemical Society 2005, 127 (32), 11232-11233.
- 26) Martucci, A.; Cruciani, G.; Alberti, A.; Ritter, C.; Ciambelli, P.; Rapacciuolo. Location of Bronsted sites in D-mordenites by neutron powder diffraction. Microporous and Mesoporous Materials 2000, 35-36, 405-412.
- 27) Alberti, A.; Location of Bronsted sites in mordenite. Zeolites 1997, 19, 411-415.
- 28) Marbrow, R.A.; Lambert, R.M. Chemisorption and Surface Reactivity of Nitric Oxide on Clean and Sodium-dosed Ag(110). Surface Science 1976, 61, 317-328.

- 29) Goddard, P.J.; West, J.; Lambert, R.M. Adsorption, Coadsorption, and Reactivity of Sodium and Nitric Oxide on Ag(111). *Surface Science* 1978, 71, 447-461.
- 30) Carley, A.F.; Davies, P.R.; Roberts, M.W.; Santra, A.K.; Thomas, K.K. Coadsorption of carbon monoxide and nitric oxide at Ag(111): evidence for a CO-NO surface complex. *Surface Science* 1998, 406, L587-L591.
- 31) Bao, X.; Wild, U.; Muhler, M.; Pettinger, B.; Schlogl, R.; Ertl, G. Co-adsorption of nitric oxide and oxygen on the Ag(110) surface. *Surface Science*, 1999, 425, 224-232.
- 32) Zemlyanov, D.; Schlogl, R. Effect of oxygen on NO adsorption on the Ag(111) surface: evidence for a NO₃ ads species. *Surface Science* 2000, 470, L20-L24.
- 33) Lobree, L.; Hwang, I.-C.; Reimer, J.; Bell, A. Investigation of the State of Fe in H-ZSM-5. *Journal of Catalysis* 1999, 186, 242-253.
- 34) Mihaylov, M.; Ivanova, E.; Drenchev, N.; Hadjivanov, K. Coordination Chemistry of Fe²⁺ Ions in Fe, H-ZSM-5 Zeolite as Revealed by the IR Spectra of Adsorbed CO and NO. *J. Phys. Chem. C* 2010, 114, 1004-1014.
- 35) Segawa, K.-I.; Chen, Y.; Kubsh, J.; Delgass, W.N.; Dumesic, J.A.; Hall, W. Infrared and Mossbauer Spectroscopic Studies of the Interaction of Nitric Oxide with Fe-Y Zeolite. *Journal of Catalysis* 1982, 76, 112-132.
- 36) Thiemann, M.; Scheibler, E.; Wiegand, K.W. Nitric Acid, Nitrous Acid, and Nitrogen Oxides. *Ullmann's Encyclopedia of Industrial Chemistry*, 2000.
- 37) McKinnon, I.R.; Mathieson, J.G.; Wilson, I.R. Gas Phase Reaction of Nitric Oxide with Nitric Acid. *Journal of Physical Chemistry* 1979, 83, 779-780.

5.7 Nomenclature

XAS – X-ray Absorption Spectroscopy

XANES – X-ray Absorption Near Edge Structure

PJFNK – Preconditioned Jacobi Free Newton Krylov

HZ – Protonated mordenite binding sites

θ – Mordenite binding sites available for cluster formation

C – Gas phase concentration

ε – Bulk bed porosity

D – Dispersion

T – Temperature

t – Time

q – Adsorbed capacity

ρ_b – Adsorbent packing density

k_f – Forward reaction rate constant

k_r – Reverse reaction rate constant

ν – Stoichiometric coefficient

ν^* – Reaction order coefficient

h_g – Specific heat of gas phase species

h_s – Specific heat of adsorbents

ρ – Gas density

K – Thermal Conductivity

Q_{st} – Isothermic heat of adsorption

j – Index of reactants

k – Index of Products

i – Index of Adsorbents

CHAPTER 6: Aging Effect in Silver Aerogel

6.1 Introduction

Reduced silver mordenite (Ag^0Z) has traditionally been considered the most promising material for radioiodine capture, however, in recent years a growing emphasis has been placed on the development of potential alternative adsorbents.^{1,2} Among the most prominent of these alternatives are silver (Ag) functionalized aerogels. The growing prominence of this type of Ag adsorbents can be attributed to their high Ag content which is well above that of Ag^0Z leading to a proportionally higher iodine capacity.³ Nevertheless, the behavior of these materials in real reprocessing off-gas has not yet been studied in depth. As previously observed in Ag^0Z , off-gas constituents such as nitric oxide (NO) and nitrogen dioxide (NO_2) can, under appropriate conditions, interact with the adsorbent leading to significant and in some cases rapid degradation in iodine capacity.⁴ This process is known as aging and while efforts have been made to understand the causes of aging in Ag^0Z no such comparable effort has been undertaken for Ag functionalized aerogels. Thus the purpose of this study is to quantify the effects of aerogel aging while simultaneously delving into the potential process that produce the observed effects. Additionally, the aerogel aging will be compared to aging in Ag^0Z and the reasons for any disparity between these two materials will be explored. This will be achieved primarily through analysis of the inorganic iodine (I_2) capacity of samples aged in dry air, humid air, and 1% NO in nitrogen (N_2) for up to one month. A more in depth analysis of dry air aging will be conducted by characterizing aged samples with X-ray Adsorption Spectroscopy (XAS) to determine Ag speciation over time. Finally, from this

discussion a predictive model for reduced silver (Ag^0) aerogel aging is developed within the Discontinuous Galerkin Off-gas Separation and Recovery (DG-OSPNEY) modeling framework.

6.2 Methodology

6.2.1 Materials

The Ag functionalized aerogel used in this study was synthesized at Pacific Northwest National Laboratory (PNNL) using a procedure that was previously developed.³ Samples were synthesized from commercial available granular silica aerogel purchased from United Nuclear in Laingsburg, MI. The as received aerogel is already functionalized with trimethylsilyl groups by the manufacturer to increase the hydrophobicity of the aerogel. These groups are removed through heat treatment of the aerogel granules for one hr at 400°C. After heat treatment, the aerogel is hydrated in humid air with a relative humidity of 100% at room temperature for approximately 12 hr. Hydrated granules were then functionalized with 1-propanethiol by treating the aerogel with 3-(mercaptopropyl) trimethoxysilane (95% Pure 3-MPTMS from Sigma Aldrich) in super critical carbon dioxide (24 MPa) at 150°C for 24 hr. Following thiol functionalization, aerogel granules were submerged in a solution containing 3.4% by mass AgNO_3 and 16.7% by volume methanol to replace protons in the thiol groups with Ag (I) ions (i.e., from the typical S-H to S-Ag). Samples were then reduced in a 4% hydrogen (H_2) in Argon gas stream with a flow rate of 500 mL/min at 400°C for 24 hr. All gases, with the exception of I_2 , used in aging, reduction, and iodine loading were purchased from Airgas Inc. with an Ultra Zero Grade for dry air and Certified Standard

Grade for all others. I₂ vapor was instead supplied from a pair of dynacalibrators (VICI Models 450 and 500) to produce a gas mixture with dry air containing a concentration of 50 ppm by volume I₂.

6.2.2 *Experimental Methodology*

Aerogel samples were aged in dry air, humid air (dew point of -15°C), and 1% NO in N₂ at 150°C for various periods of time with largely the same procedures as described in our previous study.⁴ Glass columns (2.5 cm by 7.0 cm) divided into four equally sized chambers were loaded with approximately one g of Ag⁰ aerogel per chamber. For each aging environment, a dedicated gas line was prepared and supplied with a constant flow (500 mL/min) of the desired gas mixture at a constant 150°C which was maintained using two Thermo Scientific Heratherm ovens. The flow of gas through the system was controlled using a Cole-Parmer gas mass flow controller (Item #EW-32907) while the temperature of the gas stream was tracked using thermal monitors located at the inlet of each aging column. After a certain period of time, the sample was removed from the aging system and then either underwent I₂ adsorption or was stored in pure Argon. For I₂ adsorption, the aged aerogel sample was exposed to a dry air gas stream with an I₂ concentration of 50 ppm by volume at 150°C. The system used for adsorption in this study is identical to the one used in our analysis of Ag⁰Z aging described previously.⁴

XAS experiments were performed on aerogel samples aged in dry air for one month, two months, four months, and six months to determine the speciation of Ag over time. These experiments were performed at Argonne National Laboratory's Advanced

Photon Source with beamline 10-ID-B⁵ with procedures identical to the ones described previously for the analysis of Ag⁰Z aging.⁴ Linear combination fitting on normalized $\mu(E)$ spectra from 30 eV below to 100 eV above the Ag k-edge (25514 eV) was performed with reference standards for unaged Ag⁰ functionalized aerogel, silver sulfide (Ag₂S), and silver sulfate (Ag₂SO₄). From these spectra, the approximate spectra of the X-ray Absorption Near Edge Structure (XANES) spectra are simulated and optimized against the experimentally obtained spectra based on the R-factor and reduced χ^2 fit parameters. The fit that most closely approximates the experimental spectra was determined by minimizing these parameters. Best fit results for each XANES spectra are given in Appendix B.

6.2.3 Modeling Methodology

The DG-OSPNEY model, which is developed at the Georgia Institute of Technology, is used for all simulations of adsorbent aging.⁶ Built within the MOOSE⁷ modeling framework, DG-OSPNEY defines the mass and energy conservation equations needed for adsorption modeling and directs MOOSE to carry out spatial discretization of the domain using Discontinuous Galerkin (DG) methods. Discretization is performed with DG methods as they are less prone to oscillation than continuous methods for simulation of problems derived from conservation laws. In addition to spatial discretization, MOOSE is responsible for iteratively solving the system of equations provided to it by DG-OSPNEY. Iteration of this non-linear system of equations is performed using the Jacobi-Free-Newton Krylov method which combines a Newton type non-linear solver with a nested linear iterator based on Krylov subspace methods. The

linear iteration method generally used is the Generalized Minimal Residual method and is preconditioned with incomplete lower and upper triangular fractionalization.

Convergence of non-linear iterations is controlled through the use of line search methods.

A more complete description of DG-OSPNEY can be found in our investigation of Ag^0Z aging⁴ or in the works of Ladshaw and coworkers.⁶

6.3 Results and Discussion

6.3.1 Aging and XAS Experiments

The adsorption capacities of aerogel samples aged in dry air, humid air, and 1% NO in N_2 are summarized in Table 6.1. After one month, the capacity loss for all three aging environments is quite similar with 1% NO losing slightly more than in either dry or humid air (23% loss versus 20% and 18%, respectively). This is true across all aging times indicating that all three aging environments have essentially the same rate of adsorbent aging with some variations that can be attributed to material non-uniformity. When comparing Ag^0 aerogel to Ag^0Z we can see the aging effect is much less pronounced across all three environments. In humid air, aging Ag^0Z for one month results in a 40% loss of adsorption capacity compared to only 18% observed in the aerogel.⁸ For 1% NO in N_2 the one month capacity loss from aging was 88.6% in Ag^0Z while for the same aging time the capacity of Ag^0 aerogel declined by only 23%.⁴ Lastly, for dry air aging the Ag^0Z I_2 capacity dropped by 35% after one month compared to 23% for the aerogel which, while less than the disparities in humid air and 1% NO, is still quite significant.⁹ It is postulated that there are two primary reasons for this apparent resistant to aging found in the aerogel.

The first reason is that the Ag surface is not reactive to either NO or water vapor (H₂O) at the experimental temperature of 150°C. In fact the surface becomes unreactive to NO above 25°C¹⁰ while the surface remains reactive up to about 50°C¹¹ for H₂O. In the case of Ag⁰Z, the adsorbent can interact with these two gases far above these temperatures because the adsorption of NO and H₂O are catalyzed by metal impurities found in the mordenite.^{12,13} Thus, since no metal impurities exist in the aerogel we would expect to see significantly less aging in the 1% NO and humid air aging environments. In the 1% NO environment, however, this leaves no potential gas phase species that can react with the Ag surface to produce the observed aging effect. This, paradoxically, can be explained as part of the second major reason proposed as to why the aerogel is less susceptible to aging than Ag⁰Z.

Table 6.1. I₂ capacity as a percentage of initial weight gained after exposure to 50 ppmv I₂ in dry air at 150°C for Ag⁰ functionalized aerogel aged with an unaged capacity of 36.4 w.t. % in dry air (dew point of -70°C), humid air (dew point of -15°C), and 1% NO in N₂ gas streams.

Aging Time	I ₂ Capacity (w.t. %)		
	Dry Air	Humid Air	1% NO in N ₂
3 days	35.4	35.4	33.8
1 week	34.2	34.8	32.3
2 weeks	32.4	31.1	29.6
1 month	29.2	29.8	28.1

While the aerogel contains no metal impurities, the chemistry of the thiol functional groups is important to understanding the aging behaviors observed. Specifically, the thiol groups adsorb to the surface of the Ag⁰ nanoparticles that are responsible for the vast majority of I₂ adsorption. Thiols, generic form r-S-H where r is

an alkyl such as CH₃-CH₂-CH₂ in the case of propanethiol, can adsorb onto Ag⁰ surfaces through cleavage of the S-H bond yielding an adsorbed thiolate species by the reaction given in Equation 6.1.¹⁴⁻¹⁶ As a result of this reaction, the surface of the Ag⁰ nanoparticle will be covered in a thiol monolayer. This layer acts as a protective coating reducing the reactivity of the nanoparticle's surface while also increasing its stability.¹⁷⁻¹⁹ It is this property of thiol binding that serves as the other major component of the aerogel's aging resistance. Nevertheless, thiol binding can contribute to aging under the right circumstances. At irregular surface sites, for example, the r-S bond may be cleaved resulting in the formation of Ag₂S.¹⁵ From here the Ag₂S will dissociate from the Ag⁰ nanoparticle and begin to form Ag₂S nanoparticles.²⁰ This process can be represented by the overall reaction given in Equation 6.2. As such, the aging we see in the 1% NO environment is probably a result of dissociation of adsorbed thiol groups since this process does not involve any interactions with any gas phase species.



Ag⁰ aerogels aged in dry air for one month, two months, four months, and six months were characterized using XAS through analysis of the XANES spectra. XANES for unaged Ag⁰ aerogel, Ag₂S, Ag₂SO₄, and four aerogel samples aged in dry air for one month, two months, four months, and six months are given in Figure 6.1. In this case, the aged aerogel spectra were very similar to the unaged sample which is not particularly surprising given the overall aging effect on I₂ capacity. Thus at all times we would expect to see most of the Ag remain in a form similar to the unaged aerogel. The standards previously discussed were used to perform linear combination fitting to determine Ag

speciation with the best fit for each spectrum shown in Appendix B (Figure B6). From this fitting the breakdown of Ag species as a percent of total Ag is derived for the dry air aged samples (Figure 6.2).

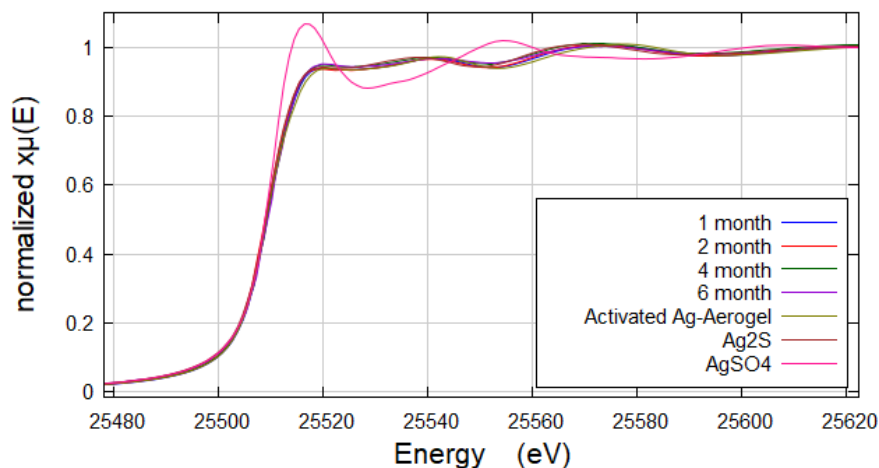


Figure 6.1. Normalized Ag K-edge XANES of Ag Aerogel aged in dry air at 150°C for one month, two months, four months, and six months.

After one month of aging in dry air, about 83% of all Ag is still in a form similar to Ag in the unaged aerogel. Considering the 20% I₂ capacity reduction observed after one month aging, we can reasonably assume that adsorption of I₂ can be explicitly tied to the proportion of Ag in the activated state with all other species playing no role in I₂ adsorption. At the same time, the remaining Ag is divided between Ag₂S (~13% of total Ag) and Ag₂SO₄ (~4% of total Ag). The proportion of Ag in the form of Ag₂S (15.3%) and Ag₂SO₄ (6%) continues to rise up to a dry air aging time of two months. Ag₂S continues to rise as aging progresses with 23.4% and 23.6% of all Ag in the form of Ag₂S after four and six months, respectively. Ag₂SO₄, on the other hand, almost disappears when the sample is aged for four months and makes up only about 3% of all Ag after six

months aging. This can partially be attributed to material heterogeneity though another aspect of this is that the processes that produce Ag_2SO_4 likely reach an effective aging equilibrium. As such, even if the samples were aged for a much longer period of time, we would not expect to see a significantly greater amount of Ag_2SO_4 . There are two important steps to the formation of Ag_2SO_4 : (i) oxidation of sulfur from sulfide to sulfate and (ii) cleavage of the propane alkyl from the surface bound sulfur. When these two steps happen in relation to one another, however, is not known with certainty. Bond cleavage could, for example, proceed before sulfur oxidation forming Ag_2S which is then oxidized into Ag_2SO_4 . Thus we will need to consider the possibility of cleavage occurring before, during, or after sulfur oxidation from sulfide to sulfate.

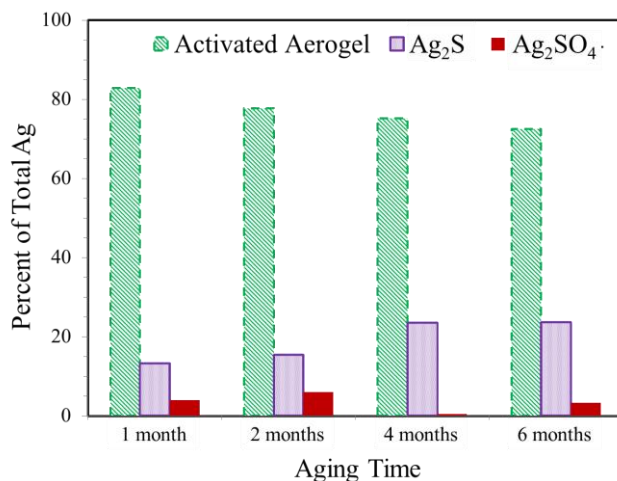


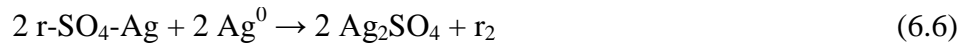
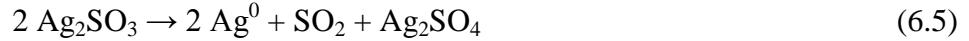
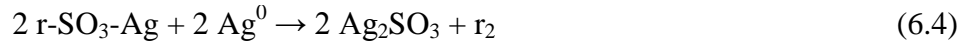
Figure 6.2. The portion of each Ag species present in 150°C dry air aged Ag aerogel samples as a percent of total Ag determined from linear combination fitting of XANES data.

The first of these possibilities, cleavage before oxidation, is unlikely for two main reasons. First, as already discussed, Ag_2S tends to dissociate from the Ag nanoparticle

forming separate Ag₂S nanoparticles. These Ag₂S nanoparticles are unreactive towards oxygen (O₂) at our experimental temperature and, therefore, should not be oxidized to Ag₂SO₄ under the conditions being examined.²¹ Oxidation of Ag₂S could proceed on the Ag nanoparticle's surface, however, this would result in the formation of silver hyposulfite (Ag₂SO₂) as an intermediate species. The formation of this species is problematic because it will dissociate into Ag⁰ and gaseous sulfur dioxide (SO₂) at temperatures above about 25°C.²² Thus, we can assume that, for the formation of Ag₂SO₄, cleavage must occur either during oxidation or after sulfur oxidation is complete.

The oxidation of surface bound thiols can proceed by a reaction with atomic oxygen forming Ag sulfenate given in Equation 6.3.²³ Atomic oxygen can originate from within the Ag nanoparticle as a result of subsurface O₂ adsorption.²⁴⁻²⁶ Sulfur oxidation likely then proceeds by a series of reactions similar to Equation 6.3 where Ag sulfenate is oxidized to Ag sulfinite (r-SO₂-Ag) which is then oxidized to Ag sulfonate (r-SO₃-Ag) and then potentially to Ag propyl sulfate (r-SO₄-Ag). For Ag₂SO₄ to ultimately form, alkyl cleavage must occur after oxidation to Ag sulfonate to avoid the potential formation of Ag₂SO₂ as an intermediate species. As such, there are two potential routes that the reaction can proceed down. The first has alkyl cleavage happen after oxidation to Ag sulfonate (Equation 6.4) followed by dissociation of the resulting Ag₂SO₃ to Ag₂SO₄, SO₂, and Ag⁰ (Equation 6.5)²⁷ while the other occurs after oxidation is complete directly forming Ag₂SO₄ (Equation 6.6). Based on the available experimental information, it is not possible to discern which of these two pathways is predominant.





6.3.2 Aging Modeling

For simulation of aerogel aging, the proportion of Ag in the form of unaged aerogel (i.e., activated aerogel) was treated as Ag^0 and it was also assumed that alkyl cleavage occurring after complete sulfur oxidation dominates. Additionally, since the concentration of atomic oxygen originating from the interior of the Ag nanoparticle is unknown it was assumed to be a constant function of the O_2 concentration. Equation 6.7, which is used to represent Ag_2S formation, is a combination of Equations 6.1 and 6.2 with a forward rate of $1.85 \times 10^{-8} (\text{kg/mol})^7$ and is treated as a 6th order reaction with respect to Ag^0 . The reaction order was changed in this case because a good agreement with experimental results could not be obtained by adjusting just the forward rate constant. Based on the previous discussion, Equation 6.8 is used as the net reaction for Ag_2SO_4 formation with a forward rate of $44 (\text{kg/mol})^3 (\text{L/mol})^4$. Results of this aging simulation are shown in Figure 6.3. For three days, one week, and two weeks aging the percentage of total Ag in the active form is estimated from the I_2 loading experiments and is based on the Ag utilization rate typically observed for the Ag aerogel. Simulated results match up well to experimental findings until two month aging. After this point, the proportion of Ag in the form of Ag_2SO_4 is overestimated leading to a lower than expected concentration of activated Ag. This can at least partially be attributed to how the model handles atomic oxygen. In practice atomic oxygen should be a function of Ag in the

reduced state, however, since the amount of Ag^0 is not precisely known this cannot be properly considered.

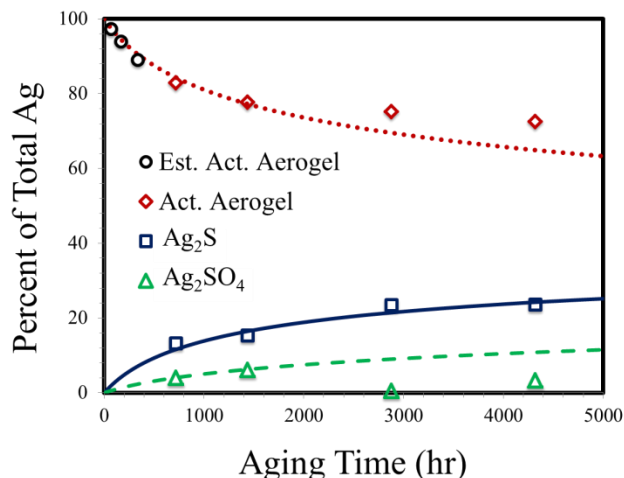
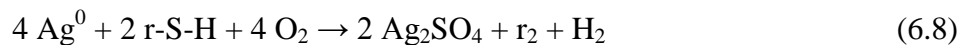
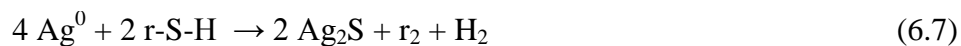


Figure 6.3. Simulation results compared against XAS combination fitting data (one, two, four, and six months) and activated aerogel estimate from I_2 loading experiments (three days, one week, and two weeks) on aerogel aged in dry air at 150°C .

6.4 Conclusions

The aging of Ag^0 functionalized silica aerogels was investigated for dry air, humid air, and 1% NO in N_2 gas streams. Aging of the aerogel was significantly less than the aging effect previously observed in Ag^0Z . This can be attributed to two primary factors: (i) the Ag^0 nanoparticles are unreactive to NO and H_2O at the experimental temperature and have no metal ion impurities to catalyze their adsorption as is the case in Ag^0Z and (ii) the adsorption of thiol functional groups onto the nanoparticles creates a protective layer that reduces the reactivity of the nanoparticle's surface. The effect of

aging in all three aging environments was roughly the same with an approximate reduction of 20% in I_2 capacity after one month. XAS analysis of dry air aged aerogel revealed that the two byproducts of aging were Ag_2S and Ag_2SO_4 . Ag_2S is formed through cleavage of the r-S bond when thiols adsorb on irregular surface sites thus releasing the propane alkyl. In the case of Ag_2SO_4 , the adsorbed thiols undergo oxidation by reacting with atomic oxygen originating from the nanoparticle interior and then experience cleavage of the alkyl group. Based on this analysis, aging simulations were performed and good agreement was obtained up to two months aging in dry air. After this point, Ag_2SO_4 was overestimated because the effective equilibrium observed for Ag_2SO_4 experimentally and the concentration of atomic oxygen in the nanoparticle subsurface could not be properly represented.

6.5 Acknowledgments

The development of this chapter was a collaborative effort among my co-authors and myself and will serve as a significant component of a manuscript that is currently being prepared with the following coauthors: A. Wiechert, A. Ladshaw, J. Moon, C.W. Abney, Y. Nan, S. Choi, J. Liu, L.T. Tavlarides, C. Tsouris, S. Yiacoumi. In the process of being developed as of November 2019.

6.6 References

- 1) Riley, R.; Vienna, J.; Strachan, D.; McCloy, J.; Jerden, J. Material and processes for the effective capture and immobilization of radioiodine: A review. *Journal of Nuclear Materials* 2016, 470, 307-326.

- 2) Huve, J.; Ryzhikov, A.; Nouali, H.; Lalia, V.; Auge, G.; Daou, T.J. Porous sorbents for the capture of radioactive iodine compounds: a review. *RSC Adv.* **2018**, *8*, 29248.
- 3) Matyas, J.; Ilton, E.S.; Kovatik, L. Silver-functionalized silica aerogel: towards an understanding of aging in iodine sorption performance. *RCS Adv.* **2018**, *8*, 31843.
- 4) Wiechert, A.; Ladshaw, A.; Moon, J.; Abney, C.W.; Nan, Y.; Choi, S.; Liu, J.; Tavlarides, L.T.; Tsouris, C.; Yiacoumi, S. Investigation of the Aging Effect of Reduced Silver Mordenite from Exposure to NO and NO₂ on the Capture of Iodine from Off-Gas Generated in Spent Nuclear Fuel Reprocessing. Submitted to *ACS Applied Materials and Interfaces* on November 15th 2019
- 5) Kropf, A. J.; Katsoudas, J.; Chattopadhyay, S.; Shibata, T.; Lang, E. A.; Zyryanov, V. N.; Ravel, B.; McIvor, K.; Kemner, K. M.; Scheckel, K. G.; Bare, S. R.; Terry, J.; Kelly, S. D.; Bunker, B. A.; Segre, C. U., The New MRCAT (Sector 10) Bending Magnet Beamline at the Advanced Photon Source. *AIP Conference Proceedings* **2010**, *1234* (1), 299-302.
- 6) Ladshaw, A.; Wiechert, A.; Welty, A.; Lyon, K.; Law, J.; Jubin, R.; Tsouris, C.; Yiacoumi, S. Adsorbents and adsorption models for capture of Kr and Xe gas mixtures in fixed-bed columns. *Chemical Engineering Journal* **2019**, *375*, 122073.
- 7) Gaston, D.; Newman, C.; Hansen, G.; Lebrun-Grandié, D. MOOSE: A parallel computational framework for coupled systems of nonlinear equations, *Nuc. Eng. Design*, **239**,1768-1778, 2009.
- 8) Patton, K. K.; Bruffey, S. H.; Jubin, R. T.; Walker, J. F. J. In *Effects of Extended In-Process Aging of Silver-Exchanged Mordenite on Iodine Capture Performance*, 33rd Nuclear Air Cleaning Conference, St Louis, MO (United States), St Louis, MO (United States), 2014.
- 9) Wiechert, A.; Ladshaw, A.; Nan, Y.; Choi, S.; Tavlarides, L.; Tsouris, C. Yiacoumi, S. *Mechanisms of Adsorbent Aging and Its Influence on Iodine Capture from Nuclear Fuel Reprocessing Off-gas*. 93rd ACS Colloid and Surface Science Symposium, Atlanta, GA, 2019.
- 10) Carley, A.F.; Davies, P.R.; Roberts, M.W.; Santra, A.K.; Thomas, K.K. Co-adsorption of carbon monoxide and nitric oxide at Ag(111): evidence for a CO-NO surface complex. *Surface Science* **1998**, *406*, L587-L591.
- 11) Henderson, M.A. The interaction of water with solid surfaces: fundamental aspects revisited. *Surface Science Reports* **2002**, *46*, 1-308.

- 12) Marbrow, R.A.; Lambert, R.M. Chemisorption and Surface Reactivity of Nitric Oxide on Clean and Sodium-dosed Ag(110). *Surface Science* 1976, 61, 317-328.
- 13) Wang, Y.-X.; Wang, G.-C. Water Dissociation on Clean and Potassium Preadsorbed Transition Metals: A Systematic Theoretical Study. *J. Phys. Chem. C* **2018**, 122, 15474-15484.
- 14) Andrieux-Ledier, A.; Tremblay, B.; Courty, A. Stability of Self-Ordered Thiol-Covered Silver Nanoparticles: Oxidative Environmental Effects. *Langmuir* **2013**, 29, 13140-13145.
- 15) Rodriguez, L.M.; Gayone, J.E.; Sanchez, E.A.; Grizzi, O.; Blum, B.; Salvarezza, R.C. Room-Temperature Kinetics of Short-Chain Alkanethiol Film Growth on Ag(111) from the Vapor Phase. *J. Phys. Chem. B* **2006**, 110, 7095-7097.
- 16) Xue, G.; Ma, M.; Zhang, J.; Lu, Y.; Carron, K.T. SERS and XPS Studies of the Molecular Orientation of Thiophenols from the Gaseous State onto Silver. *J. Coll. Inter. Sci.* **1992**, 150, 1-6.
- 17) Vericat, C.; Vela, M.E.; Corthey, G.; Pensa, E.; Cortes, E.; Fonticelli, M.H.; Ibanez, F.; Benitez, G.E.; Carro, P.; Salvarezza, R.C. Self-assembled monolayers of thiolates on metals: a review article on sulfur-metal chemistry and surface structures. *RCS Adv.* **2014**, 4, 27730-27754.
- 18) Padmos, J.D.; Boudreau, R.T.M.; Weaver, D.F.; Zhang, P. Impact of Protecting Ligands on Surface Structure and Antibacterial Activity of Silver Nanoparticles. *Langmuir* **2015**, 31, 3745-3752.
- 19) Desireddy, A.; Conn, B.E.; Guo, J.; Yoon, B.; Barnett, R.N.; Monahan, B.M.; Kirschbaum, K.; Griffith, W.P.; Whetten, R.L. Landman, U.; Bigioni, T.P. Ultrastable silver nanoparticles. *Nature* **2013**, 501, 399-402.
- 20) Chen, R.; Nuhfer, N.; Moussa, L.; Morris, H.; Whitmore, P.M. Silver sulfide nanoparticle assembly obtained by reacting an assembled silver nanoparticle template with hydrogen sulfide gas. *Nanotechnology* **2008**, 19, 455604.
- 21) Sadovnikov, S.I.; Vovkotrub, E.G.; Thermal stability of nanoparticle size and phase composition of nanostructured Ag₂S silver sulfide. *J. Alloys Comp.* **2018**, 766, 140-148.
- 22) Outka, D.A.; Madix, R.J. Sulfur Dioxide Adsorption and Reaction with Atomic Oxygen on the Ag(110) Surface. *Surf. Sci.* **1984**, 137, 242-260.
- 23) Omlid, S.M.; Zhang, M.; Isor, A.; McCulla, R.D. Thiol Reactivity toward Atomic Oxygen Generated during the Photodeoxygenation of Dibenzothiophene S-Oxide. *J. Org. Chem.* **2017**, 82, 13333-13341.

- 24) Cambell, C.T. Atomic and Molecular Oxygen Adsorption on Ag (111). *Surf. Sci.* **1985**, *157*, 43-60.
- 25) Bao, X.; Muhler, M.; Schedel-Niedrig, T.; Schlogl, R. Interaction of oxygen with silver at high temperature and atmospheric pressure: A spectroscopic and structural analysis of a strongly bound surface species. *Phys. Rev. B* **1996**, *54*, 2249-2262.
- 26) Xu, Y.; Greeley, J.; Mavrikakis, M. Effect of Subsurface Oxygen on the Reactivity of the Ag (111) Surface. *J. Am. Chem. Soc.* **2005**, *127*, 12823-12827.
- 27) Alemozafar, A.R.; Madix, R.J. Surface reorganization accompanying the formation of sulfite and sulfate by reaction of sulfur dioxide with oxygen on Ag (111). *J. Chem. Phys.* **2005**, *122*, 214718.

6.7 Nomenclature

XAS – X-ray Absorption Spectroscopy

XANES – X-ray Absorption Near Edge Structure

$\mu(E)$ – X-ray linear absorption coefficient

Ag_2SO_2 – Silver Hyposulfite

Ag_2SO_3 – Silver Sulfite

DG – Discontinuous Galerkin

CHAPTER 7: Conclusions and Recommendations

Adsorption encompasses a wide variety of processes, occurring in numerous different media which can be applied to a vast range of potential applications. The research described here was focused on the investigation of adsorbents for applications in the area of nuclear fuel resources. Specifically, this work was divided into two major areas with the first considering adsorbents for uranium (U) recovery from seawater while the second delved into materials intended for use in nuclear fuel reprocessing to capture radioiodine off-gas. Amidoxime adsorbents are currently considered the most promising materials for the recovery of U from seawater and, as such, were explored here. For iodine gas capture, silver (Ag) adsorbents, including reduced silver exchanged mordenite (Ag^0Z) and reduced silver (Ag^0) functionalized silica aerogel, were analyzed with the intent of elucidating how these materials interact with other off-gas constituents to better predict actual performance.

Adsorbents prepared by grafting amidoxime polymer chains to an inert backbone fiber, typically polyethylene, through radiation induced graft polymerization have been examined at length for the recovery of U from seawater. Despite the many strides that have been made, the cost of U recovery is still too high to be commercially viable. Thus, either the capacity of these materials must be improved or the cost associated with manufacturing and deploying the adsorbent must be reduced. The first section of this part (CHAPTER 2) was principally concerned with the effect of graft chain hydrophilicity and adsorbent conditioning on chain conformation. Film conformation is important because it services as a predictor of film diffusivity, accessibility to adsorption sites, and thus

adsorption performance. Adding hydrophilic comonomers was shown to promote film swelling in solution, producing a more dilute polymer film with greater accessibility to adsorption sites. After conditioning an amidoxime-copolymer diblock film, a slight decline in film thickness and an increase in the density of the copolymer film near the interface of the two layers were observed. This effect was a consequence of the conditioner's kosmotropic properties which make water-polymer bonds less favorable. These results call into question the need for conditioning which has been justified in the past as a means to improve the hydrophilicity of hydrophobic amidoxime polymers. If the same effect can be achieved through the use of a hydrophilic comonomer, however, then conditioning could be removed to substantially reduce the cost of recovery.

The next section (CHAPTER 3) considered the effect of competing ions on adsorbent performance. Adsorption experiments were performed with feed seawater and desalination brine reject. Despite having a far higher concentration of U than seawater, brine reject yielded significantly less U primarily as a result of competition from iron (Fe) and vanadium (V). A chemisorption model, previously developed to consider U and V speciation, was expanded to include copper, iron, magnesium, and calcium. This modeling work, coupled with experimental results, was used to explore additional properties of the various elements adsorbed. In the case of U, for example, modeling results suggest that U adsorption in brine is highly susceptible to ligand availability. As established in CHAPTER 2, ligand availability is tied to chain conformation which in turn can be effected by kosmotropic ions. Brine reject contains a significantly higher concentration of kosmotropes meaning that conformation of the adsorbent likely plays a role in the lower U adsorption in addition to competition from Fe and V. For the final

section of the first part (CHAPTER 4), an amidoxime adsorbent synthesized by directly amidoximating a commercially available acrylic fiber rather than grafting an inert backbone fiber with amidoxime polymers was examined. Experimental and modeling analysis of the adsorbent showed that it could outperform the grafted fiber adsorbent with respect to U adsorption at lower temperatures while it is predicted to match adsorption at higher temperatures. This is significant, principally because the adsorbent synthesized from acrylic fiber is significantly cheaper to produce and maintain. Further studies of this material are needed, however, to assess its durability and scalability. Scalability, in particular, appears to be a potential issue with this adsorbent since the large polymer braids also tested in this study adsorbed significantly less U.

The results of the research described in Part I provide a number of different potential avenues by which amidoxime based adsorbents can be optimized to significantly reduce U recovery costs. While improving the U capacity is one potential avenue to reduce the cost of recovery, adjustments to adsorbent synthesis, alkaline treatment, and deployment procedures are likely to yield the most substantial cost savings going forward. The acrylic adsorbent, considered in CHAPTER 4, is particularly interesting in this regard. Considering only its superior adsorption performance and cheaper alkaline treatment, the cost of U recovery using the acrylic adsorbent should be around 40% lower than the grafted adsorbents at 20°C under ideal conditions. These savings could be increased even further by incorporating this adsorbent into existing infrastructure as discussed in CHAPTER 3. Thus, even without considering the cost savings from the simplified synthesis of the acrylic adsorbent, it is entirely possible to reduce the overall U recovery costs under ideal conditions by more than 50% at 20°C if

the expected long term performance is accurate. This cost reduction is not sufficient to make U recovery commercially viable at the current market price of U. Nevertheless, successive improvement of the acrylic adsorbent could, in a relatively short period of time, place the cost of U recovery from seawater within the historic range of U prices.

In the second part of this work, the aging effect in Ag^0Z (CHAPTER 5) and Ag^0 functionalized aerogel (CHAPTER 6) was investigated in an attempt to determine the underlying causes of aging. In both adsorbents, aging is known to occur but the processes that govern aging have not previously been studied. Across all aging environments, Ag^0Z experienced a greater degree of inorganic iodine (I_2) capacity loss than the Ag^0 aerogel. This difference can be attributed to a combination of the metal ion impurities in Ag^0Z catalyzing reactions with gas species that would not otherwise react with Ag^0 and in the aerogel to the presence of thiol groups that bind to and protect the Ag^0 nanoparticles. As a result, the chemical reasons for material aging vary significantly between the two materials. Further investigation of both materials is still needed to determine the processes that govern aging in the environments not already considered, such as 2% nitrogen dioxide in dry air aging for Ag^0 aerogel which was not examined in this work. Additionally, while aerogels appear to be a promising alternative to Ag^0Z , they have yet to be proven under real reprocessing off-gas conditions and their capacity for organic iodides is not well established.

It may also be possible to improve Ag^0Z resistance to aging by, for example, dehydrating the mordenite after reduction. The Ag^0Z s currently used are hydrated, and it is a consequence of this hydration that ions can migrate through the mordenite structure. Dehydrating the mordenite would trap ions, not already on the surface, within the interior

of the mordenite preventing, for example, sodium from migrating to the Ag nanoparticle's surface where it can catalyze dissociative nitric oxide adsorption. This would require capture of water vapor at some point before the off-gas stream reaches the mordenite column which would not be implausible considering separate recovery of water is already desired to capture valuable tritium. In addition, the research described here only examines adsorption of inorganic iodine though numerous species of organic iodides exist in reprocessing off-gas. Additional investigations will need to be performed to determine how aging affects both the mordenite's and the aerogel's organic iodine adsorption capacity. Furthermore, the adsorption of many organic iodides, particularly long-chain organics such as iodododecane, on Ag adsorbents has not yet been studied. Thus, the processes governing the adsorption of these iodides must first be determined before the effect of aging can properly be established.

There are many aspects of Ag adsorbent aging that have not yet been explored and while additional experimental investigation is certainly needed there are many areas where this type of analysis is likely to be extremely difficult, time consuming, or costly. This is particularly true when trying to understand adsorbent aging at a fundamental mechanistic level. In this context, one must be aware of a variety of short lived transient and intermediate species that while difficult to observe experimentally are absolutely essential to the development of precise aging reaction pathways. Molecular modeling is a good alternative to experimentation when attempting to examine material aging at this level. The feasibility, transition states, and even reaction rates for potential reaction mechanisms can all be examined through molecular modeling. One potential application for these techniques could be to determine which of the two silver sulfate forming

reactions discussed in CHAPTER 6 is most favorable. This would be difficult to assess experimentally because of the short lived nature of silver sulfite on the nanoparticle's surface. Another possibility would be to determine the reaction pathway by which I_2 is adsorbed on unreduced silver mordenite to form α -phase silver iodide. That process would be exceptionally difficult to examine experimentally since it only proceeds deep within, and as a direct consequence of, the mordenite crystal structure.

APPENDIX A: Uranium Recovery from Seawater

A.1 Aqueous Speciation Model

The model used in CHAPTER 3 of this work is the Speciation-object Hierarchy for Adsorption Reactions and Kinetics (SHARK) which is a component of the much larger Ecosystem modeling framework. Ecosystem was developed by Dr. Austin Ladshaw as a component of his PhD research and is an open-source collection of modeling tools for simulation of both gas and aqueous phase processes.^{A1} The modeling framework is thus divided into two main components: (i) the Fundamental Off-gas Collection of Kernels (FLOCK) which handles gas systems and (ii) the Seawater Codes from a Highly Object-Oriented Library (SCHOOL) for aqueous systems. There is nevertheless overlap between these two components with SHARK, for example, relying upon the Linear Algebra Residual Kernel (LARK) which is a member of the FLOCK. LARK contains subroutines for iteratively solving linear (Krylov Subspace methods) and non-linear (Picard and Jacobi-Free Newton Krylov methods) systems. As such, LARK is not specifically tied to either media and is used in a number of different kernels within the Ecosystem framework. Recent development of the Ecosystem framework has trended towards kernels for simulation of radioactive decay in the context of nuclear accidents or detonations.^{A2} The full source code for the Ecosystem modeling framework can be found and downloaded at <https://bitbucket.org/gitecosystem/ecosystem> and can be run with only a C/C++ compiler.

Table A1. Concentration ($\mu\text{g/L}$) determined from 10 mL aliquots of feed seawater.

Time (day)	V	Fe	Cu	Zn	U
0	0.522	1.98	5.28	4.80	2.90
8	0.162	0.99	2.01	7.05	1.86
15	0.071	1.17	1.63	7.87	1.42
22	0.050	1.38	1.47	8.22	1.11
30	0.039	0.61	1.39	8.18	1.03
36	0.027	1.57	1.36	8.94	0.89
56	0.027	2.59	1.08	10.7	0.51
64	0.025	2.27	1.02	10.0	0.41
72	0.022	2.21	0.94	10.5	0.35
84	0.020	2.13	0.88	10.8	0.29

Table A2. Concentration ($\mu\text{g/L}$) determined from 10-mL aliquots of brine reject.

Time (day)	V	Fe	Cu	Zn	U
0	1.37	0.03	4.74	7.51	6.66
8	0.620	54.4	4.31	7.46	6.16
15	0.385	54.7	4.26	7.82	6.08
22	0.267	55.8	4.12	8.37	5.82
30	0.148	1.97	2.82	7.6	5.65
36	0.193	49.0	3.85	8.69	5.53
56	0.130	41.3	3.27	8.61	5.3
64	0.171	72.7	3.98	11.3	5.36
72	0.098	31.4	3.13	9.24	5.1
84	0.087	29.6	3.00	9.46	5.12

Table A3. Summary of adsorption reactions with IDO ligand and their equilibrium constants considered in the adsorption model in addition to the reactions used in the works of Ladshaw and coworkers^{A3-A5} adjusted for 23°C and zero ionic strength.^{A6,A7}

Reactions	$\log \beta$				
	UO_2^{2+}	Fe^{3+}	Cu^{2+}	Ca^{2+}	Mg^{2+}
$\text{M}^j + \text{HIDO}^{2-} \leftrightarrow \text{MHIDO}^{j-2}$	19.3		20.2	3.6	
$\text{M}^j + \text{H}^+ + \text{HIDO}^{2-} \leftrightarrow \text{MH}_2\text{IDO}^{j-1}$	23.5	27.3	24.0	15.8	15.7
$\text{M}^j + 2 \text{HIDO}^{2-} \leftrightarrow \text{M}(\text{HIDO})_2^{j-4}$	29.0	38.6	25.7		
$\text{M}^j + \text{H}^+ + 2 \text{HIDO}^{2-} \leftrightarrow \text{M}(\text{H}_2\text{IDO})\text{HIDO}^{j-3}$	38.9	46.8	27.7	18.6	19.8
$\text{M}^j + 2 \text{H}^+ + 2 \text{HIDO}^{2-} \leftrightarrow \text{M}(\text{H}_2\text{IDO})_2^{j-2}$	44.2	52.6			
$\text{M}^j + \text{H}_2\text{O} + 2 \text{HIDO}^{2-} \leftrightarrow \text{MOH}(\text{HIDO})_2^{j-5}$		27.7			
$\text{M}^j + \text{Na}^+ + \text{H}^+ + 2 \text{HIDO}^{2-} \leftrightarrow \text{NaMH}(\text{HIDO})_2^{j-2}$	39.2				

Table A4. Summary of aqueous reactions considered in the adsorption model in addition to those used in the works of Ladshaw and coworkers.^{A3-A5} Equilibrium constants are adjusted for 23°C and zero ionic strength.

Reactions	log β	Reactions	log β
$\text{Fe}^{3+} + \text{H}_2\text{O} \leftrightarrow \text{FeOH}^{2+} + \text{H}^+$		$\text{Cu}^{2+} + \text{H}_2\text{O} \leftrightarrow \text{CuOH}^+ + \text{H}^+$	
$\text{Fe}^{3+} + 2 \text{H}_2\text{O} \leftrightarrow \text{Fe}(\text{OH})_2^+ + 2 \text{H}^+$		$\text{Cu}^{2+} + 2 \text{H}_2\text{O} \leftrightarrow \text{Cu}(\text{OH})_2 + 2 \text{H}^+$	
$\text{Fe}^{3+} + 3 \text{H}_2\text{O} \leftrightarrow \text{Fe}(\text{OH})_3 + 3 \text{H}^+$		$\text{Cu}^{2+} + 3 \text{H}_2\text{O} \leftrightarrow \text{Cu}(\text{OH})_3^- + 3 \text{H}^+$	
$\text{Fe}^{3+} + 4 \text{H}_2\text{O} \leftrightarrow \text{Fe}(\text{OH})_4^- + 4 \text{H}^+$		$\text{Cu}^{2+} + 4 \text{H}_2\text{O} \leftrightarrow \text{Cu}(\text{OH})_4^{2-} + 4 \text{H}^+$	
$\text{Fe}^{3+} + \text{B}(\text{OH})_4^- \leftrightarrow \text{FeB}(\text{OH})_4^{2+}$	8.6 ^a	$\text{Cu}^{2+} + \text{CO}_3^{2-} \leftrightarrow \text{CuCO}_3$	6.8 ^c
$\text{Fe}^{3+} + 2 \text{B}(\text{OH})_4^- \leftrightarrow \text{Fe}(\text{B}(\text{OH})_4)_2^+$	15.5 ^a	$\text{Cu}^{2+} + 2 \text{CO}_3^{2-} \leftrightarrow \text{Cu}(\text{CO}_3)_2^{2-}$	10.0 ^c
$\text{Fe}^{3+} + \text{F}^- \leftrightarrow \text{FeF}^{2+}$	5.18 ^b	$\text{Cu}^{2+} + \text{HCO}_3^- \leftrightarrow \text{CuHCO}_3^+$	2.7 ^c
$\text{Fe}^{3+} + 2 \text{F}^- \leftrightarrow \text{FeF}_2^+$	9.1 ^b	$\text{Cu}^{2+} + \text{SO}_4^{2-} \leftrightarrow \text{CuSO}_4$	2.3 ^c
$\text{Fe}^{3+} + 3 \text{F}^- \leftrightarrow \text{FeF}_3$	11.9 ^b	$\text{Cu}^{2+} + \text{Cl}^- \leftrightarrow \text{CuCl}^+$	0.0 ^c
$\text{Fe}^{3+} + \text{SO}_4^{2-} \leftrightarrow \text{FeSO}_4^+$	2.2 ^b	$\text{Cu}^{2+} + 2 \text{Cl}^- \leftrightarrow \text{CuCl}_2$	-0.7 ^c
$\text{Fe}^{3+} + 2 \text{SO}_4^{2-} \leftrightarrow \text{Fe}(\text{SO}_4)_2^-$	3.2 ^b	$\text{Cu}^{2+} + 3 \text{Cl}^- \leftrightarrow \text{CuCl}_3^-$	-2.2 ^c
$\text{Fe}^{3+} + \text{Cl}^- \leftrightarrow \text{FeCl}^{2+}$	0.5 ^b	$\text{Cu}^{2+} + 4 \text{Cl}^- \leftrightarrow \text{CuCl}_4^{2-}$	-4.4 ^c
$\text{Fe}^{3+} + 2 \text{Cl}^- \leftrightarrow \text{FeCl}_2^+$	-0.4 ^b	$\text{F}^- + \text{H}^+ \leftrightarrow \text{HF}$	
$2 \text{FeOH}^{2+} \leftrightarrow \text{Fe}_2(\text{OH})_2^{4+}$		$2 \text{F}^- + \text{H}^+ \leftrightarrow \text{HF}_2^-$	
$\text{B}(\text{OH})_3 + \text{H}_2\text{O} \leftrightarrow \text{B}(\text{OH})_4^- + \text{H}^+$			

a. From Byrne and Kester. Ref A8.

b. From Millero et al. Ref A9.

c. From Zirino and Yamamoto. Ref A10.

Table A5. Concentration ratios for each of the trace elements examined experimentally to the uranium (U) concentration in both feed seawater and desalination brine reject.

	X:U			
	V	Fe	Cu	Zn
Seawater	5.56	1.46	0.55	0.60
Brine reject	4.86	8.17	0.71	0.89

A.2 References

- A1) Ladshaw, A.P. (2017). *Complex Adsorption Modeling for Nuclear Energy Applications* (Doctoral Dissertation). Georgia Institute of Technology, Atlanta, GA.
- A2) Ladshaw, A.P.; Wiechert, A.I.; Kim, Y-H.; Tsouris, C.; Yiacoumi, S. Algorithms and algebraic solutions of decay chain differential equations for stable and unstable nuclide fractionation. *Comp. Phys. Comm.* **2020**, *246*, 106907.
- A3) Ladshaw, A.P.; Das, S.; Liao, W.-P.; Yiacoumi, S.; Janke, C.; Mayes, R.; Dai, S.; Tsouris, C. Experiments and Modeling of Uranium Uptake by Amidoxime-Based Adsorbent in the Presence of Other Ions in Simulated Seawater. *Ind. Eng. Chem. Res.* **2016**, *55*, 4241-4248.

- A4) Ladshaw, A.P.; Wiechert, A.I.; Das, S.; Yiacoumi, S.; Tsouris, C. Amidoxime Polymers for Uranium Adsorption: Influence of Comonomers and Temperature. *Materials*. **2017**, *10*, 1268.
- A5) Ladshaw, A.P.; Ivanov, A.S.; Das, S.; Bryantsev, V.; Tsouris, C.; Yiacoumi, S. First-Principles Integrated Adsorption Modeling for Selective Capture of Uranium from Seawater by Polyamidoxime Sorbent Materials. *Appl. Mater. Interfaces*. **2018**, *10*, 12580-12593.
- A6) Sun, X.; Xu, C.; Tian, G.; Rao, L. Complexation of glutarimidedioxime with Fe(III), Cu(II), Pb(II), and Ni(II), the competing ions for the sequestration of U(VI) from seawater. *Dalton Trans*. **2013**, *42*, 14621-14627.
- A7) Leggett, C.J.; Rao, L. Complexation of calcium and magnesium with glutarimidedioxime: Implications for the extraction of uranium from seawater. *Polyhedron*. **2015**, *95*, 54-59.
- A8) Byrne, R.H.; Kester, D.R. Solubility of Hydrous Ferric Oxide and Iron Speciation in Seawater. *Marine Chem*. **1976**, *4*, 255-274.
- A9) Millero, F.J.; Yao, W.; Aicher, J. The speciation of Fe(II) and Fe(III) in natural waters. *Marine Chem*. **1995**, *50*, 21-39.
- A10) Zirino, A.; Yamamoto, S. A pH-Dependent Model for the Chemical Speciation of Copper, Zinc, Cadmium, and Lead in Seawater. *Limnol. Oceanogr*. **1972**, *17*, 661-671.

APPENDIX B: Silver Adsorbent Aging

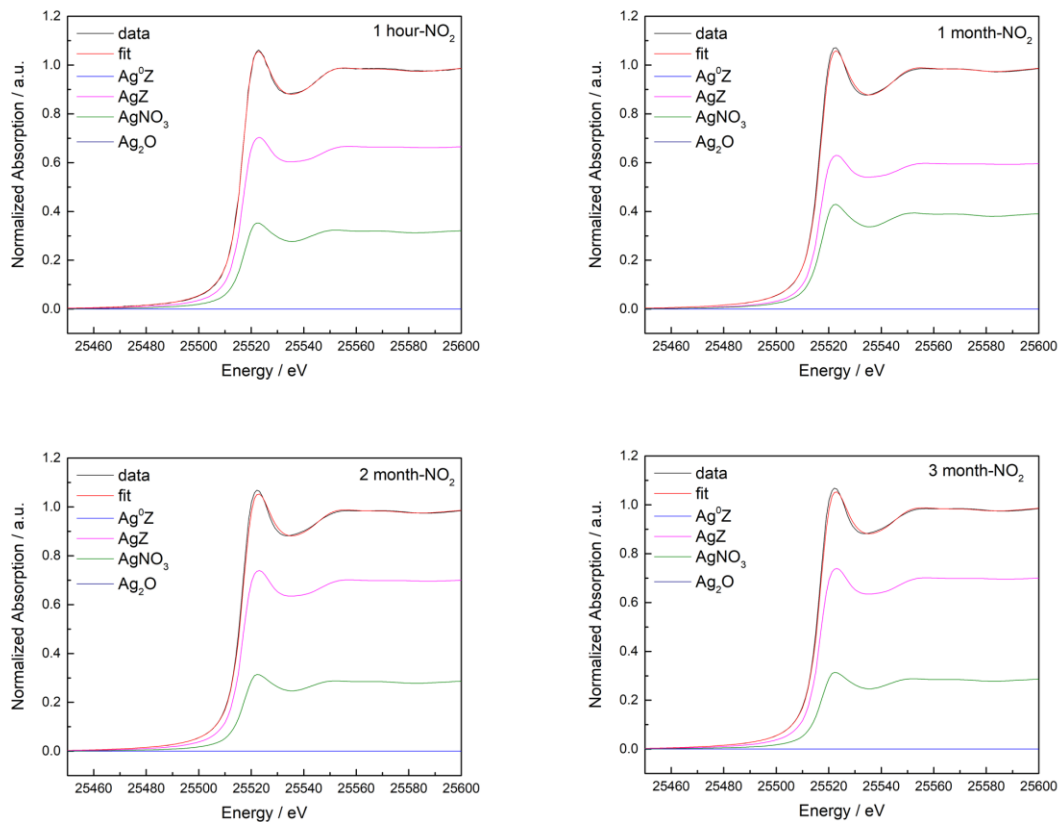


Figure B1. Linear combination fitting (LCF) for Ag^0Z aged in 2% NO_2 in dry air using reference compounds Ag^0Z , Ag_2O , AgNO_3 , and AgZ . Experimental data are in black and the LCF is in red. Reference standards used to achieve the LCFs are plotted beneath and scaled according to their contribution to the fit.

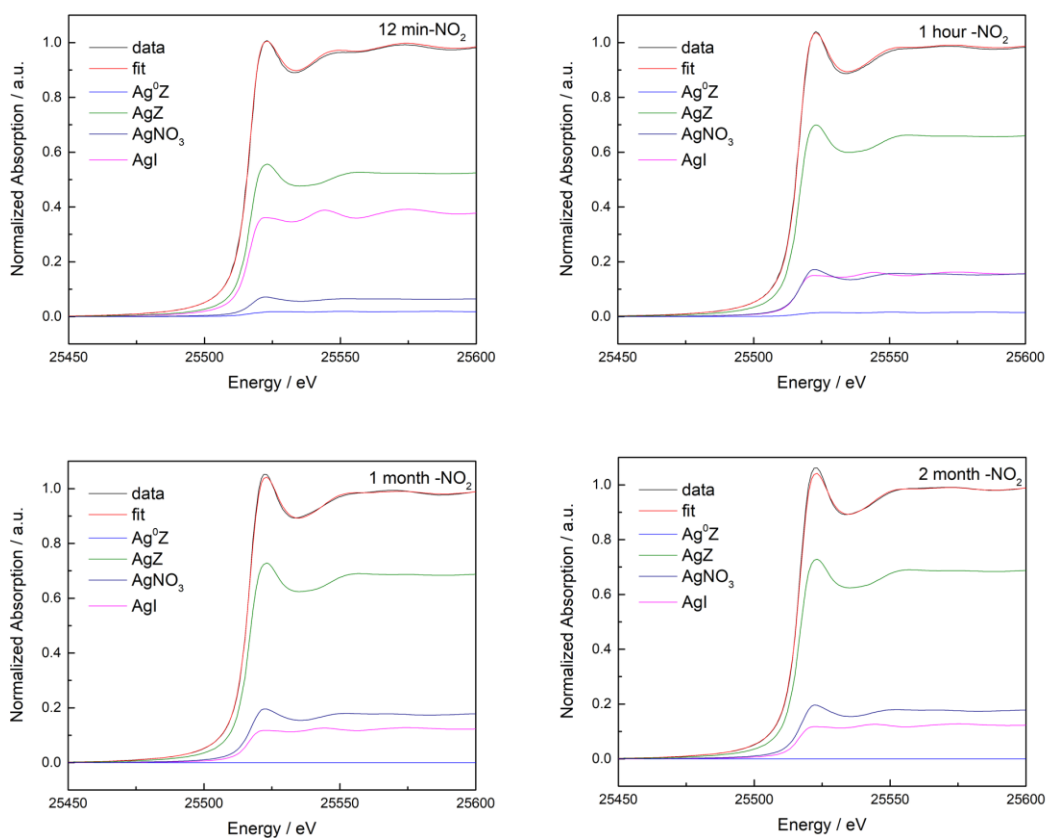


Figure B2. Linear combination fitting (LCF) for Ag⁰Z aged in 2% NO₂ in dry air and then exposed to iodine (I₂) at a concentration of 50 ppmv in dry air using reference compounds Ag⁰Z, Ag₂O, AgNO₃, AgZ, and AgI. Experimental data are in black and the LCF is in red. Reference standards used to achieve the LCFs are plotted beneath and scaled according to their contribution to the fit.

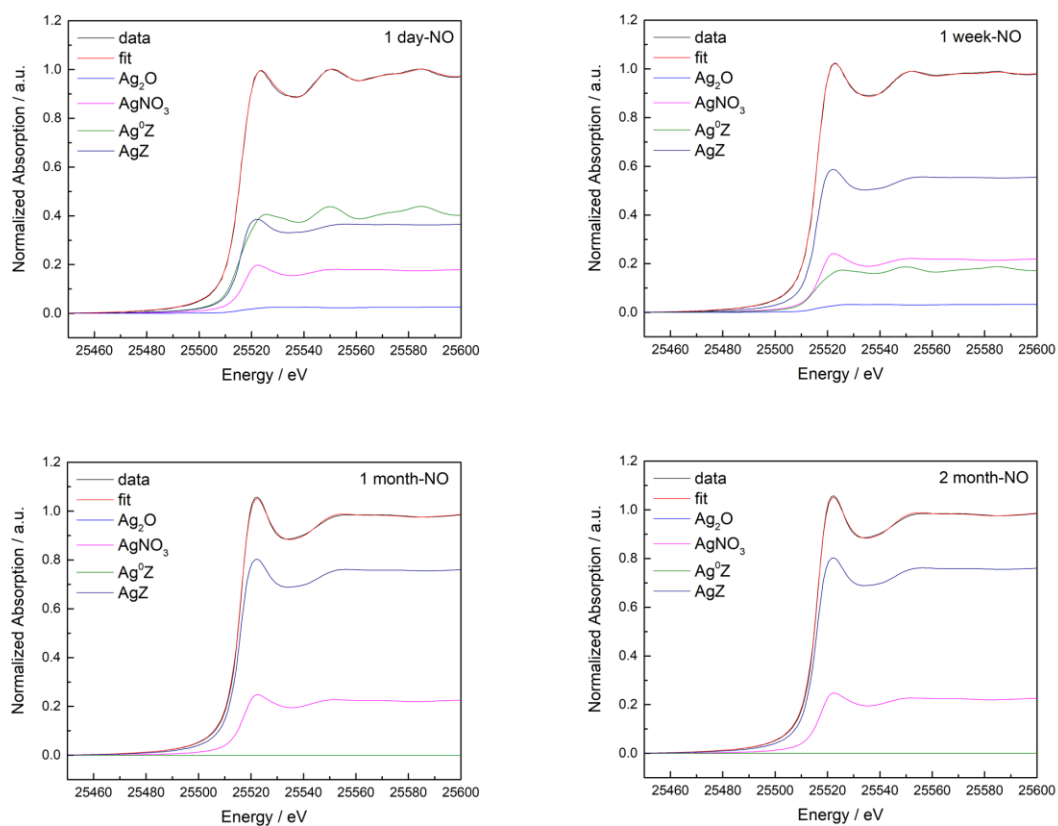


Figure B3. Linear combination fitting (LCF) for Ag^0Z aged in 1% NO in N_2 using reference compounds Ag^0Z , Ag_2O , AgNO_3 , and AgZ . Experimental data are in black and the LCF is in red. Reference standards used to achieve the LCFs are plotted beneath and scaled according to their contribution to the fit.

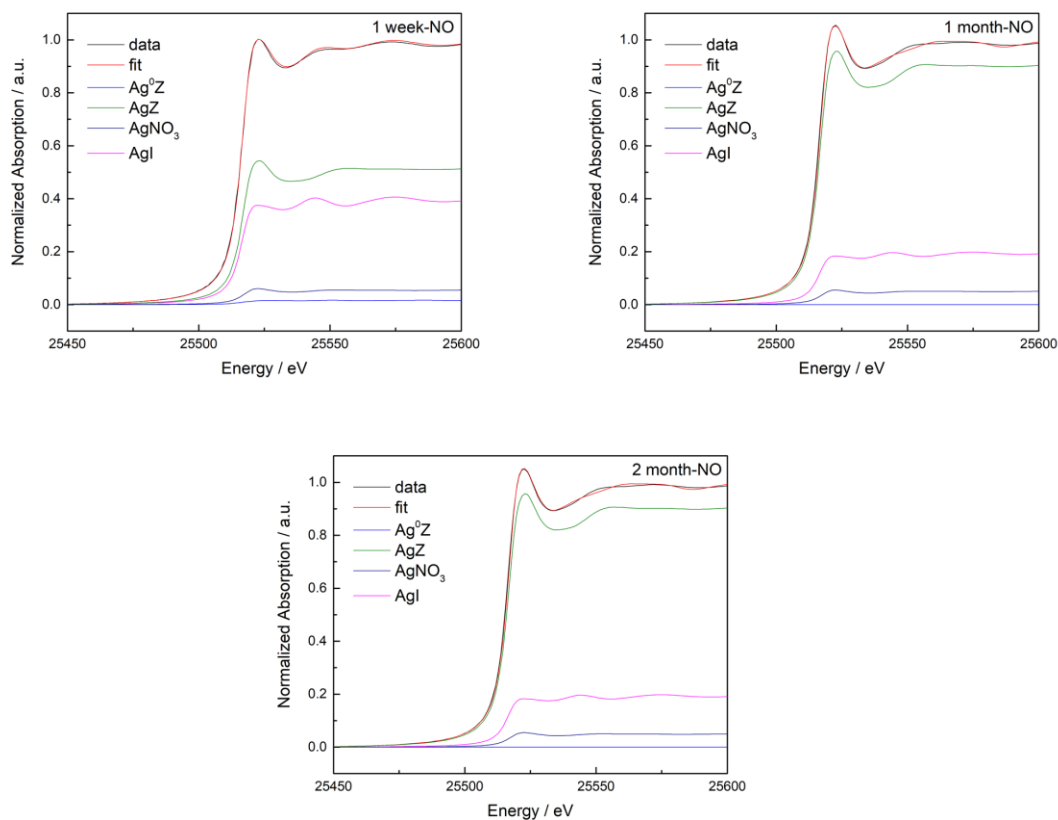


Figure B4. Linear combination fitting (LCF) for Ag⁰Z aged in 1% NO in N₂ and then exposed to iodine (I₂) at a concentration of 50 ppmv in dry air using reference compounds Ag⁰Z, Ag₂O, AgNO₃, AgZ, and AgI. Experimental data are in black and the LCF is in red. Reference standards used to achieve the LCFs are plotted beneath and scaled according to their contribution to the fit.

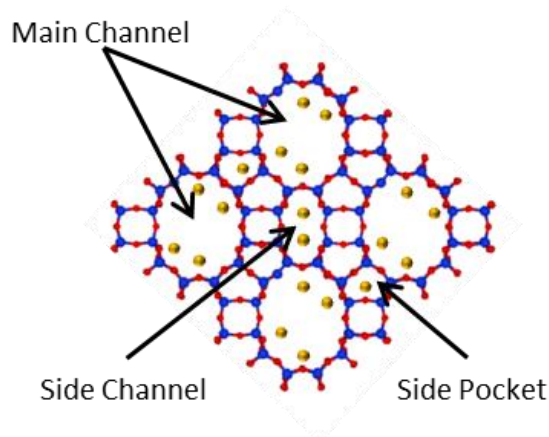


Figure B5. Structure of mordenite crystal where 12-member $7.0 \times 6.5 \text{ \AA}$ main channels, parallel 8-member $5.7 \times 2.6 \text{ \AA}$ side channels, and 5-member side pockets with approximate binding sites shown.

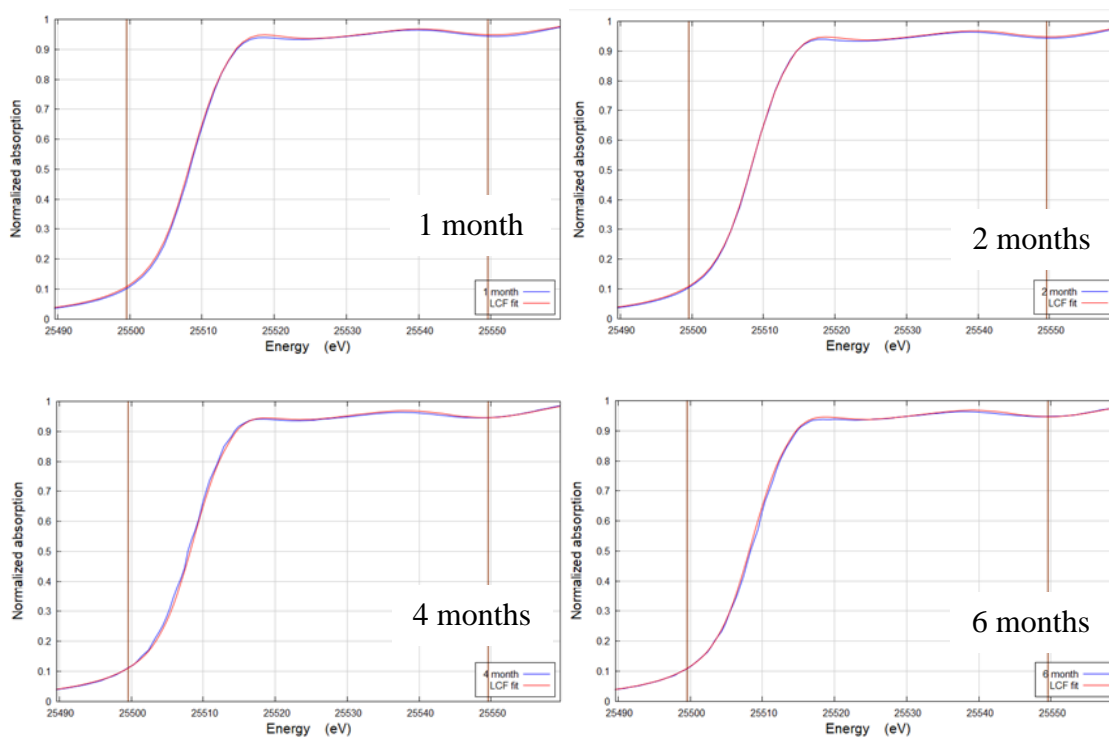


Figure B6. Linear combination fitting (LCF) for Ag^0 aerogel aged in dry air using reference compounds for unaged Ag^0 aerogel, Ag_2S , and Ag_2SO_4 . Experimental data are in black and the LCF is in red.